

Figure I. Experimental setup.

through the experiment using an insulation tube covering the top part of the cathode wire. Gas mixture was fed downward or upward through the reactor at a volume rate of 100 cm³/min. The concentrations of the acetaldehyde and oxygen in the gas mixture were varied, by mixing commercial standard gases. Deionized water, both with and without the dissolved inorganic additives, NaOH or HCl, was circulated as a falling film (approximately 0.4 mm thickness without corona discharge) on the inner surface of the anode, at a volume rate of 1400 cm³/min. The temperature of the water was controlled at 10°C by employing a heat exchanger unit.

The gas composition at the inlet and outlet of the reactor were analyzed by a gas chromatograph (Shimadzu, GC-9A) equipped with an FID detector. To determine the gaseous ozone concentration, the outlet gas was sampled (4 cm³) and bubbled into a 1 mol/L KI solution (5 cm³). Then a UV/VIS spectrophotometer (Shimadzu, UV-1600PC) was used to measure the photoabsorptivity at 288 or 353 nm to estimate the ozone concentration. For aqueous analysis, the FID gas chromatograph and a high performance liquid chromatograph (IIPLC) with a UV-VIS detector (Shimadzu, SPD-10AVP) were employed for analysis of the circulating water. The total organic carbon (TOC) content and pH of the circulating water were measured by a TOC analyzer (Shimadzu, TOC-5000) and a pH meter (Horiba, pH meter F-22), respectively.

Since corona wind is generated during the corona discharge, it can affect the reactions inside the reactor. The corona wind velocity inside the reactor was evaluated as an indication of the degree of gaseous turbulence in the reactor, by measuring the pressure difference between the dynamic pressure in the corona wind and the static pressure outside the reactor, by using a Pitot tube. The measurement was conducted under the condition where gas flowed into the reactor but without water feeding onto the wall of the reactor. This is because the Pitot tube inserted into the corona zone through the anode disturbs the water film.

3 Results and Discussion

3.1 Removal Concept

The concept of removal of acetaldehyde in the wettedwall corona discharge reactor is illustrated in Fig. 2. When the gas stream flows through the upper part of the reactor, a majority of the gaseous acetaldehyde is absorbed into water before it is transferred to the corona zone. After this, the remaining acetaldehyde in the gas stream enters the corona zone where it is removed by gas corona discharge reaction. In the corona discharge zone, free electrons are emitted from the wire cathode and accelerated towards the cylindrical anode by the electric field. Ionization of gas molecules by collision with electrons produces some extra electrons and positive ions [14]. Secondary electrons, which can be produced by photoemission from the discharge electrode, bombardment of the positive ions at the discharge surface, or photoionization in the gas, could all contribute to sustaining the stable corona discharge [14]. These energetic electrons could also dissociate oxygen molecules to produce O radicals in the corona plasma region adjacent to the wire cathode [15].

The dissociation and ionization are expected to take place in the corona plasma zone in which the electron energy is higher than 1.85 eV [14]. It should also be noted that the ionization energy and bonding energy of oxygen are 12.06 and 5.12 eV, and those of nitrogen are 15.6 and 9.76 eV, respectively [14, 16]. Consequently, ozone can be produced by reaction of oxygen with O radical. Since the gas mixture contains the water vapor evaporating from the water film in the reactor, dissociation of H₂O by electron impact could produce radical OH [15]. In the low energy electron region close to the narrow plasma zone, dissociative electron attachment to oxygen and water vapor would produce O, O⁻, OH, and H⁻ [17, 18]. The removal of gaseous acetaldehyde should be enhanced by electron attachment [1] and cluster

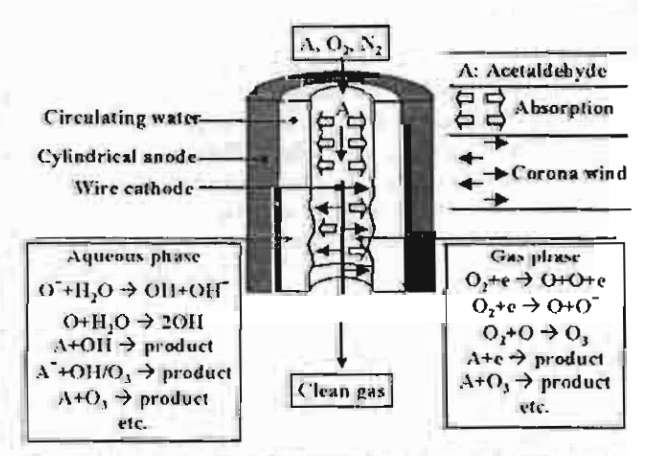


Figure 2. Concept of removal of acetaldehyde using a wetted-wall corona discharge reactor.



formation [2], as well as reaction with ozone and radicals [19,20].

The ions that drift along the electric field to the water film covering the anode create a corona wind, the velocity of which is in the order of several meters per second [21]. Uncharged radicals can also be conveyed to the water surface by the gas turbulence induced by this corona wind. When the O ion and O radical reach the water film, an aqueous OH radical would be produced by their reactions with $\rm H_2O$ [22–24]. Subsequently, the aqueous OH radical is expected to decompose the acetaldehyde absorbed in the aqueous phase. In addition, this OH radical could also decompose the soluble byproducts, which are produced by the gas corona reaction.

3.2 Voltage-Current Characteristics of a Wetted-Wall Corona Discharge Reactor

Fig. 3 shows the voltage-current (V-I) characteristics of the wetted-wall corona discharge reactor at various oxygen concentrations. In the absence of O₂, the corona voltage increases very slightly from 6.5-7.5 kV, while the corona current is increased widely from 0.25-2 mA. In contrast, in the

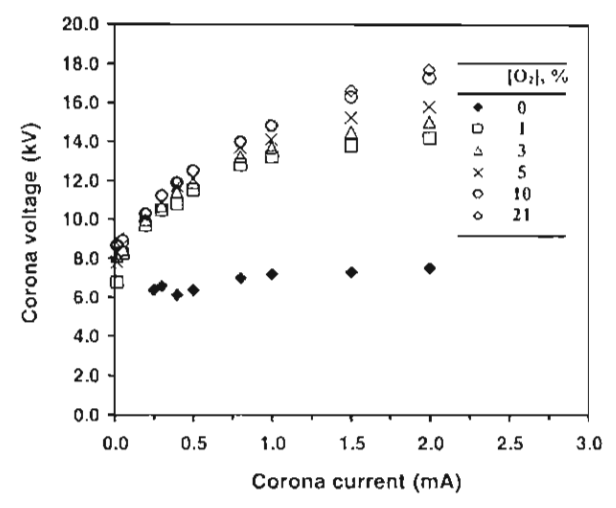


Figure 3. V-I characteristic of wetted-wall corona discharge reactor at various oxygen concentrations.

presence of 1% oxygen, the corona voltage sharply increases from around 8-15 kV when the current is increased from 0.1-2 mA. The increase in oxygen concentration from 1 to 21% causes higher corona voltage requirement. The high electron affinity of O_2 , which easily induces the formation of oxygen ions, could be one of the reasons for this voltage elevation. It should be remembered that the electron affinity of O_2 is significantly higher than that of N_2 – the values are 1.78 and -2.58 eV, respectively. These values were calculated by the density functional calculation at the B3LYP/6-31G level. Because the ion mobility is much lower

than electron mobility [14], the voltage required to maintain the corona discharge in the presence of oxygen is significantly higher than that in its absence. The difference in the voltages required, in the presence and absence of the falling water film on the anode, was found to be insignificant and was generally smaller than 2%.

3.3 Influence of Oxygen on the Removal of Gaseous Acetaldehyde

Fig. 4 shows the outlet concentration of gaseous acetaldehyde, $C_{o.g.}$ during the discharge operation at various oxygen concentrations ranging from 0–21%, at a fixed corona current, with downward gas flow¹⁾. The inlet concentration of gaseous acetaldehyde here is 200 mole-ppm. Without the corona discharge, $C_{o.g.}$ is initially zero, proving that acetaldehyde is readily absorbed into fresh water. However, $C_{o.g.}$ rap-

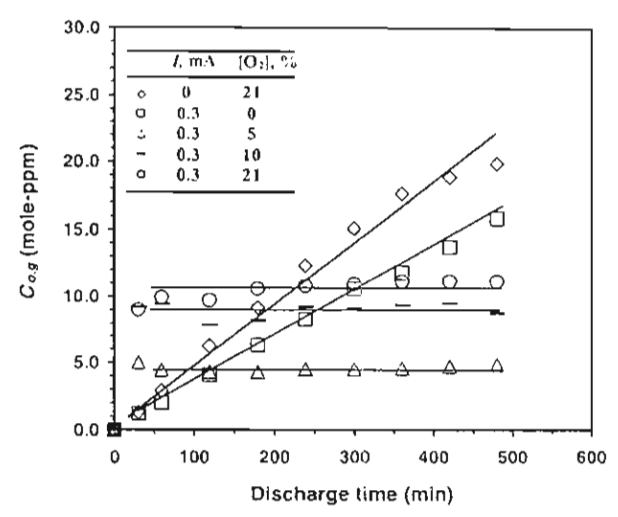


Figure 4. Concentration of acetaldehyde in the treated gas during corona discharge operation at various oxygen concentrations: $C_{l,g} = 200$ mole-ppm, $Q_{\kappa} = 100$ cm³ min⁻¹, $Q_I = 1400$ cm³ min⁻¹, W = 1000 cm³. Gas flow direction = downward.

idly increases with time because the water is continuously contaminated with acetaldehyde. When the corona discharge is generated in the gas stream with 5% oxygen, this increase in $C_{o,g}$ is drastically suppressed. The $C_{o,g}$ becomes a steady state value around 5 mole-ppm at a very early stage. This feature can also be noticed at 10 and 21% oxygen concentration. $C_{o,g}$ increases as the oxygen concentration becomes greater. When oxygen does not coexist in the gas stream, $C_{o,g}$ still increases with elapsed time.

It is considered that the rate of acetaldehyde absorption is not stable because the aqueous acetaldehyde can be accumulated in the water and inhibits the gas absorption. This result indicates that oxygen plays a significant role on the re-

List of symbols at the end of the paper

moval of acetaldehyde in the wetted-wall corona discharge reactor. The ozone concentrations measured at oxygen concentrations of 5, 10, and 21 % were 200, 757, and 1622 ppm, respectively. This clearly shows that an increase in ozone concentration does not contribute to the removal of acetaldehyde. One possible reason why increases in oxygen concentration could inhibit the removal of acetaldehyde will be explained later in this section.

In Fig. 5, the removal extent, ψ , of acetaldehyde defined by Eq. (1) is plotted against corona discharge current, I:

$$\psi = (C_{i,g} - C_{i,g})/C_{i,g}$$
 (1)

where $C_{i,g}$ is the inlet concentration of gaseous acetaldehyde, and $C_{o,g}$ is the time-averaged outlet concentration of acetaldehyde at steady state. The results clearly show that increases in oxygen concentration, inhibit the extent of removal at corona currents of 0.3 and 0.5 mA. Focusing upon

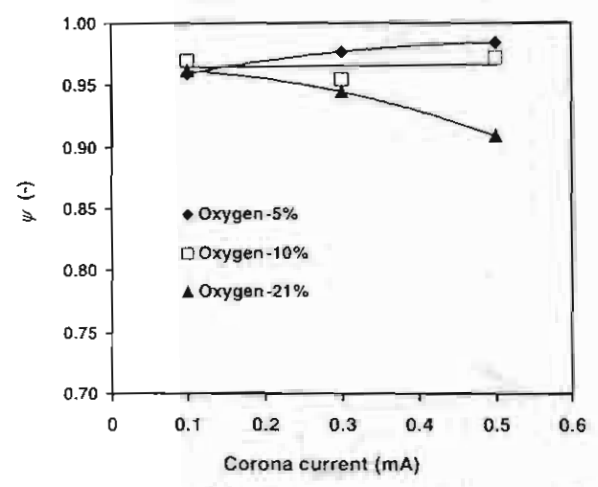


Figure 5. Extent of removal of gaseous acetaldehyde against corona discharge current at various oxygen concentrations; $C_{Lg} = 200 \text{ mole-ppm}$, $Q_g = 100 \text{ cm}^3 \text{ min}^{-1}$. (ias flow direction = downward.

the 5% oxygen concentration, the extent of removal increases, when the current increases from 0.1-0.5 mA. It is reasonable to assume that the higher current provides a higher electron flux, resulting in more effective acetaldehyde removal. However, when the oxygen concentration is 10 or 21%, the increase in the current does not result in a higher removal extent.

The inhibition of acetaldehyde removal by the increase in oxygen concentration could be attributed to corona-induced turbulence in the gas stream inside the reactor. To evaluate the degree of turbulence in the gas stream, the velocity of the corona wind was measured. The corona wind velocity against the oxygen concentration is depicted in Fig. 6. When the current is either 0.3 or 0.5 mA, the increase in oxygen concentration leads to a significant increase in the corona wind velocity. Nonetheless, the corona wind velocity does not significantly increase when current is 0.1 mA. The coro-

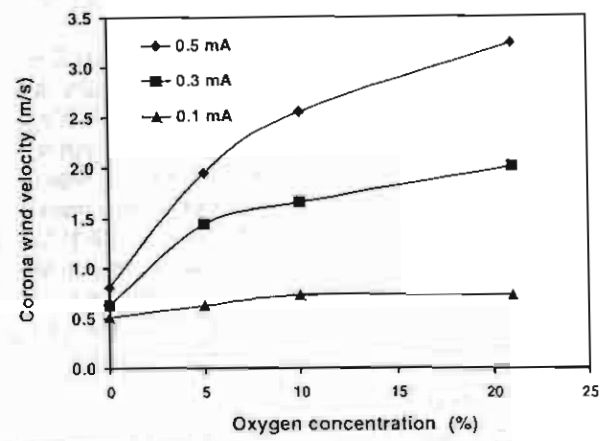


Figure 6. Effect of oxygen on corona wind velocity, $Q_g = 100 \text{ cm}^3 \text{ min}^{-1}$.

na-induced turbulence inside the corona reactor should affect the gas residence time distribution (RTD) in the reaction zone. It is considered that when the turbulence induced by the corona wind becomes stronger, the RTD in the reactor should behave more like that in a continuous stirred tank reactor (CSTR), which results in a much broader RTD compared with a plug flow reactor (PFR). It is common knowledge that, with the exception of the zero-order reaction, the CSTR possesses a lower conversion than the PFR, based upon the same space-time [25]. It should be noted that the negative effect of admixing oxygen, on the extent of removal, could not be observed even when the current was as low as 0.1 mA. This correlates with the observation that the corona-induced turbulence is not affected by O₂ concentration, in the low current range.

3.4 Influence of Oxygen on the Removal of Absorbed Acetaldehyde in Water

Fig. 7 shows the concentrations of aqueous acetaldehyde, C_m, at various oxygen concentrations during the discharge operation. In the absence of corona discharge, C, obviously increases with time, suggesting that acetaldehyde is accumulated in the water by absorption. When corona discharge is generated, the increase in C, is attenuated by the decomposition of aqueous acetaldehyde. When the oxygen concentration is increased from 5 to 10 %, Cw becomes constant at a lower value. It is reasonable to assume that with more oxygen coexisting in the corona zone, more O radical could be produced, not only due to the high O2 concentration, but also the elevated voltage. Consequently, the production of aqueous radical OH is enhanced, resulting in the higher decomposition rate of aqueous acetaldehyde. However, when oxygen is further increased from 10 to 21 %, C, does not decrease further. This is because the elevated corona-induced turbulence disturbs the surface of the falling water film, resulting in less uniform spatial distribution of the gas corona. Previous work revealed that the reduced spatial uniformity

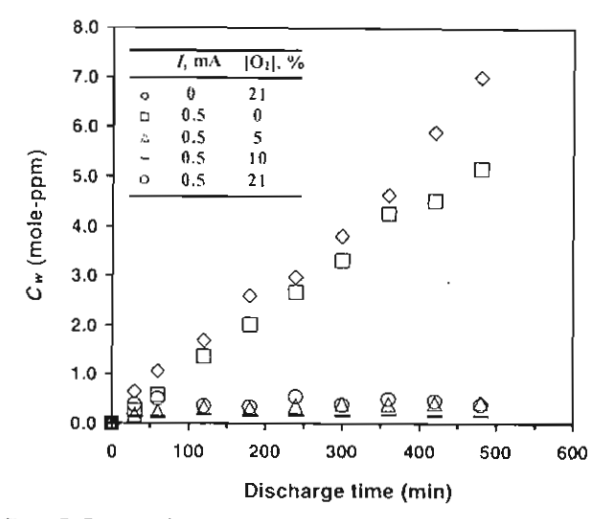


Figure 7. Concentration of acetaldehyde in circulating water during corona discharge operation at various oxygen concentrations; $C_{L_X} = 200 \text{ mole-ppm}$, $Q_x = 100 \text{ cm}^3 \text{ min}^{-1}$, $Q_t = 1400 \text{ cm}^3 \text{ min}^{-1}$, $W = 1000 \text{ cm}^3$. Gas flow direction = downward.

of the gas corona attenuates the decomposition efficiency of an aqueous organic compound in water [12]. The aqueous acetaldehyde is not so effectively decomposed in the absence of oxygen.

Since aqueous acetaldehyde is converted to other organic compounds as intermediate by-products, the total organic carbon TOC was monitored against the decomposition time. Fig. 8 shows the concentrations of TOC in the aqueous phase during the discharge operation at various oxygen concentrations. The figure reveals that, when the oxygen concentration is increased in the range of 5–10 %, the TOC decomposition rate increases. However, when the oxygen concentration is further increased from 10 to 21 %, the TOC decomposition rate does not significantly increase. This is

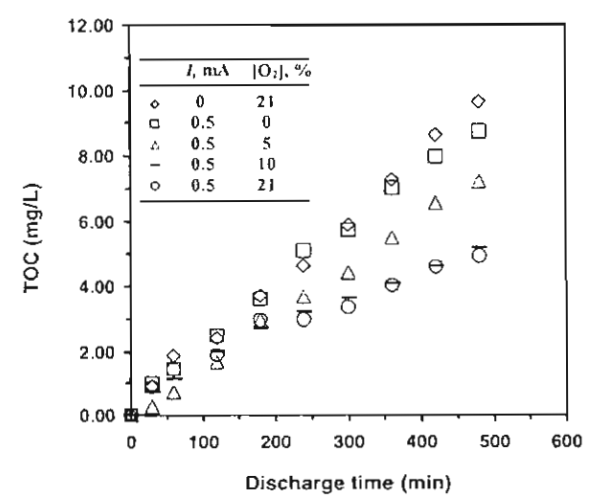


Figure 8. TOC concentration in water against discharge time at various oxygen concentrations: I = 0.5 mA, $C_{lx} = 200 \text{ mole-ppm}$, $Q_g = 100 \text{ cm}^3 \text{ min}^{-1}$, $Q_I = 1400 \text{ cm}^3 \text{ min}^{-1}$, Gas flow direction = downward.

because the smoothness of the water film surface was disturbed, resulting in less spatial uniformity of the corona.

Although the aqueous acetaldehyde concentration becomes stable as shown in Fig. 7, the TOC concentration still increases with time. This result shows that there are some byproducts accumulated in the water that are more stable than acetaldehyde. The byproducts existing in the circulating water were identified by both GC and HPLC. As a result acetic acid which is commonly found in the oxidation treatment of aqueous acetaldehyde [26,27] is detected as the dominant byproduct. Other byproducts exist in negligible quantities compared with acetic acid.

To determine the effect of accumulating acetic acid in water on the removal of acetaldehyde by the present reactor, acetic acid is dissolved into the circulating water at 50 ppm (equivalent to 20 ppm TOC). Fig. 9 shows the concentration of gaseous acetaldehyde at the outlet of the reactor and also that of aqueous acetaldehyde in the circulating water, against discharge time, when pure deionized water or acetic acid solution is used as the circulating water. The result shows that the concentration of gaseous acetaldehyde is consistently at the same level for both cases. Similarly, the difference in aqueous acetaldehyde concentration between the systems, with and without acetic acid contamination, is negligible. This indicates that the removal of gaseous acetaldehyde can be sustained during the corona discharge operation, even if acetic acid is accumulated at high concentrations in the circulating water.

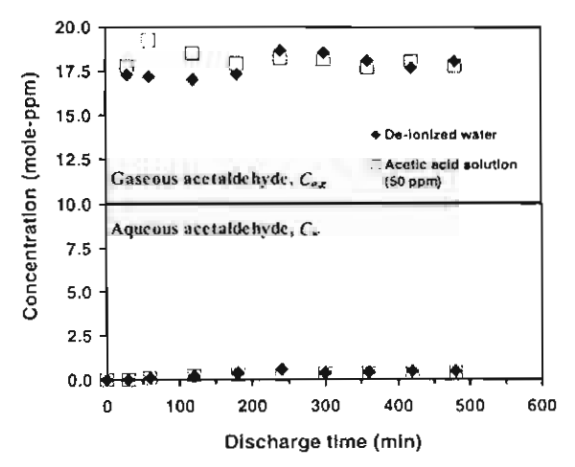


Figure 9. Effect of accumulating acetic acid on gaseous and aqueous acetaldehyde removals: I=0.5 mA, $C_{l,g}=200 \text{ mole-ppm}$, Oxygen = 21%, $Q_g=100 \text{ cm}^3 \text{ min}^{-1}$, $Q_I=1400 \text{ cm}^3 \text{ min}^{-1}$, Gas flow direction = downward.

3.5 Effect of Inorganic Additives on Removal of Gaseous Acetaldehyde

The effects of the inorganic additives, NaOH and HCl dissolved into the circulating water on the removal of gaseous acetaldehyde by the present reactor, were investigated. In Fig. 10, the concentration of aqueous acetaldehyde against

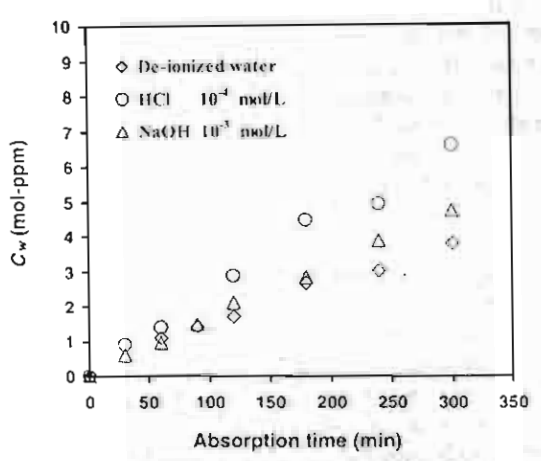


Figure 10. Influence of dissolved inorganic additives on absorbability of acetaldehyde; $C_{tot} = 200$ mole-ppm, $Q_g = 100$ cm³ min⁻¹, $Q_t = 1400$ cm³ min⁻¹. Gas flow direction = upward.

absorption time in the absence of corona discharge, is shown. It is obvious that dissolved NaOH and HCl enhance the absorptivity of acetaldehyde into water. In contrast, it was found in previous work that HNO₃ does not significantly affect the absorptivity of acetaldehyde [13]. In fact, HNO₃ was produced in water during the corona operation, leading to a decrease in the pH of water [22, 23]. When the current is 0.1 mA, the pH of water decreased from around 6-6.5 to 5, corresponding to 10⁻⁵ mol/L HNO₃.

Fig. 11 shows the outlet concentration of gaseous acetal-dehyde during the discharge operation with various dissolved additives. The effect of dissolved inorganic compounds in water is investigated at a corona current 0.1 mA, with upward gas flow. It is found that NaOH enhances the removal of acetaldehyde from the gas stream, whereas HCl retards the removal of gaseous acetaldehyde. When the NaOH concentration is further increased from 10⁻¹ to 10⁻¹ mol/L, the extent of removal of the gaseous acetaldehyde is increased from 97.1–98.5 %.

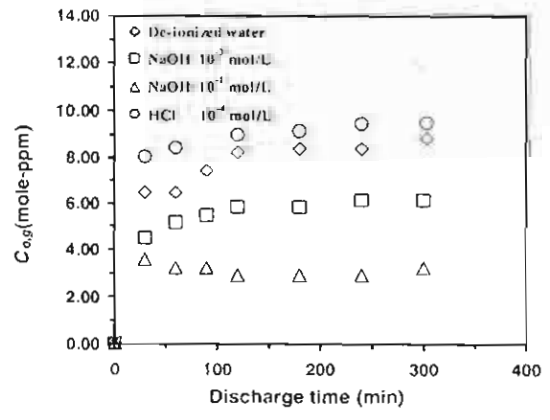


Figure 11. Effect of additives on the concentration of acctaldehyde in treated gas during discharge time; $I \approx 0.1$ mA, $C_{kg} = 200$ mole-ppm, $Q_g = 100$ cm 3 min $^{-1}$, $Q_I = 1400$ cm 3 min $^{-1}$. Gas flow direction – upward.

In considering the effect of HCl, removal of gaseous acetaldehyde is attenuated even if HCl elevates its absorptivity. It is considered that absorbed acetaldehyde may be accumulated in the circulating water, and the increased concentration of aqueous acetaldehyde may consequently inhibit the absorption of gaseous acetaldehyde into water. The concentrations of aqueous acetaldehyde, C_{w_c} in circulating water with dissolved NaOH, HCl, and without additives, during the discharge operation are shown in Fig. 12. As expected, when 10^{-4} mol/L HCl is dissolved in the water, C_w rapidly increases with time and becomes higher than when deionized

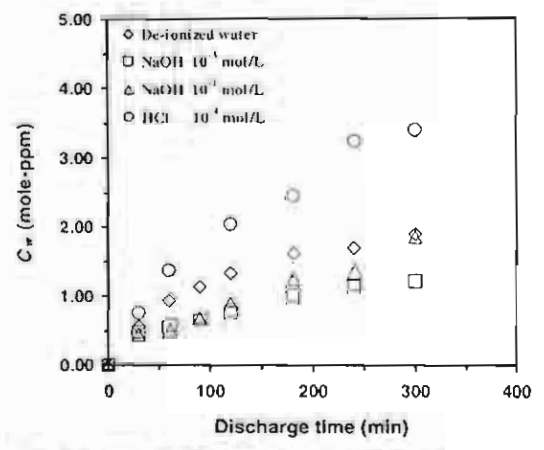


Figure 12. Influence of additives on the accumulation of acetaldehyde in circulating water; I=0.1 mA, $C_{I,K}=200$ mole-ppm, $Q_{K}=100$ cm 3 min $^{-1}$, $Q_{I}=1400$ cm 3 min $^{-1}$, Gas flow direction = upward.

water free of additives is used. This confirms that an increase in C_w could reduce the absorption rate of gaseous acetaldehyde, leading to the inhibition of the removal of gaseous acetaldehyde. The reason why HCl lessens the decomposition of aqueous acetaldehyde might be explained as follows – when HCl is dissolved into the water, dissociated CT could be reacted with OH radical as shown in Eq. 2, with a rate constant of $4.3 \cdot 10^9$ L mol⁻¹ s⁻¹ [28]:

$$OH + Cl^{-} \rightarrow ClOH^{-}$$
 (2)

In addition, the OH radical could react with some derivatives of Cl⁻ such as ClO⁻ and ClO₂⁻ which might be produced in the aqueous phase at high reaction rate [28]. Therefore, these reactions may take place and inhibit the decomposition of aqueous acetaldehyde by OH. This is consistent with previous work in which it was found that adding HCl can inhibit the decomposition of aqueous phenol [29].

Focusing on the effect of NaOH, despite the accelerated adsorption of acctaldehyde, the concentration of aqueous acetaldehyde is reduced. This result suggests that the decomposition rate of the aqueous acetaldehyde can be enhanced by the addition of NaOH. This result may possibly be explained as follows – when NaOH is added to the water, dissociated OH⁻ could be produced which then acts as an initi-



ator to accelerate the decay of ozone, to form the oxidant such as hydroxyl radical, OH [27–30]. Besides the acceleration in OH production by NaOH, the reactivity of the OH radical with organic compounds, may be enhanced by the dissolved NaOH [29]. Eventually, the decomposition of acetaldehyde in water is enhanced. This result is consistent with previous work in which it was found that the addition of NaOH can enhance the decomposition of aqueous phenol [29].

4 Conclusions

The influence of oxygen and dissolved inorganic additives on the removal of gaseous acetaldehyde using a wetted-wall corona discharge reactor was experimentally studied. It was found that acetaldehyde cannot be removed when oxygen does not coexist in the gas stream. The sustainability of removal of acetaldehyde is obtained in the presence of oxygen. There is an optimum O_2 concentration. When the oxygen concentration was 5 %, up to 98.5 % of the gaseous acetaldehyde was removed. The increase in corona current also led to an increase in the extent of its removal at the proper O_2 concentration. An excessive oxygen concentration resulted in a lower extent of removal, when the current was excessively high. This could be attributed to the fact that coronainduced gaseous turbulence broadens the gas residence time distribution in the reaction region.

It was also found that increasing the oxygen from 5 to 10% improved the decomposition of absorbed acetaldehyde and TOC, but that decomposition is attenuated when the oxygen concentration is further increased up to 21%. The decomposition of aqueous acetaldehyde is enhanced by the addition of NaOH, but is inhibited by adding HCl, although both additives can increase the absorbability of acetaldehyde into water.

Acknowledgement

We gratefully acknowledge financial support from a Thailand Research Fund [Grant No. PHD/0180/2543 of the Royal Golden Jubilee Ph.D. Program (TRF-RGJ) for K.F. and W.T., and a Research Team Award (TRF-RTA) for W.T. and T.C.] and an AIEJ Student Exchange Program for K.F.

Received: April 8, 2004 [CET 2092]

Symbols used

$C_{i,g}$	[mol-ppm]	inlet concentration of gaseous
•		acetaldehyde
$C_{o,g}$	[mol-ppm]	outlet concentration of
		gaseous acetaldehyde

C_w	$[mol-ppm], [mg L^{-1}]$	concentration of aqueous
1	[mA]	acetaldehyde corona discharge current
[O ₂]	[%]	oxygen concentration
Q_g	\ \ \tau_{\color}	gas flow rate
Q_{l}	[cm³ min-1]	water circulation rate
Re	[-]	Reynold number
TOC	[mg L ⁻¹]	total organic carbon
V	[kV]	applied voltage
W	[cm ³]	water volume
ψ	[-]	removal extent

References

- [1] H. Tamon, H. Mizoata, N. Sano, M. Okazaki, AIChE J. 1995, 41, 1701.
- [2] N. Sano, T. Nagamoto, H. Tamon, T. Suzuki, M. Okazaki, Ind. Eng. Chem. Res. 1997, 36, 3783.
- [3] L. Huang, K. Nakajyo, T. Hari, S. Ozawa, H. Matsuda, Ind. Eng. Chem. Res. 2001, 40, 5481.
- [4] H. Tamon, N. Sano, M. Okazaki, AIChE J. 1996, 42, 1481.
- [5] T. Yamamoto, K. Ramanathan, P. A. Lawless, D. S. Ensor, J. R. Newsome, N. Planks, G. H. Ramsey, IEEE Trans. Ind. Appl. 1992, 28, 528.
- [6] E. M. Van Veldhuizen, Electrical Discharge for Environmental Purposes, Nova Science Publishers, Inc., New York 2000.
- [7] T. Hakoda, M. Yang, K. Hirota, S. Hashimoto, J. Adv. Oxid. Technol. 1998, 3, 79.
- [8] K. Kawamura, Kagaku Kogaku 1989, 53, 820.
- [9] C. R. McLarnon, U. K. Mathur, Ind. Eng. Chem. Res. 2000, 39, 2779.
- [10] N. Sano, T. Nagamoto, H. Tamon, M. Okazaki, J. Chem. Eng. Jpn. 1996, 29, 59.
- [11] A. Mizuno, K. Shimizu, T. Matsuoka, S. Furuta, IEEE Trans. Ind. Appl. 1995, 31, 1463.
- [12] N Sano, D. Yamamoto, T. Kanki, A. Toyoda, Ind. Eng. Chem. Res. 2003, 42, 5423.
- [13] K. Faungnawakij, N. Sano, D. Yamamoto, T. Kanki, T. Charinpanitkul, W. Tanthapanichakoon, Chem. Eng. J. 2004, in press.
- [14] J. Chen, J. H. Davidson, Plasma Chem, and Plasma Proc. 2003, 23, 83.
- [15] R. Peyrous, P. Pignolet, B. Held, J. Phys. D. 1989, 22, 1658.
- [16] R. J. Silbey, R. A. Alberty, Physical Chemistry, John Wiley and Sons Inc., New York 2001.
- [17] J. L. Moruzzi A. V Phelps, J. Chem. Phys. 1966, 45, 4617.
- [18] L. M. Chanin, A. V. Phelps, M. A. Brendi, Phys. Rev. 1962, 128, 219.
- N. I. Butkovskaya, D. W. Setser, J. Phys. Chem. A. 2000, 104, 9428.
 A. Tomas, E. Villenave, R. Lesclaux, J. Phys. Chem. A. 2001, 105, 3505
- [20] A. Tomas, E. Villenave, R. Lesciaux, J. Phys. Chem. A. 2001, 103, 350
- [21] A. Yabe, Y. Mori, K. Hijikata, Amer. Inst. Aeronautics and Astronautics J. 1978, 16, 340.
- [22] N. Sano, T. Kawashima, J. Fujikawa, T. Fujimoto, K. Takaaki, T. Kanki, A. Toyoda, Ind. Eng. Chem. Res. 2002, 41, 5906
- [23] W. F. L. M. Hoeben, Pulsed Corona-Induced Degradation of Organic Materials in Water, Technische Universiteit Eindhoven, Netherlands 2000.
- [24] A. K. Sharma, G. B. Josephson, D. M. Camatoni, S. C. Goheen, Environ. Sci. Technol. 2000, 34, 2267.
- [25] R. B. Bird, W. E. Stewart, E. N. Lightfoot, Transport Phenomena, John Wiley and Sons Inc., New York 1960.
- [26] D. J. Jacob, E. W. Gottlied, M. J. Prather, J. Geophys. Res. 1989, 94, 12975
- [27] L. Bruno, A. R. David, R. B. Deborch, Ozone in Water Treatment, Lewis Publishers Inc., Michigan 1991.
- [28] G. V. Buxton, C. L. Greenstock, W. F. Helman, A. B. Ross, J. Phys. Chem. Ref. Data. 1988, 17, 693.
- [29] N. Sano, T. Fujimoto, T. Kawashima, D. Yamamoto, T. Kanki, A. Toyoda, Sep. Purif. Technol. 2004, 37, 167.
- [30] C. Gottschalk, J. A. Libra, A. Saupe, Ozonation of Water and Waste Water, Wiley-VCH, Weinheim 2000.

Simultaneous Gas-Water Purification by a Wetted-Wall Corona Discharge Reactor: Decomposition of Aqueous Phenol and Gaseous Acetaldehyde

Kajornsak FAUNGNAWAKIJ^{1,2}, Noriaki SANO², Daisuke YAMAMOTO², Tatsuo KANKI², Tawatchai CHARINPANITKUL³ and Wiwut TANTHAPANICHAKOON¹

Department of Chemical Engineering, Chulalongkorn University, Patumwan, Bangkok 10330, Thailand

Department of Mechanical and System Engineering, Himeji Institute of Technology, University of Hyogo, 2167, Shosha, Himeji-shi, Hyogo 671-2201, Japan

Keywords: Corona, Radical, Acetaldehyde, Phenol, Simultaneous Purification

Simultaneous purification of contaminated gas and water by using a cylindrical wetted-wall corona discharge reactor was proposed in this work. Gaseous acetaldehyde and aqueous phenol were chosen as target compounds. The gaseous acetaldehyde was continuously removed from gas stream by absorption into the aqueous phenol solution used for making a wetted-wall. Aqueous phenol and the absorbed acetaldehyde in water were effectively degraded by aqueous radicals, OH, produced by direct contact of gaseous corona with the interfacial water. In addition, ozone partly contributed to decompositions of phenol and some byproducts. The experimental results show that gaseous acetaldehyde can be completely removed from gas mixture when its inlet concentration was in a range of 30 to 200 ppm since decomposition of aqueous acetaldehyde can sustain the absorption of acetaldehyde. This concentration range of acetaldehyde scarcely affected the decomposition of phenol. However, decomposition of total organic carbon (TOC) in water was strongly attenuated when the acetaldehyde concentration is higher than 100 ppm. The influence of the solution pH ranging from 2 to 13 was also investigated.

Introduction

Purification of gaseous pollutants such as volatile organic compounds (VOCs), SO, and NO, using a high-voltage electrical discharge has been developed for several decades, for example D.C. corona discharge (Tamon et al., 1995, 1996), pulsed corona discharge (Yamamoto et al., 1992; Haung et al., 2001), electron beam (Kawamura, 1989), and barrier discharge (Mclarnon and Mathur, 2000). In a D.C. corona discharge technique, low energy electrons are utilized for removal of target gases. The wetted-wall corona discharge reactor was proposed to enhance the removal efficiency by an additional absorption effect to the gas phase reactions (Sano et al., 1996). In this reactor, a thin liquid film flowing on an anode surface can absorb a soluble gas and negative ions produced by electron attachment, ionization, and dissociation of target gases. Recently, the wetted-wall reactor has also been applied for purification of contaminated water (Sano

Received on April 12, 2004. Correspondence concerning this article should be addressed to N. Sano (E-mail address: sano@eng.u-hyogo.ac.jp).

et al., 2003). In this method, the organic contaminants can be effectively decomposed by OH radicals and ozone. In fact, several techniques of electrical discharge have presently been developed for purification of aqueous organic compounds, for example, D.C. corona discharge (Sano et al., 2002, 2003) and pulsed plasma discharge (Grymonpre et al., 1999; Hoeben, 2000; Hayashi et al., 2000).

Combining those performances of the wetted-wall reactor, it can be expected that the reactor can be used for simultaneous purification of gas and water. If the simultaneous purification by this reactor is achieved, not only the cost of the whole process, the operation time and the energy consumption, but also an integrated process can be minimized.

In this study, a cylindrical wetted-wall corona discharge reactor was used for simultaneous purification of aqueous phenol and gaseous acetaldehyde. We investigated the influence of corona discharge current, pH of aqueous solution, concentration of phenol, and that of acetaldehyde. The goal of this work is to examine the feasibility of using the reactor for the simultaneous purification and to optimize the operational conditions.

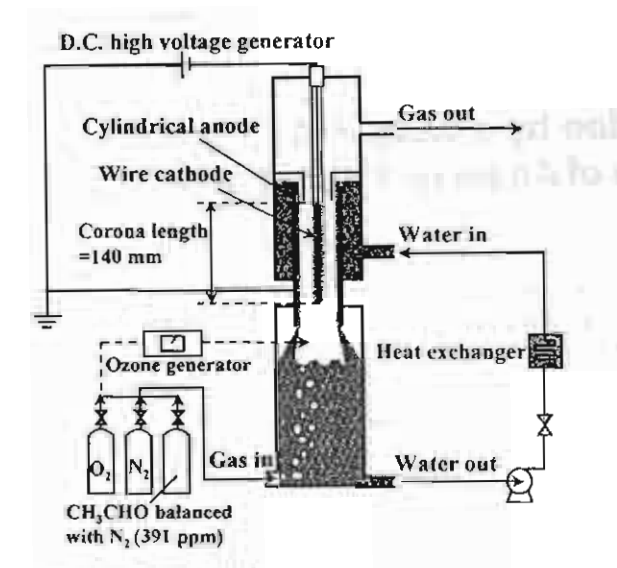


Fig. 1 Schematic diagram of the experimental set-up

1. Experimental

The schematic diagram of the experimental setup is shown in Figure 1. The wetted-wall corona discharge reactor consists of a stainless steel (SUS) wire cathode (0.34 mm diameter) stretched along the axis of an SUS cylindrical anode (34 mm inner diameter; 200 mm length). A D.C. high voltage generator was used to generate a corona discharge by applying the high voltage ranging from -6 to -13 kV to the wire cathode, while the anode was earthed. The axial corona discharge region length was fixed at 140 mm using an insulation tube covering the top part of the eathode wire. Gas mixture of acetaldehyde, oxygen, and nitrogen was fed to the reactor by bubbling into the water reserved below the corona zone at a flow rate of 100 cm3-min-1. The concentrations of acetaldehyde and oxygen in the gas mixture were varied by mixing commercial standard gases. The solution was prepared by dissolving phenol into de-ionized water. The pH of the solution ranging from 2-13 was adjusted by dissolving H,PO, or NaOH. Aqueous phenol was introduced to the corona zone as a falling film, whose thickness was approximately 0.4 mm without corona discharge, on the inner surface of the anode and was circulated at a flow rate of 1400 cm min-1. The temperature of the water was kept at 10°C by using a heat exchanger unit during the operations.

Ozone (O_3) can be produced in the presence of O_2 under the corona discharge in the reactor. In the above experiment, O_3 around 2000 ppm maximum was detected in the treated gas. Thus, the contribution of ozone to the purification of phenol and acctaldehyde was separately evaluated without corona discharge to perform this experiment. O_2 (21 cm³·min⁻¹) was separated from the main gas stream and fed to an ozone genera-

tor to produce ozone at approximately 1%. Subsequently, it was fed to the bottom part of gas corona zone. Whereas the main gas stream, 125 ppm acetal-dehyde balanced with nitrogen at 79 cm³·min⁻¹, was bubbled through the wetted-wall reactor. When the ozone mixed with the main gas stream in the reactor, the ozone concentration was diluted to be approximately 2000 ppm and the total gas flow rate was at 100 cm³·min⁻¹. With these conditions, the concentrations of all gas components became similar to those used in the experiments with the corona discharge.

The gas composition at the inlet and outlet of the reactor were analyzed by a gas chromatograph (GC-9A, Shimadzu Co.) equipped with an FID detector. Gaseous ozone concentration was measured by the KI method. A high performance liquid chromatograph (HPLC) with a UV-VIS detector (SPD-10AVP, Shimadzu Co.) and the FID gas chromatograph were used for analyses of phenol, acetaldehyde, and intermediate products in the circulating water. Total organic carbon (TOC) and pH of the circulating water were measured by a TOC analyzer (TOC-5000, Shimadzu Co.) and a pH meter (pH meter F-22, Horiba Ltd.), respectively.

2. Results and Discussion

2.1 Concept of simultaneous purification

When a corona discharge is applied to the reactor, the energetic electrons are emitted from the wire cathode and accelerated towards the anode along the electric field. During their drift, dissociation and ionization of oxygen can produce O radicals in the high strength electric field adjacent to the cathode as shown in Eq. (1) (Peyrous et al., 1989; Loiseau et al., 1994). In the low strength electric field next to the high electric zone, the dissociative electron attachment to oxygen can also produce O and O- as shown in Eq. (2) (Chanin et al., 1962; Moruzzi and Phelps, 1966). The reaction of oxygen with O radicals would produce ozone as in Eq. (3). When the O and O reach the interfacial water and subsequently react with water molecules, reactive OH radicals are expected to be produced in water as described by Eqs. (4) and (5) (Hoeben et al., 2000; Sano et al., 2002).

$$O_1 + e^- \rightarrow O + O + e^- \tag{1}$$

$$O_1 + e^- \rightarrow O^- + O \tag{2}$$

$$O_3 + O \to O_3 \tag{3}$$

$$O_{(3a)} + H_2O \rightarrow OH_{(3a)} + OH_{(3a)}$$
 (4)

$$O_{(gas)} + H_2O \rightarrow OH_{(aq)} + OH_{(aq)}$$
 (5)

When gas stream is bubbled into the phenol solution, the acetaldehyde is absorbed into the aqueous phenol solution. Then, aqueous solution containing phenol and acetaldehyde flow through the corona zone as a falling thin film on the inner surface of the anode cylinder. In the corona zone, the OH radicals together with ozone simultaneously decompose both aqueous phenol and acetaldehyde.

$$OH_{(aq)}/O_{3(aq)}$$
 + organic compounds (aq) \rightarrow product (6)

The treated solution is circulated through the reactor, while the gas containing acetaldehyde is steadily supplied. By this system, acetaldehyde can be continuously absorbed into the solution since acetaldehyde in water can be continuously degraded. Meanwhile, phenol along with its intermediate products could be completely decomposed to be CO₂ and H₂O as final products by the circulation system.

If the gaseous acetaldehyde is remaining in the gas stream, it is expected that the acetaldehyde is removed in the corona zone by radical reaction (Sano et al., 1997; Butkovskaya and Setser., 2000), ozonation, and cluster formation (Sano et al., 1997).

2.2 Simultaneous purification of aqueous phenol and gaseous acetaldehyde

Concentrations of aqueous phenol, C_{p-1} , aqueous acetaldehyde, C31, and TOC are shown against the discharge time for various inlet concentrations of gaseous acetaldehyde, $C_{a-g inl}$, in Figure 2. Discharge current, I, and applied voltage, V, were 0.3 mA and 11.8 kV, respectively. In Figure 2(a), the concentration of phenol rapidly decreased toward zero within around 3 hrs at the inlet concentration of acetaldehyde in the range of 0-200 ppm. The decomposition rates of phenol were not significantly affected by acetaldehyde in this range. However, it might be possible that the excessively high concentration of acetaldehyde at the inlet could inhibit the decomposition of phenol. Regarding the concentration of aqueous acetaldehyde, Figure 2(b) shows that $C_{s,1}$ slightly increased at the early operation time for all runs and then the $C_{i,j}$ gradually decreases. The higher $C_{a-c \, inl}$ causes higher remaining C_{a-l} .

When decomposition of phenol was conducted without feeding gaseous acetaldehyde, it was found that a small amount of aqueous acetaldehyde was detected from decomposition of phenol within about 5 h. This presence of acetaldehyde corresponds to the C_{a-1} detected when $C_{a-g \, inl}$ was fed to the system at 30 ppm. It was reported that acetaldehyde was one of byproducts in the intermediate pathway of decomposition of phenol by pulsed corona discharge (Hoeben et al., 2000). Moreover, hydroquinone, 1,4-benzoquinone, resorcinol, and pyrocatechol were detected as common intermediate by-products by HPLC during the discharge operation time. These by-products could be completely

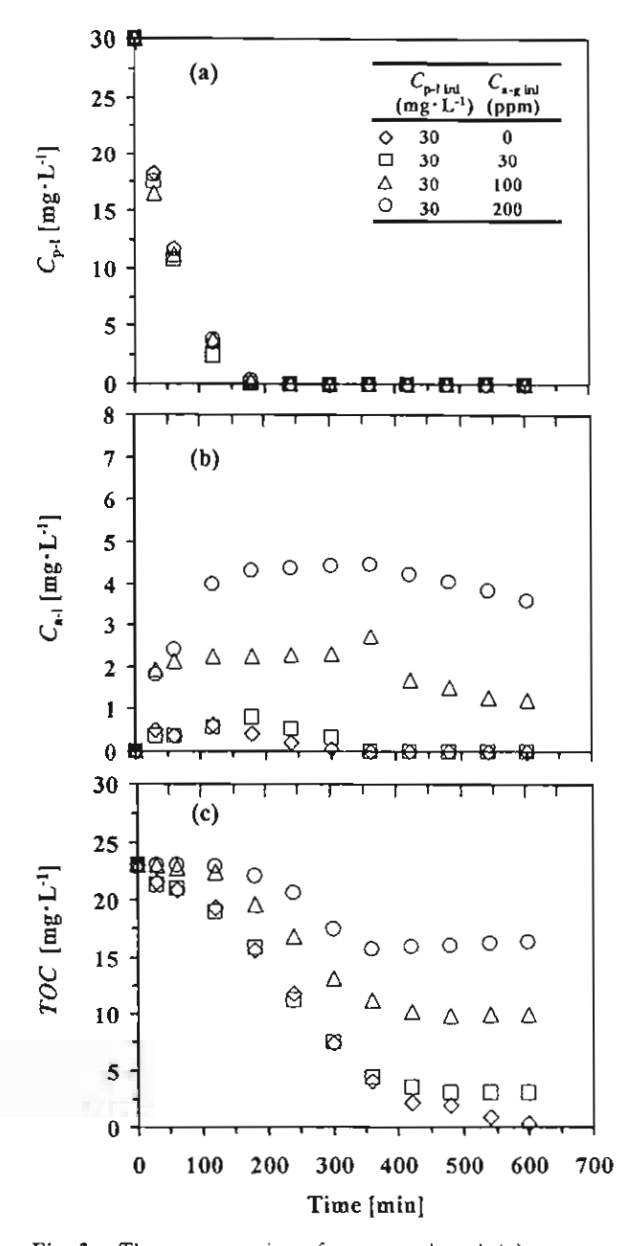


Fig. 2 The concentration of aqueous phenol, (a), aqueous acetaldehyde, (b), and TOC, (c), during corona discharge operation at various inlet concentrations of gaseous acetaldehyde: I = 0.3 mA; $Q_g = 100 \text{ cm}^3 \cdot \text{min}^{-1}$; $Q_1 = 1400 \text{ cm}^3 \cdot \text{min}^{-1}$; $W = 1000 \text{ cm}^3$

mineralized within around 4 hrs. Thus, it was considered that decomposition of phenol along with these intermediates might inhibit the decomposition of absorbed acetaldehyde at the early time operation. However, gaseous acetaldehyde at the outlet was not be detected throughout the discharge operation for all experiments. This suggests that acetaldehyde is completely absorbed into the solution. If the acetaldehyde remains in the gas stream, it could be removed by gas corona reactions. According to the gas analysis by GC, there are no significant gaseous by-products detected

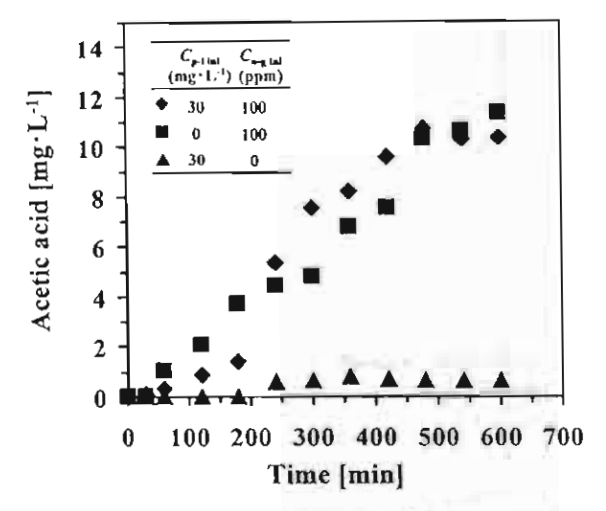


Fig. 3 The concentration of acetic acid during corona discharge operation: I = 0.3 mA; $Q_y = 100 \text{ cm}^3 \cdot \text{min}^{-1}$; $Q_z = 1400 \text{ cm}^3 \cdot \text{min}^{-1}$; $W = 1000 \text{ cm}^3$

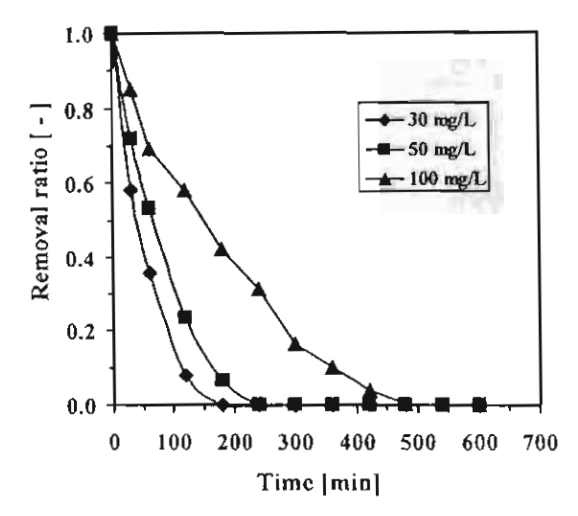


Fig. 4 Removal ratio of aqueous phenol during corona discharge operation at various initial concentrations of phenol: $C_{xy} = 30 \text{ ppm}$; I = 0.3 mA; $Q_y = 100 \text{ cm}^3 \cdot \text{min}^{-1}$; $Q_z = 1400 \text{ cm}^3 \cdot \text{min}^{-1}$; $W = 1000 \text{ cm}^3 \cdot \text{min}^{-1}$

at the outlet gas stream.

Since both phenol and acetaldehyde are converted to other byproducts, TOC are monitored as shown in Figure 2(c). The result shows that TOC can be efficiently degraded when the inlet concentration of acetaldehyde was at 30 ppm. The concentrations of acetaldehyde higher than 100 ppm obviously inhibit the TOC degradation rate. This implies that some stable products are accumulated in the treated water. According to the aqueous analysis by GC and HPLC, the acetic acid was detected as a significant by-product. Acetic acid occupied more than 50% of the residual TOC after 8 h operation time. The concentrations of acetic acid were plotted as a function of time in Figure 3. The

result shows that acetic acid accumulated in water is mainly converted from acetaldehyde rather than phenol. Acetic acid is considered to be a final intermediate product of decompositions of acetaldehyde and phenol.

The removal ratios of phenol at various initial concentrations with fixed 30 ppm $C_{\text{a-g-inil}}$ are depicted in Figure 4. The removal ratio sharply decreases with discharge time. The decreasing rate of removal ratio increases with the lower inlet concentration. The maximum removal rate was found at 30 ppm $C_{\text{p-l-inil}}$. This result suggests that the reactor can be efficiently used for the low concentration of phenol under the present condition.

2.3 pH effect

Figures 5(a)-(c) show the influence of the pH of the solution on the simultaneous purification process in terms of aqueous acetic acid, phenol and acetaldehyde concentration, respectively. H,PO, and NaOH were used to adjust the solution pH at 2 to 13. In Figure 5(a), when pH was raised up to 11, the concentrations of acetic acid significantly decreased. On the other hand, the pH ranging from 2-10 does not strongly affect the decomposition of acetic acid. Not only the decomposition of acetic acid but also the decomposition of aqueous phenol and acetaldehyde are strongly enhanced by adding NaOH as shown in Figures 5(b) and (c). When NaOH is added into the water, dissolved OHwould accelerate the decay of ozone to form hydroxyl radical, OH, which could enhance the decomposition of acetic acid in water (Gottschalk et al., 2000). Furthermore, NaOH might enhance the reactivity of organic compounds in water while H,PO, is considered to be an inert species (Sano et al., 2004).

2.4 Ozonation effect

The influences of direct ozonation on the simultaneous purification are shown in Figure 6. It should be noted that the concentration used here is almost the same as that detected in the simultaneous treatment above. The experimental operation was explained in the experimental section. The removal extent of acetal-dehyde ψ , is defined as

$$\psi = \frac{C_{\text{a-g inf}} - C_{\text{a-g out}}}{C_{\text{a-g out}}} \tag{7}$$

where $C_{\text{a-g inl}}$ and $C_{\text{a-g out}}$ are the inlet and outlet concentrations of gaseous acetaldehyde, respectively. In Figure 6(a), the removal extent of gaseous acetaldehyde is shown against time. Without corona current, the removal extent gradually decreases with time since the absorbed acetaldehyde in water inhibits the absorption rate. With ozonation, the removal extent decreases slightly slower than that obtained by absorption. This result shows that direct ozonation does not significantly contribute to the removal of gaseous acetaldehyde. In

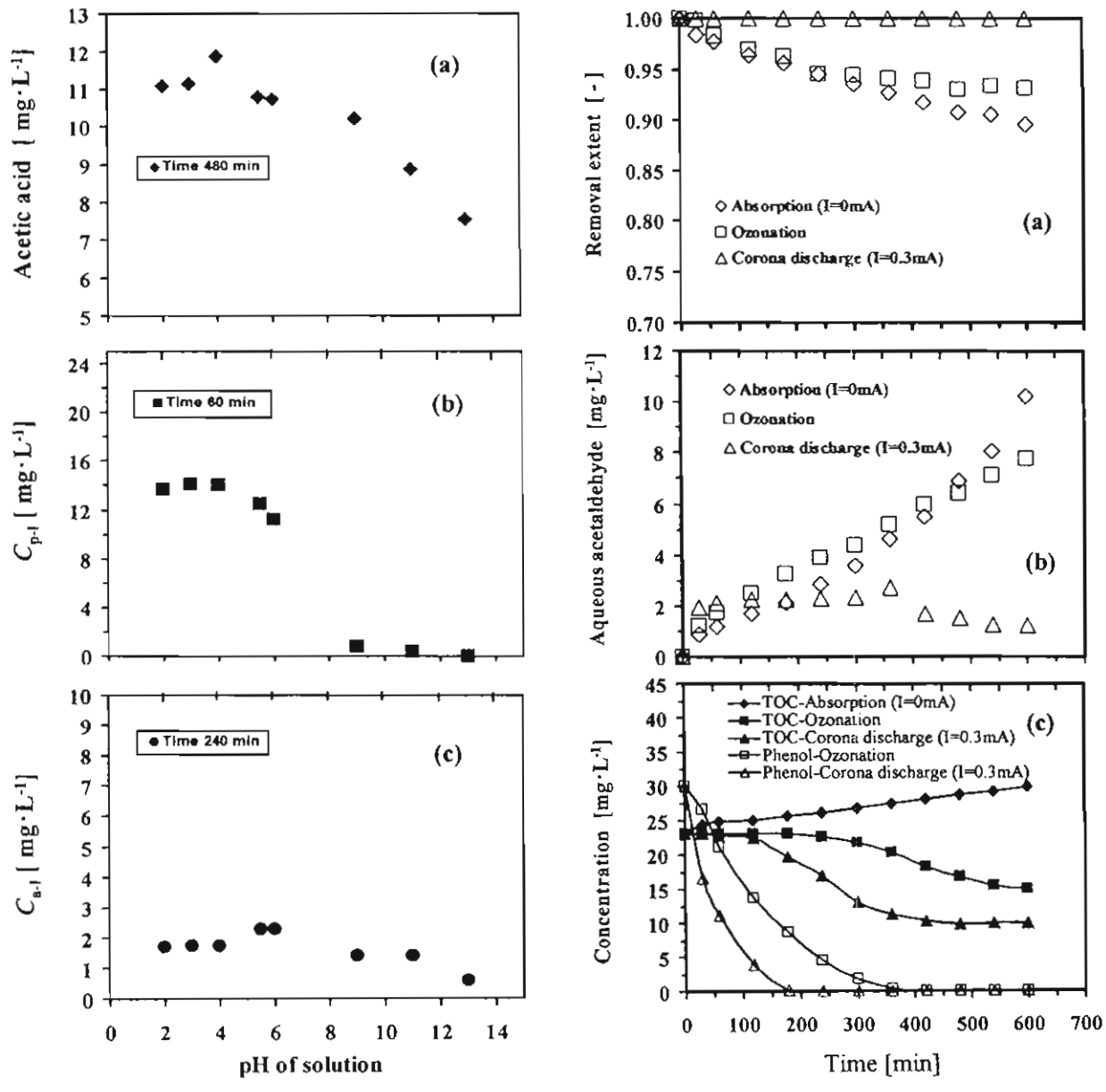


Fig. 5 Influence of pH of solution on the simultaneous purification: (a) aqueous acetic acid concentration at 480 min; (b) aqueous phenol concentration at 60 min; (c) aqueous phenol concentration at 240 min; $C_{\text{p-1-in}} = 30 \text{ mg} \cdot \text{L}^{-1}$; $C_{\text{a-g-in}} = 100 \text{ ppm}$; I = 0.3 mA; $Q_{\text{g}} = 100 \text{ cm}^3 \cdot \text{min}^{-1}$; $Q_{\text{l}} = 1400 \text{ cm}^3 \cdot \text{min}^{-1}$; $W = 1000 \text{ cm}^3$

Fig. 6 Influence of ozonation on the simultaneous purification during operation: (a) removal extent of gaseous acetaldehyde; (b) aqueous acetaldehyde concentration; (c) TOC and phenol concentrations in water: $C_{p-1 \text{ ini}} = 30 \text{ mg} \cdot \text{L}^{-1}$; $C_{\text{a-g ini}} = 100 \text{ ppm}$; I = 0.3 mA; $Q_g = 100 \text{ cm}^3 \cdot \text{min}^{-1}$; $Q_1 = 1400 \text{ cm}^3 \cdot \text{min}^{-1}$; $W = 1000 \text{ cm}^3$

contrast, when the corona discharge is generated, the removal extent can reach 100% through the operation time. Figure 6(b) shows the concentration of aqueous acetaldehyde during operation. As expected, with ozonation, the concentration of acetaldehyde increases with time, resulting in the increase of the outlet concentration of gaseous acetaldehyde. When the corona discharge is generated, the concentration of aqueous acetaldehyde can be kept almost constant, resulting in

a steady state removal extent of gaseous acetaldehyde.

Figure 6(c) shows the concentration of phenol and TOC in water against operation time. The result shows that ozone can completely decompose phenol within around 6 h, approximately 2 times slower than corona discharge. However, TOC degradation by ozonation gently decreases compared with that by corona discharge because acetic acid cannot effectively be decomposed by direct ozonation. The effect of direct

VOL. 37 NO. 11 2004

ozonation is not significant in the corona discharge system studied here.

Conclusions

In this work, simultaneous purification of gas and water was experimentally investigated by using a wetted-wall corona discharge reactor. Gaseous acetaldehyde and aqueous phenol were chosen as target contaminants. It is found that gaseous acetaldehyde can completely be removed from gas stream throughout the operation when its inlet concentration is ranging from 30 to 200 ppm. Simultaneously, aqueous phenol can completely be decomposed within about 3 h when its initial concentration is at 30 ppm. The inlet concentration of acetaldchyde ranging from 30 to 200 ppm does not play a significant role on the decomposition of phenol. However, when the inlet concentration of gaseous acetaldehyde was higher than 100 ppm, degradation of TOC in water was considerably retarded. This is because acetic acid is accumulated in the aqueous solution. The increase of initial concentration of phenol causes the decrease of its removal ratio. There are no significant by-products detected in the treated gas stream. The influence of pH ranging from 2 to 13 was investigated by adding NaOH and H,PO. The result shows that the decomposition of acetic acid is drastically increased when the pH is raised up to 11. Whereas, pH lower than 11 does not significantly affect the decomposition of acetic acid in water. The influence of direct ozonation is not significant in the present study.

Acknowledgment

The authors would like to acknowledge the financial support from the Thailand Research Fund [Grant No. PHD/0180/2543 of Royal Golden Jubilee Ph.D. Program (TRF-RGJ) for K.F. and W.T., and Research Team Award (TRF-RTA) for W.T. and T.C.] and the AIEJ Student Exchange Program for K.F.

Nomenclatures

to the straining			
C_{a1}	=	concentrations of aqueous acetaldehyde	[mg·L-1]
$C_{\text{a-g and}}$	=	inlet concentrations of gaseous acetalde	hyde
			(ppm)
C ser out	=	outlet concentrations of gaseous acetald	ehyde
			(ppm)
$C_{\alpha 1}$	=	concentrations of aqueous phenol	[mg.L-1]
C _{p-1 ini}	=	initial concentrations of aqueous pheno.	[mg-L-1]
D.C.	=	direct current	
1	=	corona discharge current	[mA]
Q_{\bullet}	=	gas flow rate [c	:m³·miu-1]
Q_{k} Q_{i} TOC	=	water circulation rate [6	[1-nim ³ mis
TOC	=	total organic carbon	$[mg\cdot L^{-1}]$
V	=	applied voltage	[kV]
W	=	water volume	[cm]
W	=	removal extent	(1

Literature Cited

Butkovskaya, N. I. and D. W. Setser; "Infrared Chemiluminescence Study of Reaction of Hydroxyl Radical with Acetaldehyde and the Secondary Reactions of Acetyl Radical with NO₂, OH, and

- H," J. Phys. Chem. A., 104, 9428-9435 (2000)
- Chanin, L. M., A. V. Phelps and M. A. Brondi; "Measurement of the Attachment of Low-Energy Electrons to Oxygen Molecules," *Physical Review*, 128, 219-230 (1962)
- Gottschalk, C., J. A. Libra and A. Saupe; Ozonation of Water and Waste Water, Wiley-VCH, Weinheim, German (2000)
- Grymonpre, D. R., W. C. Finey and B. R. Locke; "Aqueous-phase Pulsed Streamer Corona Reactor Using Suspended Activated Carbon Particles for Phenol Oxidation: Model-Data Comparison," Chem. Eng. Sci., 54, 3095-3105 (1999)
- Haung, L., K. Nakajo, S. Ozawa and H. Masuda; "Decomposition of Dichloromethane in a Wire-in-Tube Pulsed Corona Reactor," Environ. Sci. Technol., 35, 1276-1281 (2001)
- Hayashi, D., W. F. L. M. Hoeben, G. Dooms, E. M. Van Veldhuizen, W. R. Rutgers and G. M. W. Kroesen; "Influence of Gaseous Atmosphere on Corona-Induced Degardation of Aqueous Phenol." J. Phys. D: Appl. Phys., 33, 2769-2774 (2000)
- Hoeben, W. F. L. M.; Pulsed Corona—Induced Degradation of Organic Materials in Water, Technische Universiteit Eindhoven, Eindhoven, the Netherlands (2000)
- Kawamura, K.; "Simultaneous Removal of NO_x and SO_x by Electron Beam," Kagaku Kogaku, 53, 820-821 (1989)
- Loiseau, J. F., F. Lacassie, C. Monge, R. Peyrous, B. Held and C. Coste; "Numerical Simulation of Ozone Axial and Radial Distribution in a Cylindrical Oxygen-Fed Ozonizer," J. Phys. D: Appl. Phys., 27, 63-73 (1994)
- Mclarnon, C. R. and U. K. Mathur; "Nitrogen Oxide Decomposition by Barrier Discharge," Ind. Eng. Chem. Res., 39, 2779-2787 (2000)
- Moruzzi, J. L. and A. V. Phelps; "Survey of Negative-Ion-Molecule Reactions in O₂, CO₂, H₂O, CO, and Mixtures of These Gases at High Pressures," J. Chem. Phys., 45, 4617-4627 (1966)
- Peyrous, R., P. Pignolet and B. Held; "Kinetic Simulation of Gaseous Species Created by an Electrical Discharge in Dry or Humid Oxygen." J. Phys. D: Appl. Phys., 22, 1658-1667 (1989)
- Sano, N., T. Nagamoto, H. Tamon and M. Okazaki; "Removal of Iodine and Methyl Iodide in Gas by Wetted-Wall Reactor Base on Selective Electron Attachment," J. Chem. Eng. Japan, 29, 59-64 (1996)
- Sano, N., T. Nagamoto, H. Tamon, T. Suzuki and M. Okazaki; "Removal of Acetaldehyde and Skatole in Gas by Corona-Discharge Reactor," Ind. Eng. Chem. Res., 36, 3783-3791 (1997)
- Sano, N., T. Kawashima, J. Fujikawa, T. Fujimoto, T. Kitai, T. Kanki and A. Toyoda; "Decomposition of Organic Compounds in Water by Direct Contact of Gas Corona Discharge: Influence of Discharge Conditions," Ind. Eng. Chem. Res., 41, 5906-5911 (2002)
- Sano, N., D. Yamamoto, T. Kanki and A. Toyoda; "Decomposition of Phenol in Water by Cylindrical Wetted-Wall Reactor Using Direct Contact of Gas Corona Discharge," Ind. Eng. Chem. Res., 42, 5423-5428 (2003)
- Sano, N., T. Fujimoto, T. Kawashima, D. Yamamoto, T. Kanki and A. Toyoda; "Influence of Dissolved Inorganic Additives on Decomposition of Phenol and Acetic Acid in Water by Direct Contact of Gas Corona Discharge," Sep. Purif. Technol., 37, 169-175 (2004)
- Tamon, H., H. Mizota, N. Sano and M. Okazaki; "New Concept of Gas Purification by Electron Attachment," AIChE J., 41, 1701– 1711 (1995)
- Tamon, H., N. Sano and M. Okazaki; "Influence of Oxygen and Water Vapor on Removal of Sulfur Compounds by Electron Attachment," AIChE J., 42, 1481-1486 (1996)
- Yamamoto, T., K. Ramanathan, P. A. Lawless, D. S. Ensor, J. R. Newsome, N. Planks and G. H. Ramsey; "Control of Volatile Organic Compounds by an AC Energized Ferroelectric Pellet Reactor and a Pulsed Corona Reactor," *IEEE Trans. Ind. Appl.*, 28, 528–534 (1992)

- [5] Matsuo Y, Fukutsuka T, Sugie Y. Photochemical dimerization of acenaphtylene in surfactant-intercalated graphite oxide. Carbon 2002;40:958-61.
- [6] Matsuo Y, Fukunaga T, Fukutsuka T, Sugic Y. Photochemical dimerization of acenaphthylene in hydrophobized graphite oxide. Mol Cryst Liq Cryst 2002;386:45-50.
- [7] Matsuo Y, Fukunaga T, Tokura N, Fukutsuka T, Sugie Y. Photochemical dimerization of acenaphthylene in hydrophobized graphite oxide (II). Trans Mat Res Soc Jpn 2003;28:589-95.
- [8] Matsuo Y, Fukunaga T, Tokura, N, Fukutsuka T, Sugic Y. Control of photochemical dimerization of acenaphtylene in graphite oxide intercalated by n-alkylamines with different alkyl chain length. Trans Mat Res Soc Jpn, in press.
- [9] Dékány I, Küger-Grasser R, Weiss A. Selective liquid sorption properties of hydrophobized graphite oxide. Colloid Polym Sci 1988;276:570-6.
- [10] Matsuo Y, Hatase K, Sugie Y. Selective intercalation of aromatic molecules into alkyltrimethylammonium ion-intercalated graphite oxide. Chem Lett 1999:1109-10.

- [11] Matsuo Y, Hatase K, Sugie Y. Monomer emission from pyrene adsorbed in surfactant-intercalated graphite oxide. Chem Commun 1999:43-4.
- [12] Bourlinos AB, Gournis D, Petridis D, Szabó T, Szeri A, Dékány I. Graphite oxide: chemical reduction to graphite and surface modification with primary aliphatic amines and amino acids. Langmuir 2003;19:6050-5.
- [13] Ogawa M, Okumoto S, Kuroda K. Control of interlayer microstructures of a layered silicate by surface modification with organochlorosilanes. J Am Chem Soc 1998;120:7361-2.
- [14] Ogawa M, Miyoshi M, Kuroda K. Perfluoroalkylsilylation of the interlayer silanol groups of a layered silicate, magadite. Chem Mater 1998;10:3787-9.
- [15] Fujita I, Kuroda K, Ogawa M. Syntehesis of interlamellar silylated derivatives of magadiite and the adsorption for aliphatic alcohols. Chem Mater 2003;15:3134-41.
- [16] Brodie MBC. Sur le poids atomique du graphite. Ann Chim Phys 1860:59:466-72.
- [17] Scholz W. Boehm HP. Betrachtungen zur struktur des graphitoxids. Z Anorg Allg Chem 1969;369-327-40.

Formation of unique nanowhiskers on carbon gels

Nattaporn Tonanon a.*, Wiwut Tanthapanichakoon a, Takuji Yamamoto b, Hiromoto Nishihara c, Shin R. Mukai c, Hajime Tamon c

Department of Chemical Engineering, Faculty of Engineering, Chulalongkorn University, Phayathai, Bangkok 10330, Thailand
 National Institute of Advanced Industrial Science and Technology, 1-1-1 Higashi, Tsukuba 305-8565, Japan

Department of Chemical Engineering, Graduate School of Engineering, Kyoto University, Katsura, Kyoto 615-8510, Jupan

Received 29 September 2003; accepted 18 March 2004 Available online 6 May 2004

Keywords: A. Whiskers; B. Pyrolysis; C. Adsorption; D. Scanning electron microscopy; E. Surface properties

Pekala et al. firstly synthesized RF carbon gels from sol-gel polycondensation of resorcinol (R) and formal-dehyde (F) with sodium carbonate (C) as a basic catalyst [1-3]. From its high BET surface area, $S_{\rm BET}$, and large mesopore volume, $V_{\rm mes}$, RF carbon gels are interesting porous materials, which are suitable for many applications such as column packing materials for high-performance liquid chromatography, electrode materials and materials for catalyst supports. Apart from previous works on RF gels or carbon gels [1-5], in the present work nanowhiskers are first found on the surface of carbon gel prepared by using RF gel as a precursor.

In general, well-developed methods such as electric arc discharge, laser evaporation, and a well-round chemical vapor deposition (CVD) are used to prepare nanowhiskers/nanofibers [6]. In CVD process, the whiskers or fibers grow by decomposing hydrocarbons or carbon monoxide with assistance of mono- or bime-

E-mail address: nattaporn.t@chula.ac.th (N. Tonanon).

tallic catalysts, typically Fe, Ni, Co and Ni-Cu [6,7]. Apart from the normal nanowhisker or nanofiber formation [6-11], unique nanowhiskers are obtained by using neither external carbon source nor additional metal catalyst in the present work.

In order to prepare RF hydrogels, resorcinol-formaldehyde (RF) solutions were prepared from resorcinol $(C_6H_4(OH)_2)$ (R), formaldehyde (HCHO) (F), sodium carbonate (Na₂CO₃) (C) and distilled water (W). All chemicals are research grades from Wako Pure Chemical Industries Inc. Na2CO3 and distilled water were used as a basic catalyst and a diluent, respectively. The synthesis conditions are presented in Tables 1 and 2. Here the molar ratio of resorcinol to formaldehyde (R/F) was fixed at 0.5. The molar ratios of resorcinol to catalyst (R/C) were 100 and 400 mol/mol and the ratios of resorcinol to water (R/W) were 0.5 and 0.25 g/cm³. The prepared RF solutions were first kept at gelation temperature, T_{gel} , and the sol-gel transition continues. RF hydrogels synthesized in this work were in the forms of rod and sphere. The RF rod gels were prepared by pouring RF solution into the cylindrical glass tube

^{*}Corresponding author, Tel.: +66-22-18-68-65; fax: +66-22-18-68-77.

Table 1 Synthesis conditions and porous properties of cryogels

	R/C (mol/mol)	R/W (g/cm3)	C/W (mol/m³)	$S_{\rm BET}$ (m ² /g)	Vmes (cm ³ /g)
U450	100	0.50	45	70	0.02
U600	400	0.25	6	590	0.33

Sphere shape, aging time: 1-4 weeks, Tpel = 298 K.

Table 2
Synthesis conditions and porous properties of carbon gel and Na₂CO₃-doped carbon gels

	Na ₂ CO ₃ amount doped ³ (g)	Keeping time ^b (d)	C/W (mol/m ³)	$S_{\rm HET}$ (m ² /g)	$V_{\rm mes}$ (cm ³ /g)
T6	Non	Non	6	720	0.90
T16	0.16	9	>6	380	0.52
T60	0.60	9	>6	400	0.42

Rod shape, R/C = 400 mol/mol, R/W = 0.25 g/cm³, T_{gel} = 333 K.

"Na₂CO₃ amount doped in 25 cm³ water.

b Keeping time after doping.

(inner diameter = 4 mm, length = 40 mm) [4,5]. For the preparation of RF sphere, before RF solution lost its fluidity, it was dropped into cyclohexane by using a syringe and RF spheres were formed. RF rods and spheres were aged at 298 K for 24 h. Before freeze drying, water in RF hydrogels was replaced by solvent exchange with t-butanol for three times. The RF hydrogels were kept at 323 K in t-butanol for 1-4 weeks in





Fig. 1. SEM micrographs of carbon cryogel surface.

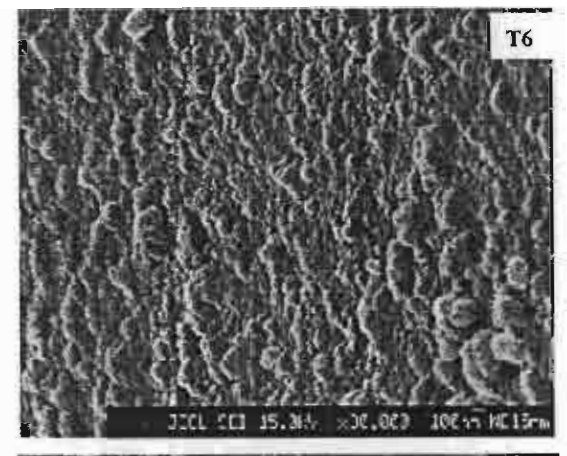
a glass vial tightly sealed with Teflon tape. After that, RF hydrogels were freeze dried at 263 K for 4 days to obtain RF cryogels.

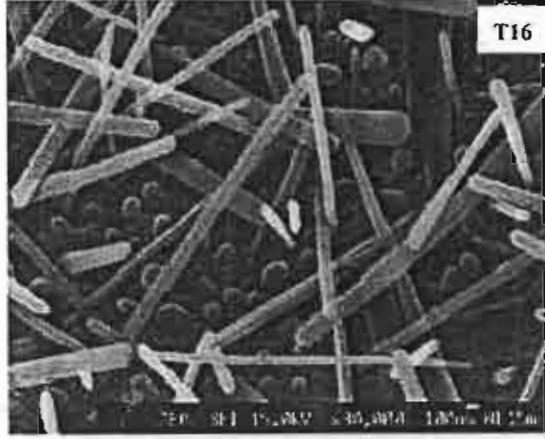
RF carbon gels were obtained by pyrolyzing RF cryogels at 1273 K. Pyrolysis was conducted under a 200 cm³-STP/min flow of argon gas. At first, the RF cryogels were heated to 523 K at a constant heating rate of 250 K/h, and were kept at this temperature for 2 h. Then they were heated to 1273 K at a constant heating rate of 250 K/h and were kept at 1237 K for 4 h.

The porous properties of RF carbon gels were determined by the N₂ adsorption method using an adsorption apparatus (BEL Japan Inc; BELSORP28) [4,5]. The surface and cross section of carbon cryogel were observed by a scanning electron microscope (JEOL, Ltd., JSL-6340FS).

SEM micrographs of carbon gel (U450) listed in Table 1 are shown in Fig. 1. Nanowhiskers can be observed only on the surface of RF carbon gel (U450). On the other hand, there are no nanowhiskers on the surface of RF organic gels (U450 and U600) before pyrolysis and RF carbon gel (U600). These results show that nanowhiskers are formed only on the surface of RF carbon gel prepared under high catalyst concentration (C/W=45). Fig. 1 also shows that the nanowhiskers (U450 at 100,000 magnifications) are formed by connection of primary nanoparticles.

In order to confirm the effect of catalyst concentration in RF gel, Na_2CO_3 was doped to the RF gel of T6, on which the nanowhiskers were not formed after pyrolysis. RF gels of T6 were immersed in an aqueous solution of two different catalyst (Na_2CO_3) concentrations under conditions as shown in Table 2. From Table 2, it can be found that the Na_2CO_3 doping decreases both S_{BET} and V_{mes} of the RF carbon gel. These results confirm that the catalyst can be doped to the gels. After doping followed by freeze drying and pyrolysis, nanowhiskers are observed only on carbon rods prepared by





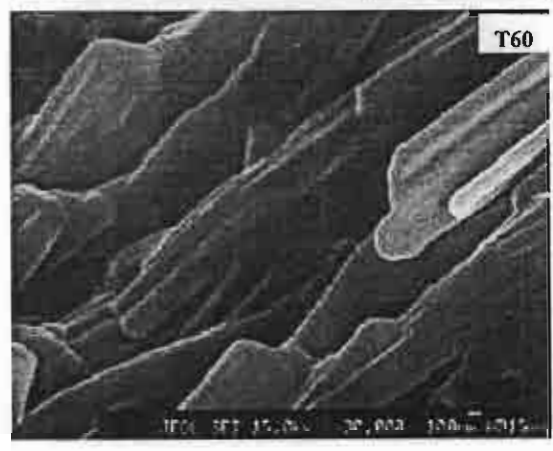


Fig. 2. SEM micrographs of carbon cryogel surface prepared by doping Na₂CO₃ solution to RF gel.

doping T6 with Na₂CO₃ solution as shown in Fig. 2. One can see that when the Na₂CO₃ doping concentration is high, the thick nanowhiskers are formed. These results together with previous result suggest that the catalyst (Na₂CO₃) concentration (in both starting RF solution and final catalyst concentration of RF gel) has an effect on the nanowhisker formation.

In the present investigation, it is found that the unique nanowhiskers are formed on the surface of RF carbon gel after pyrolysis of RF gel prepared with appropriate concentration of Na₂CO₃ used as a catalyst in the sol-gel polycondensation of resorcinol and formaldehyde. Neither external carbon source nor additional metal catalyst is needed for this unique nanowhisker formation. However, more investigations are needed to understand more about the novel nanowhiskers.

Acknowledgements

This research was partially supported by Thai Government (Matching Fund), the Thailand Research Fund (Senior Researcher Scholarship), Thai-Japan Technology Transfer Project (TJTTP), Silver Jubilee Research Fund, Chulalongkorn University, National Metal and Materials Technology Center (Thailand), Japan Society for the Promotion of Science, Grant-in-Aid for Scientific Research (B), No. 14350416 (2002) and Industrial Technology Research Grant Program in 2001 from New Energy and Industrial Technology Development Organization (NEDO) of Japan.

References

- Pekala RW. Organic acrogels from the polycondensation of resorcinol with formaldehyde. J Mater Sci 1989;24:3221-7.
- [2] Pekala RW, Alviso CT. Carbon aerogels and xerogels. Mater Res Soc Symp Proc 1992;270:3-14.
- [3] Al-Muhtaseb SA, Ritter JA. Preparation and properties of resorcinol-formaldehyde organic and carbon gels. Adv Mater 2003;15:101-14.
- [4] Tamon H, Ishizaka H, Mikami M, Okazaki M. Porous structure of organic and carbon aerogels synthesized by sol-gel polycondensation of resorcinol with formaldchyde. Carbon 1997;35:791-6.
- [5] Tamon H, Ishizaka H, Yamamoto T, Suzuki T. Preparation of mesoporous carbon by freeze drying. Carbon 1999;37:2049-55.
- [6] Singh C, Quested T. Boothroyd CB, Thomas P, Kinloch IA, Abou-Kandil AI, et al. Synthesis and characterization of carbon nanofibers produced by the floating catalyst method. J Phys Chem B 2002;106:10915-22.
- [7] Che G, Lakshmi BB, Martin CR, Fisher ER. Chemical vapor deposition based synthesis of carbon nanotubes and nanofibers using a template method. Chem Mater 1998;10:260-7.
- [8] Terrones M, Terrones H, Grobert N, Hsu WK, Zhu YQ, Hare JP, et al. Efficient route to large arruys of CNx nanofibers by pyrolysis of ferrocene/melamine mixtures. Appl Phys Lett 1999;75:3932 4.
- [9] Cooper CA, Ravich D, Lips D, Mayer J, Wagner HD. Distribution and alignment of carbon nanotubes and nanofibrils in a polymer matrix. Compos Sci Technol 2002;62:1105-12.
- [10] Steigwalt ES, Deluga GA, Cliffel DF, Lukehart CM. A Pt-Ru/ graphitic carbon nanofiber nanocomposite exhibiting high relative performance as a direct-methanol fuel cell anode catalyst. J Phys Chem B 2001;105:8097-101.
- [11] Park JG, Kim GT, Park JH, Yu HY, McIntosh G, Krstic V, et al. Quantum transport in low-dimensional organic nanostructures. Thin Solid Films 2001;393:161-7.

Investigation of Fluid and Coarse-Particle Dynamics in a Two-Dimensional Spouted Bed

By Thanit Swasdisevi*, Wiwut Tanthapanichakoon, Tawatchai Charinpanitkul, Toshihiro Kawaguchi, Toshitsugu Tanaka, and Yutaka Tsuji

The aerodynamics of particles and gas flow in a two-dimensional spouted bed (2DSB) with draft plates is investigated with the aid of the discrete element method. The geometry of the 2DSB with draft plates is set as close as possible to the experimental apparatus of Kudra [1] and Kalwar [2]. The physical properties of the coarse particles are similar to those of shelled corn. The calculated minimum spouting velocity and pressure drop agree well with the correlations of Kudra [1] and Kalwar [2]. In the spout region, the particle vertical velocities are found to decrease as the height increases. The fluid velocity in the downcomer region decreases as the superficial gas velocity increases. The particle circulation rate indreases when the friction coefficient decreases or the separation height increases. At the minimum spouting velocity, the bed height does not affect the particle circulation rate in the 2DSB with draft plates. The draft plates not only reduce the minimum spouting velocity and pressure drop but also increase the maximum spoutable bed height. The effect of staking out the draft plates on the spouting phenomenon is investigated and the effect of putting in a deflector on the possible treakage of the particles is also estimated.

1 Introduction

The spouted bed has been established as an alternative to the fluidized bed for the handling of particulates, which are coarse and monodisperse in size. Spouted beds are widely used in industry, e.g., for the drying of granular materials granulation of powders, coating of tablets and blending of solids. The conventional spouted bed is formed in a contral or conical-cylindrical vessel having a small or mind for gas injection at the center of its bottom. The injected biglivelocity gas lifts and carries particles upwards through the central part of the bed. After reaching a certain height above the peripheral bed level, these particles fallias a loosely packed bed into the downcomer region between the hollowed core and the vessel wall. Therefore, the overall bed is composed of a dilute phase in the central core (spout region) through which the particles are lifted and moved upwards by the injected gas and a dense phase (downcomer) between the spout region and the vessel wall through which the particles move down. The combination of these two distinct flow regimes, a pneumatic transport through the bed center (in the spout) and a falling bed in the downcomer, results in an internal circulation of the solids, which is characteristic of the spouted bed. In the drying operation, this intensive particle circulation results in more nearly uniform moisture content and bed temperature while the high velocity of the injected gas allows the use of high gas temperature with little thermal degradation of the product. Although the spouted bed requires a relatively high pressure drop prior to the onset of spouting and a high inlet gas velocity (though lower

volumetric flow rate than the fluidized bed), the resulting high insimal efficiency makes this technique economically feasible under numerous conditions [3].

The literature on conical-cylindrical spouted beds (CSBs) in shown that the continuous movement of particles has a significant effect on the performance of the spouted beds in industrial applications, such as drying, coal gasification, granulation and particle coating. However, the CSBs are rarely used in the postharvest industry because of scaleup and operating difficulty [4]. In an attempt to overcome some of the limitations of the CSBs, Mujumdar [4] proposed the idea of a two-dimensional spouted bed (2DSB). As shown in Fig. 1, a typical 2DSB consists of two planar walls with a slanting base and has a gas entry slot at the center of the width of the bed bottom. The thin rectangular geometry makes the 2DSB easier for scaleup than a cylindrical bed.

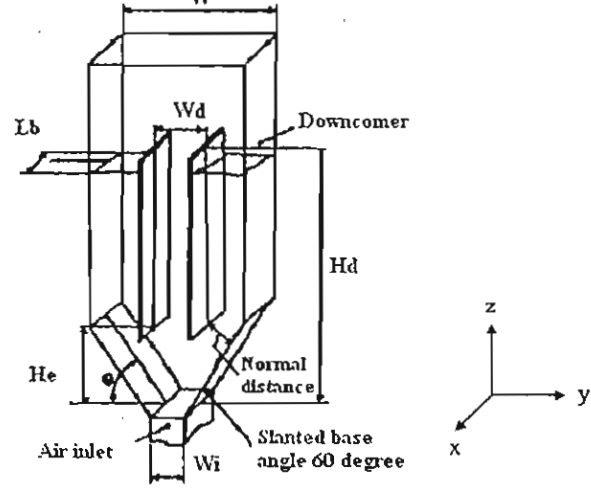


Figure 1. Schematics of the two-dimensional spouted bed.

^[*] T. Swasdisevi (e-mail: ithasevi@yahoo.com), W. Tanthapanichakoon, T. Charinpanitkul, Department of Chemical Engineering, Faculty of Engineering, Chulalongkorn University, Patumwan, Bangkok 10330, Thailand; T. Kawaguchi, T. Tanaka, Y. Tsuji, Department of Mechanophysics Engineering, Faculty of Engineering, Osaka University, 2-1 Yamada-oka, Suita, Osaka 565-0871, Japan.

Adding identical units in the orthogonal direction can readily scale up production capacity. Therefore, a laboratory-scale apparatus can be considered to be a single unit in a complex of similar units. In order to eliminate backmixing, stabilize solids circulation and reduce the bed pressure drop, draft plates are frequently inserted in the core of the spouted bed to separate the spout region from the downcomer region [1].

Nowadays, computational techniques are popular and often used to simulate multiphase flows, including diluteand dense-phase gas-solid flows. The discrete element method (DEM) is a powerful tool for getting detailed information on these complex phenomena without physically disturbing the flows. A distinct advantage of carrying out DEM simulation of the spouted bed over the traditional use of the twofluid models is that the former is capable of elucidating the bed dynamics at the individual particle level [5]. Tsuji et al. [6-9] successfully applied the DEM to plug flows in a horizontal pipe, two-dimensional fluidized bed and a cylindrical spouted bed with slanting base. They found that the calculated results on the formation of bubbles and slugs, particle mixing, and velocity profiles of the particles agreed well with experimental observations. Horio et al. [10-13] successfully applied DEM to an investigation of the hot-spot formation on the distributor near the wall of a fluidizing column in which polymerization reaction is taking place, the behavior of particles and bubbles around the immersed tubes in afluidized bed at high temperature and pressure, and the meeting nism of agglomeration in a fluidized bed Van Nierop [14] used DEM to investigate the charge motion of a mill and found that the simulation results predicted well the power draft and the charge motion of the mill at speeds below the critical value. Rhodes [5] applied DEM to the investigation of mixing in gas-fluidized beds. The results indicated that the rate of solids mixing increased as the gas velocity increased but the degree of mixing achievable was unaffected. While the initial rate of mixing was found to be insensitive to the particle size, the overall rate of mixing and the resulting degree of mixing were found to decrease as the particle size increased. Although the 2DSB with draft plates is expected to benefit the postharvest industry, there has been little detailed information on particle dynamics and gas flow, while their measurements without causing undesirable disturbances in the 2DSB are experimentally difficult.

Corn is an economically important agricultural produce for Thailand and many other countries. The demand for corn is high, especially in the feed milling and food industries. Modern agricultural technology has been developed to solve the problem of shortage of corn. Consequently, a huge quantity of corn is often produced within a short period of time, thus resulting in poor corn quality and infection with aflatoxin B-1 in corn with high moisture content. In this situation, sun drying is generally unreliable because it depends on weather conditions. Therefore, the fluidized bed and spouted bed dryers are often employed because of the small area required for installation.

In this work, DEM is used to investigate the aerodynamics of coarse particles in a 2DSB with draft plates. The properties of the particles are set close to the corn particles. As explained above, the 2DSB is selected because it is suitable for coarse heat-sensitive particles. Detailed information, such as minimum spouting velocity, pressure drop, spatial distributions of particle velocity and particle circulation rate, is analyzed and presented. The effects of the draft plates and the separation height (H_e in Fig. 1) are also investigated. Such information will be useful for the design of a 2DSB dryer in the postharvest industry.

2 Governing Equation

2.1 Fluid Motion

The fluid motion is calculated two-dimensionally in the vertical (y,z) plain. The locally averaged equation of continuity and equation of motion (Navier-Stokes equation) are used to calculate the fluid motion. All local quantities of the fluid in acalculation cell such as pressure and velocity are represented by uniform values. Thus, the void fraction of each cell can be calculated from the total volume of particles contained in it. In this way, the position and velocity of individual particles are not of concern in the equation of fluid motion. Only the local total volume of the particles and their locally averaged velocities are considered. The equations for the fluid motion are as follows¹⁾:

Equation of continuity:

$$\frac{\partial}{\partial t}\varepsilon + \frac{\partial}{\partial x_i}\left(\varepsilon u_j\right) = 0\tag{1}$$

Equation of motion:

$$\frac{\partial}{\partial t} \left(\varepsilon u_i \right) + \frac{\partial}{\partial x_i} \left(\varepsilon u_i u_j \right) = -\frac{\varepsilon}{\rho_x} \frac{\partial p}{\partial x_i} + f_{pi} \tag{2}$$

For inviscid flow, the laminar and turbulent velocity distribution inside a thin rectangular duct is essentially flat because there is no viscous effect at the two neighboring side walls. It is well known that the velocity distribution of fluid flowing through a packed bed is relatively flat. Therefore, the fluid flow in this simulation is assumed to be inviscid because of the presence of the particles. Although the concentration of the particles in the spout region is somewhat lower than that in the downcomer region, the depthwise velocity distribution of the fluid in the spout region may be

List of symbols at the end of the paper.

assumed to be fairly flat. It should, however, be pointed out that the effect of the particles on the void fraction of each fluid is taken into account at every step of the numerical integration. In addition, the effect of fluid drag forces acting on the particles is also considered. Since the depth (x-direction) of the bed is only 40 mm, and the fluid flow may be considered to be inviscid, it is convenient to carry out the fluid flow calculation in two dimensions (y,z) and save computational time and computer memory. Tsuji et al. [7,8] have shown that the fluid may be treated as inviscid except for

$$f_{pl} = \frac{\beta}{\rho_*} \left(\tilde{v}_{pl} - u_l \right) \tag{3}$$

the interaction term (f_{pi}) between the fluid and the particles.

where ε , u, p, ρ_g and $\bar{\nu}_{\mu}$ are the local void fraction, fluid velocity, pressure, fluid density and average particle velocity, respectively. The coefficient β is derived from Ergun's equation [15] for the dense phase and Wen and Yu's equation [16] for the dilute phase:

$$\beta = \begin{cases} \frac{\mu(1-\varepsilon)}{d_p^2 \varepsilon} [150(1-\varepsilon) + 1.75Re] & (\varepsilon \le 0.8) \\ \frac{3}{4} C_D \frac{\mu(1-\varepsilon)}{d_p^2} \varepsilon^{-2.7} Re & (\varepsilon > 0.8) \end{cases}$$
(4)

 $(Re \le 1000)$

$$C_D = \begin{cases} 24(1 + 0.15Re^{0.687})/Re \\ 0.43 \end{cases}$$

$$Re = \frac{\left| \bar{v}_p - u \right| \rho_g \varepsilon d_p}{\mu}$$



The particle motion is calculated by simultaneously applying Newton's law to each individual particle while taking into account the external gravity force (fg), the gas-solid drag forces (f_D) and the contact forces between the particles (fc). The particle motion is calculated three-dimensionally throughout the entire apparatus. The drag force is the sum of the reactionary forces in Eq. (3) and the pressure gradient as follows:

$$f_D = \left(\frac{\beta}{1 - \varepsilon} \left(u - v_p \right) - \frac{\partial p}{\partial x} \right) V_p \tag{7}$$

where V_p is the volume of a particle. The contact force is calculated by using the DEM correlation proposed by Cundall and Strack [17]. The contact force between a particle and the vessel wall, or draft plate, may be treated in a similar fashion as that between two particles but with the wall or draft plate always planar and stationary. An individual particle often comes into simultaneous contacts with several par-

http://www.cet-journal.de

ticles or a wall. Therefore, the contact force fc is the sum of all such forces. The Newton's equation of motion can be written as follows:

$$\ddot{x} = \frac{f_C + f_D}{m} + g \tag{8}$$

where m is the mass of a particle. The rotational motion of a particle caused by the tangential force is calculated from

$$\dot{\omega} = \frac{T}{I} \tag{9}$$

where T is the torque caused the tangential components of the contact forces and d is the moment of inertia of the particle.

3 Materials and Metho

3.1 Calculation Continuous

Tab. Compares the dimensions of the two system configturations the present simulation and the experiment of Kudra [1] and Kalwar [2]. Because of their importance, the dth of the gas inlet port and the particle diameter in both the experiment and the simulation are taken to be exactly same at 33 mm and 8 mm, respectively. Though the gemetry of the vessel is set as close as possible to the medi-

Table I. The properties of the particles and the dimensions of the vessels used in the DEM simulation and the experiments of [1] and [2].

	Simulation		Experiments (Kudra [1], Kalwar [2])		
Particle					
Diameter, d _p	(mm)	8.0	8.0		
Density, $ ho_p$	(kg/m^3)	1,231	1,231		
Sphericity, ϕ		1	0.755		
Vessel					
Width, W	(mm)	495	(11 × 45)	500	
Depth, Lb	(mm)	40	(8 × 5)	40	
Width of gas inlet, W_i	(mm)	33	(11×3)	33	
Width of draft plates, W.	(mm)	55	(11 × 5)	50	
Entrance height, He	(mm)	95	(19 × 5)	100	
Spout height, Hd	(mm)	912	(19 × 48)	900	
Normal distance,	(mm)	38.0	(19 × 2)	42.64	
Slant angle, θ	(degrees)	60	60		
Dimensionless sizes					
W/W _i		15	15.1		
W/d_p		61.8	62.5		
Wi/d _p		4.1	4.1		
Wd/W_I		1.6	1.5		

(6)

um-scale experimental apparatus of Kudra [1], it is not possible to avoid some slight differences while maintaining the same width of the gas inlet port and the same slant angle of the conic section at 60°. As shown in Fig. 1, the normal distance is the spacing between the draft plate and the slanting base. The particles are spherical and monodisperse. Their physical properties are based on shelled corn, whose properties are summarized in Tab. 1. The number of particles corresponding to the same bed height of 0.90 m as the experiments is approximately 26,000. The particle-particle friction coefficients (both static and kinetic) and the Poisson's ratio of the particles are 0.30 and 0.25, respectively. The coefficient of restitution of the particles is taken to be 0.90. The particle-wall friction coefficients (both static and kinetic) are taken to be 0.30. The vessel walls and draft plates are treated as stationary planar particles. The appropriate value of the spring constant at 800 N/m in the contact force model was determined in the same manner as Kawaguchi [8]. Air at 20 °C and 1 atm is used as the fluid. As mentioned in section 3.1, the gas flow is calculated two-dimensionally. The grid size for calculating the gas motion is $dy \times dz = 11 \text{ mm} \times 10^{-3}$ 19 mm. Since the DEM technique makes use of the locally averaged properties of the fluid flow in a computational fluid cell, the size of the computational fluid cell must never be smaller than the size of a single particle. In fact, to obtain statistically meaningful average values, the fluid call should be large enough to contain a small number of particles but much smaller than the entire flow region.

In addition, we have carried out the calculation of fluid flow in the absence of particles while halving all speeds of the grid. The obtained results show negligible differences in the flow field of both cases when compared a the same locations.

The maximum allowable time step for numerical integration is estimated using the oscillation period of the springmass system recommended by Tsuji et al. [7].

$$\Delta t \le \frac{\pi \sqrt{m/k}}{5} \tag{10}$$

where Δt and k are the integration time step and spring constant, respectively. The actual time step used is 0.0003 second. To determine the minimum spouting velocity, the superficial gas velocity is gradually reduced from a sufficiently large value. The superficial gas velocity is defined as the gas velocity over an empty cross section of the rectangular vessel. The calculation results will be verified against the experimental results of Kudra [1] and Kalwar [2].

Generally, a parabolic deflector is installed at the top of the 2DSB with draft plates in order to prevent the unintentional entrainment of particles and to enhance solids circulation by directing the particles from the spout back to the two downcomers. Kalwar [2] reported that the deflector above the draft plates is optimally installed centrally at a distance equal to 30% of the plate height. In the present simulation, no deflector is installed because the medium-scale experiment of Kudra [1] does not use one. Nevertheless, the possible effect of a deflector will be estimated and discussed.

3.2 Boundary Conditions for Fluid Motion

In DEM, the fluid motion based on locally averaged properties is calculated with the use of the finite-difference method and staggered grids. This requires that the size of the computational fluid cell must never be smaller than the size of a single particle. In fact, to obtain statistically meaningful average values, the fluid cell should be large enough to contain a small number of particles but much smaller than the entire flow region. Fig. 2 shows the numerical grids for fluid motion. The rectangular grids are employed in this calculation. The boundary condition used in the present calculation are summarized as follows:

(A) The gas is injected with the central hozzle.

$$u_y(22,0) = u_y(22,1)$$

$$u_y(23,0) = u_y(23,1)$$

$$u_z(22,0) = 15u_z/8(32.1)$$

$$u_z(23.0) = 15u i \epsilon(23.1)$$

$$u_{\nu}(24,0) = 15u_{\nu}(24,1)$$

(B) An outflow boundary is chosen at which the velocity practient becomes zero.

$$u_y(i,j_{max}+1) = u_y(i,j_{max})$$
 (for all i)

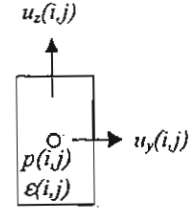
$$u_z(i,j_{max}+1) = u_z(i,j_{max})$$
 (for all i)

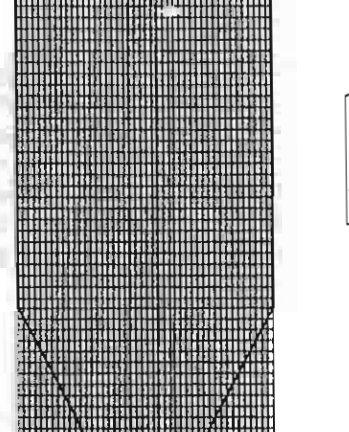
Since the fluid flow is assumed to be inviscid, the walls including the draft plates are treated as slip walls.

$$u_{y}(0,j) = 0 \qquad (for j \ge 22)$$

$$u_z(0,j) = u_z(1,j)$$
 (for $j \ge 22$)







$u_y(45,j)=0$	(for $j \ge 22$)
$u_z(46,j) = u_z(45,j)$	(for $j \ge 22$)
Slanted walls	
$u_y(21 - j,j) = 0$	$(\text{for } 1 \le j \le 21)$
$u_{\mathbf{z}}(21-j,j)=0$	(for $1 \le j \le 21$)
$u_y(24+j,j)=0$	(for $1 \le j \le 21$)
$u_z(24 + j,j) = 0$	$(\text{for } 1 \le j \le 21)$
Draft plates	
$u_{\gamma}(20\mathbf{J})=0$	$(\text{for } 5 \le j \le 48)$
$u_z(21,j) = u_z(20,j)$	$(\text{for } 5 \le j \le 48)$
$u_{y}(25,j)=0$	$(\text{for } 5 \le j \le 48)$
$u_z(26j) = u_z(25j)$	$(\text{for } 5 \le j \le 48)$

4 Results and Discussion

4.1 Minimum Spouting Velocity (ums) and Pressure Drop

Fig. 3 shows the calculated pressure drop vs. the inlet gas velocity. As shown in Fig. 2, the u_{ms} represents a turning point at which a slight reduction of the superficial gas velocity causes the spout to collapse and the pressure drop to significantly increase. Fig. 4 shows some snapshots of the flow patterns in the spouted bed with draft plates. In Fig. 4 the spout begins to collapse at the superficial gas velocity of 1.25 m/s. The minimum spouting velocity and corresponding pressure drop can be estimated from the correlations given by Kudra [1]. The correlation of u_{ms} is as follows:

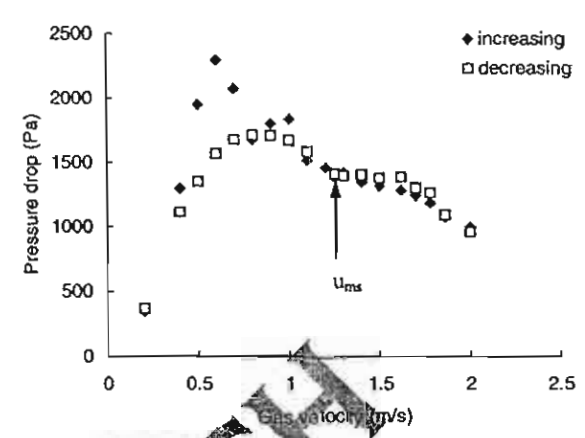
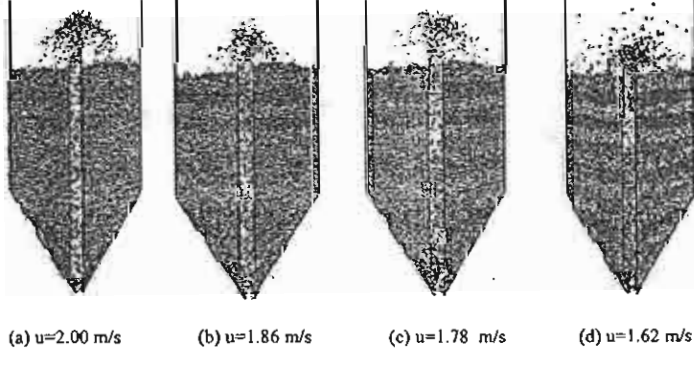


Figure 3. Calculated pressure drop vs. this inlet superficial gas velocity.

$$u_{ms} = \sqrt{g w_d} \rho^{0.084} \left(\frac{\rho_p - \rho_g}{\rho_g} \frac{H_e}{L_b} \right)^{0.15} \left(\frac{w_d d_p}{w_i H_b} \right)^{0.084} \tag{11}$$

For a culated minimum spouting velocity (u_{ms}) at the bed height of 0.9 m is 1.25 m/s while the prediction of Modra's correlation is 1.12 m/s. The apparent discrepancy in values may be ascribed to the slight differences in the vessel geometry. In the simulation H_e and W_d are 95 and 55 mm, respectively, whereas they are 100 and 50 mm in the experiment. Based on an experimental value of 1.12 m/s and Eq. (11), the predicted u_{ms} under the same vessel geometry





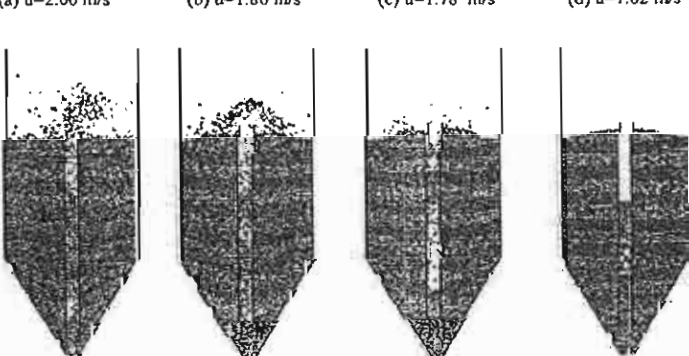


Figure 4. Snapshots of the flow patterns in the spouted bed with draft plates for different gas velocities.

(h) u=0.90 m/s

should be $(1.12)(55/50)^{0.5}(95/100)^{0.15}$ $(55/50)^{0.084} = 1.18$ m/s, which agrees very well with our simulation value of 1.25 m/s.

The correlation for the spouting pressure drop is as follows:

$$\Delta P_{ms} = \rho_b (gH_d)^{0.79} \theta^{0.33} \left(\frac{W_s}{w_b L_b \rho_b} \right)^{0.46} \left(\frac{s}{w_d} \right)^{0.42} \left(\frac{w_i H_b}{w_d H_d} \right)^{0.11}$$
(12)

As in the experiment of Kalwar [2], the pressure drop is measured between a central height of 11 mm above the bottom and the atmospheric pressure. The plotted pressure drop is time-smoothed over 1.8 seconds because slug flow causes the pressure to fluctuate strongly. Initially, the pressure drop increases as the superficial gas velocity increases. When the velocity reaches a certain value, the pressure drop starts to decrease gradually. Conversely, when the superficial gas velocity decreases from a sufficiently high value, the pressure drop gradually increases and then it increases significantly after passing the ums point. The hysteresis loop in the 2DSB occurs as shown in Fig. 3 because the flow resistance of the dense packed bed is higher than the loose one. In practice, the hysteresis loop will shrink somewhat the increase-decrease cycle is repeated by starting within loos rather than a relatively dense packed bed. However, the hysteresis cannot be eliminated entirely due to the inherent irreversibility of the jet penetration phenomenon [18]. The discrepancy between our calculated minimum spouling pressure drop and Kudra's prediction (1240 vs. 120 kPa, or 1.16:1) can be attributed to the above difference in the predicted and experimental u_{ms} (1.25 vs. 1.12 m/s, or (1.25/1.12)² =1.24:1). It is assumed here that the pressure drop is proportional to the square of the velocity.

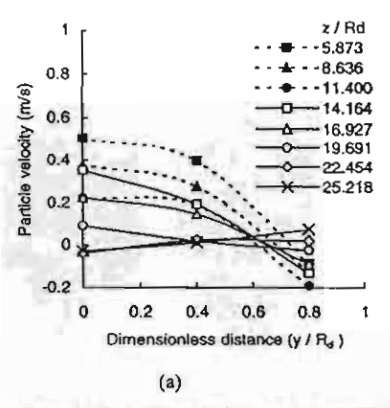
4.2 Particle Motion in the Spout Region

In this section, the spatial distribution of the particle velocity is investigated for each region: the spout and the downcomer. To save computer memory space, the particle velocities are recorded every 0.03 seconds. The particle velocities are time-smoothed over a period of 1.8 seconds corresponding to 60 snapshots. Fig. 5a) shows the profile of the timesmoothed vertical velocity of the particles and Fig. 5b) shows the timesmoothed void fraction at different heights in the spout region when the inlet superficial gas velocity is 1.25 m/s (= u_{ms}). In this figure, z/R_d is the dimensionless height. The dimensionless distance (y/R_d) is measured from the central axis of the spout. The draft plates are located at $y/R_d = \pm 1$. The dimensionless particle size is $(d_p/R_d) = 8/27.5 = 0.29$, and the dimensionless fluid cell size in the y-direction is $(dy/R_d) = 11/27.5 = 0.40$. To reduce randomness, the particle velocity shown in Fig. 5a) is obtained by averaging the velocities of the particles observed in a fluid cell. In the spout region, there are five fluid cells in the y-direction and their centers are used as the locations to show the time-smoothed particle velocity. The point $y/R_d = 0.8$ is the calculation point closest to the draft plate located at 1.0.

The particle vertical velocity in the spout decreases against the increased height because of slugging. The slugs formed in the upper region increases the flow resistance in the spout. The particle vertical velocities adjacent to the draft plates are lower than the local average value and some particles even fall flown. The height-averaged particle vertical velocity over the dimensionless height (z/R_d) 14.164-25.218 is shown in Fig. 6 for various inlet superficial gas velocities. Las found that the height-averaged particle verticalvelocities generally increase as the superficial gas velociy increases. In the present work, some slug flow occurs in the spout region at the minimum spouting velocity $(u_{ms} =$ 25 m/s). The slugs gradually disappear when the superficial gas velocity further increases as shown in Fig. 3. The foun-Ain is stable at $u_i > 1.5 u_{ms}$ ($u_i > 1.86 \text{ m/s}$). The observed formation of slugs in the simulation of the 2DSB, which is related to the waves of particles developed in the lower region of the spout [19], is consistent with reported experimental results. Formation of slugs is observed in the progressively incoherent spouting regime [20]. This regime occurs in the spouted bed when choking of the spout is the mechanism responsible for spout termination.

4.3 Particle Motion in the Downcomer Region

The profile of the particle vertical velocity in the downcomer region is shown in Fig. 7 for various heights. Here,



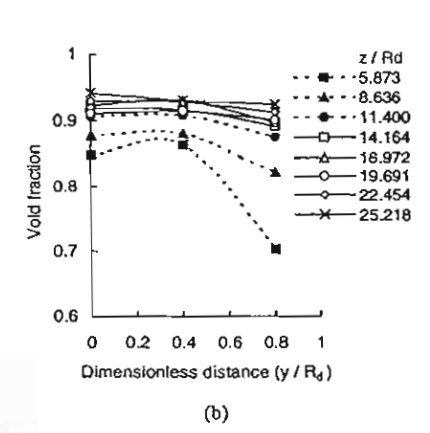


Figure 5. The profiles of (a) the particle vertical velocity and (b) the void fraction at different heights in the spout region when the inlet superficial gas velocity is 1.25 m/s (= u_{ms}).

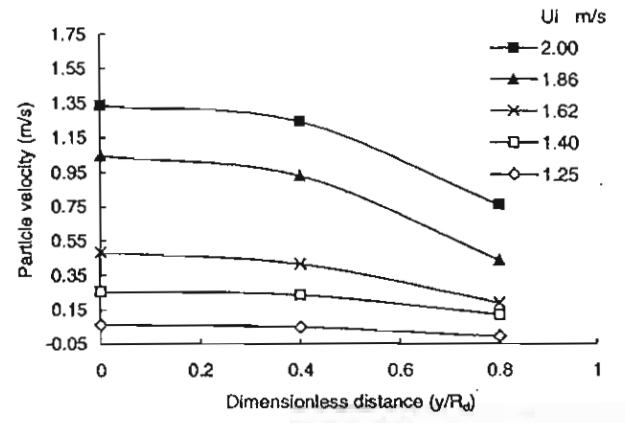


Figure 6. Profile of height-averaged vertical velocity of particles over the dimensionless height (z/R_d) 14.164–25.218 in the spout for various superficial gas velocities.

downward particle velocities are plotted as positive values. The draft plate is located at $y/R_d = 1$ and the wall, at $y/R_d = 1$ 9. As the height increases, the vertical particle velocities decrease in the vicinity of the draft plates whereas those near the vessel walls increase with the increasing height. Generally, the particle vertical velocities near the walls are lower than those near the draft plates because the increased fri tion between the particles and the slanting base defaints the return flow of the particles to the spout. In the lower region $(z/R_d = 5.873-11.400)$, the particle vertical relocations are higher than in the upper region (z/R 1416425.218) because of the reduction in the cross-sectional area by the slanting base. Fig. 8 shows the profile of the height-averaged particle vertical velocity over the dimensionless height (z/R_d) 14.164-25.218 in the downcomer at various inlet superficial gas velocities. As expected, the particle velocities increase with the increasing superficial gas velocity. At the same height, the reduction in the particle downward velocity near the walls and near the draft plates can be attributed to the friction between the particles and the stationary walls and draft plates.

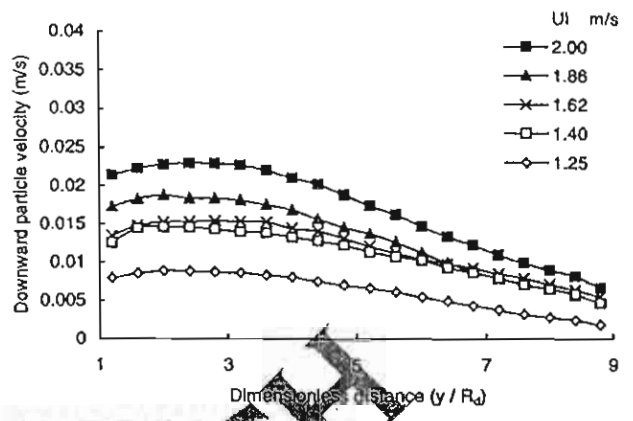
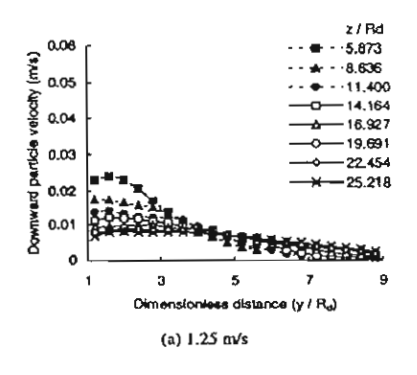


Figure 8. Profile of height veraged particle vertical velocity over the dimensionless height (z/R_d) 14.14–25.218 in the downcomer at various inlet superficial gas velocities.

4.4 Fluid Motion in the Spout and Downcomer Regions

The profile of the height-averaged vertical fluid velocity over the appensionless height (z/R_d) 14.164-25.218 in the pout region is shown in Fig. 9 for various inlet superficial velocities. The calculated terminal velocity of the particles is 15.76 m/s. The interstitial fluid velocity must be high mough to lift the particles in the spout. If the calculated interstitial fluid velocity is greater than 15.76 m/s, the particles will start to move upwards. In Fig. 9, the particles start to move upward at the minimum superficial gas velocity $u_{ms} =$ 1.25 m/s, which yields an interstitial velocity of 18.75 m/s at the vessel bottom. Fig. 10 shows the height-averaged vertical fluid velocity over the dimensionless heights (z/R_d) 14.164– 25.218 in the downcomer for various inlet superficial gas velocities. The spatial distribution of the height-averaged vertical fluid velocity is fairly uniform at all superficial gas velocities. The fluid velocities in the downcomer region generally decrease as the superficial gas velocity increases. This may be ascribed to the fact that slugs occurring in the spout at low superficial gas velocities cause the flow resistance in the



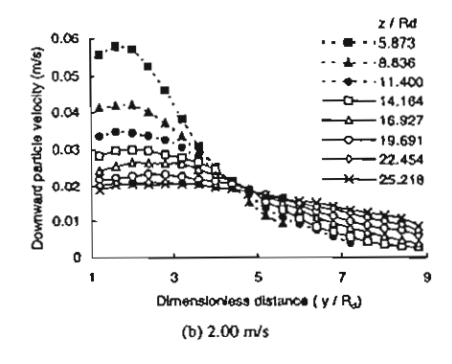


Figure 7. Particle vertical velocity profile in the downcomer for various dimensionless heights at superficial gas velocity (a) 1.25 m/s (u_{md}) and (b) 2.00 m/s $(1.6 u_{mg})$.

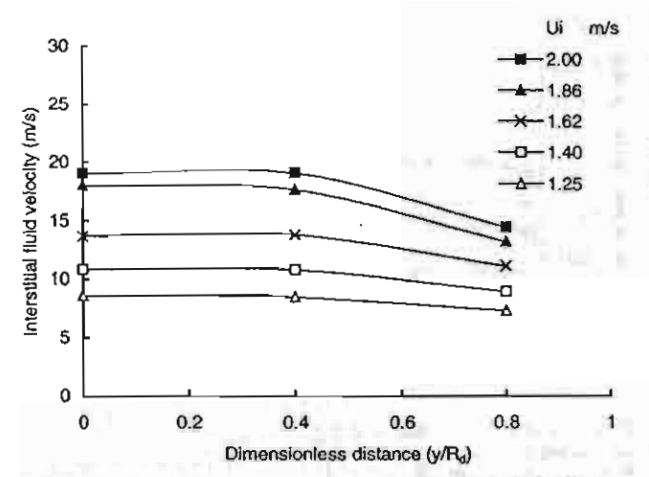


Figure 9. Profile of the height-averaged interstitial vertical fluid velocity profile over the dimensionless height (z/R_d) 14.164–25.218 in the spout region at various superficial gas velocities.

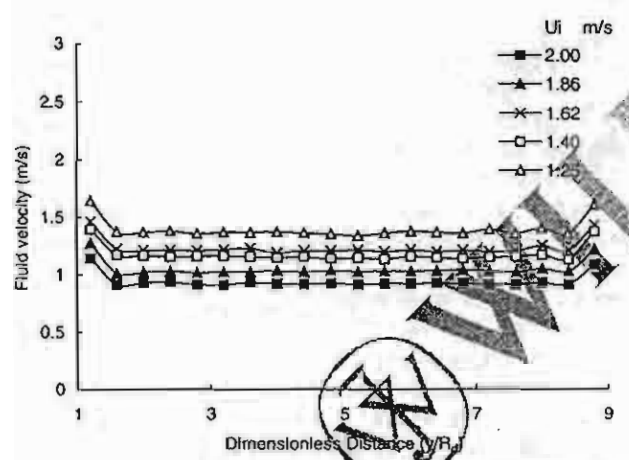


Figure 10. Profile of height-averaged vertical fluid-velocity over the dimensionless heights (z/R_d) 14.164-25.218 in the downcomer for various inlet superficial gas velocities.

spout region to increase. This in turn causes the gas flow into the downcomer to relatively increase, compared to the case of a higher superficial gas velocity. As shown in Fig. 10, the vertical fluid velocities near the draft plates and the walls are higher than elsewhere because the void fractions of the fluid cells close to them are slightly higher than elsewhere because of the channeling effect.

4.5 Circulation Rate of the Particles

The particle circulation rate can be estimated from the particle velocity above the slanting base, voidage, particle density and cross-sectional area of the downcomer as follows:

$$W_s = A_d v_\rho \rho_\rho (1 - \varepsilon) \tag{13}$$

where $W_{\mathbf{b}}$ $A_{\mathbf{b}}$ $v_{\mathbf{p}}$ $p_{\mathbf{p}}$ ε are the particle circulation rate, cross-sectional area of the downcomer, particle velocity above the slanting base, particle density and voidage, respectively. As expected, the particle circulation rate increases with the increasing gas flow rate. As reported by Law-Kwet-Cheong [21], a plot between the square root of the gas velocity and the particle circulation rate in Fig. 11 yields a straight line.

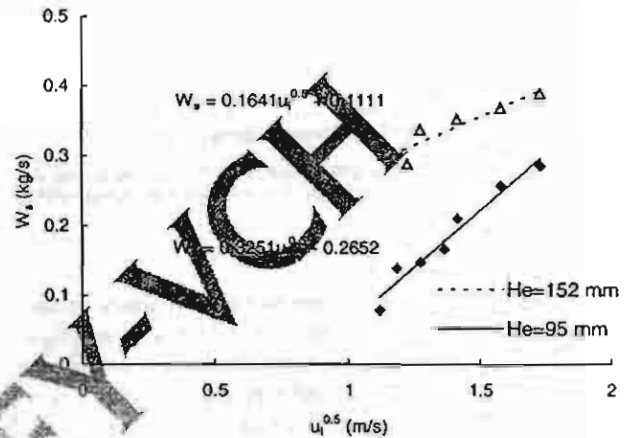


Figure 1 Relation between the particle circulation rate and the square root of superficial gas velocity ($H_e = 95.3 \text{ mm}$, $H_e = 152.48 \text{ mm}$).

4.5.1 Effect of Separation Height (H_e) on Particle Circulation Rate

As mentioned above, Fig. 11 shows an essentially linear relation between the particle circulation rate and the square root of the superficial gas velocity for two different separation heights, 95 and 152 mm. When the separation height increases from 95 mm to 152 mm, the normal distance in Fig. 1 increases from 37.97 mm to 66.47 mm, thus resulting in a larger number of particles entering the spout. The obtained empirical correlation for the particle circulation rate is as follows.

$$W_s = \begin{cases} 0.3251u_i^{0.5} - 0.2652, & for He = 95 \text{ mm} \\ 0.1641u_i^{0.5} + 0.1111, & for He = 152 \text{ mm} \end{cases}$$
 (14)

4.5.2 Effect of Coefficient of Friction on Particle Circulation Rate

The calculated particle circulation rate at 1.25 m/s (= u_{ms}) as a function of the friction coefficient is shown in Fig 12. As expected, the particle circulation rate decreases as the friction coefficient increases. An apparent friction coefficient of 0.063 gives a circulation rate consistent with the experimental value of 0.39 kg/s reported by Kalwar [2]. Fig. 12 reveals that the friction coefficient has a significant effect on the

(c) u=2.7 m/s

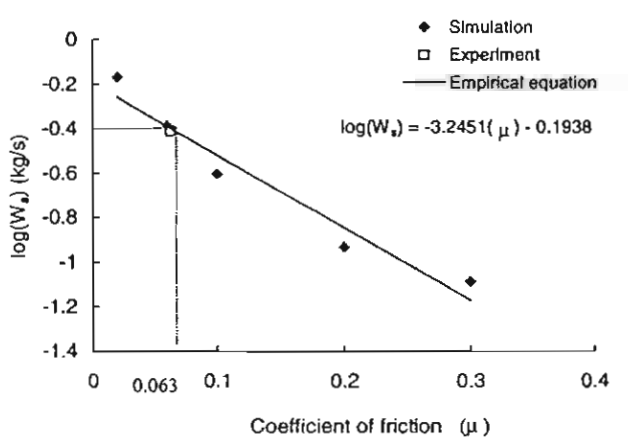


Figure 12. Calculated particle circulation rate at 1.25 m/s (= u_{so}) as a function of the friction coefficient.

particle circulation rate in the 2DSB with draft plates. The obtained empirical equation for the circulation rate is as follows:

$$\log(W_s) = -3.245(\mu) - 0.1938 \tag{15}$$

where μ is the friction coefficient. As for the effect of the bed height, the simulation results at u_{ms} show that the bed height does not significantly affect the particle circulation rate in the 2DSB with draft plates, which is consistent with Kalwar [2].

4.6 Effect of Draft Plates on the 2DSB

When the draft plates are removed from the vessel, our simulations show that spouting no longer occurs in the vessel with an initial bed height of 0.9 m (26,000 particles). A bubbling bed instead occurs in the vessel as shown in Fig. 13. Even as the gas velocity is further increased, the bubbling

bed still remains. The spouting does not occur in the vessel because the particle size is quite large. Malek and Lu [22] found that the maximum spoutable bed depth decreased as the particle size increased. Fig. 14 shows the observed flow patterns of the 2DSB at the bed height of 0.4 m (10,000 particles). Spouting does occur at this reduced bed height when the gas velocity is sufficiently high. The minimum spouting velocity and pressure drop are about 2.0 m/s and 1.75 kPa, respectively. As expected, the minimum spouting velocity and pressure drop of the 2DSB without plates are higher than those with

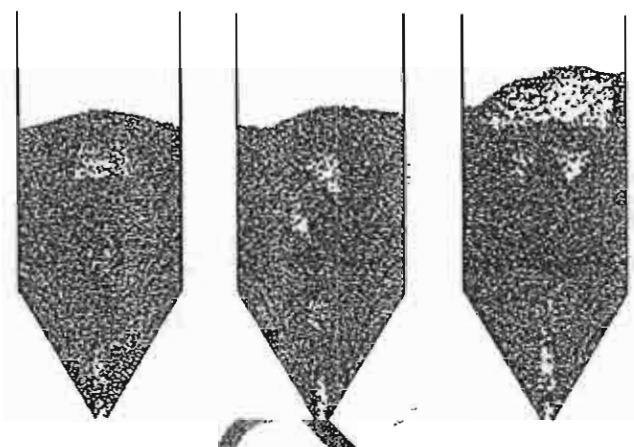


Figure 13. Flow patterns of 2DSBs the bed height of 0.9 m (26,000 particles).

(a) u=2.2 m/s

draft plates at confirms that the draft plates not only reduce the minimum spouting velocity and pressure drop but also increase the spoutable bed height.

47 Effect of an Overhead Deflector in the 2DSB with Draft Plates

Generally, an overhead deflector is installed in the 2DSB to prevent the unintentional entrainment of particles. On the negative side, an incorrectly installed deflector can induce breakage of particles. Kalwar [2] reported that the deflector was optimally placed above the draft plates at a distance equal to 30 % of the draft plate height (at 1.170 m). In the present work, we also investigate what would happen if an overhead deflector were centrally located above the draft plates at a distance equal to 10 %, 20 %, and 30 % of the draft plate height. Fig. 15 shows the calculated kinetic energy of the impacting particles time-smoothed over a peri-

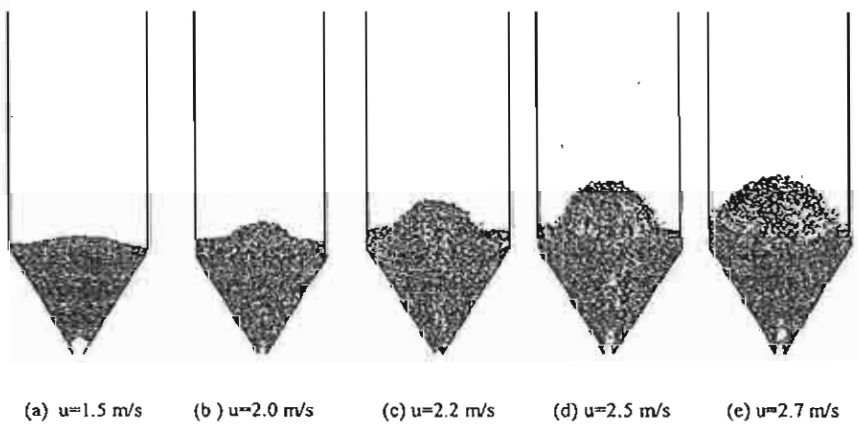


Figure 14. Flow patterns of the 2DSB at the bed height of 0.4 m (10,000 particles).

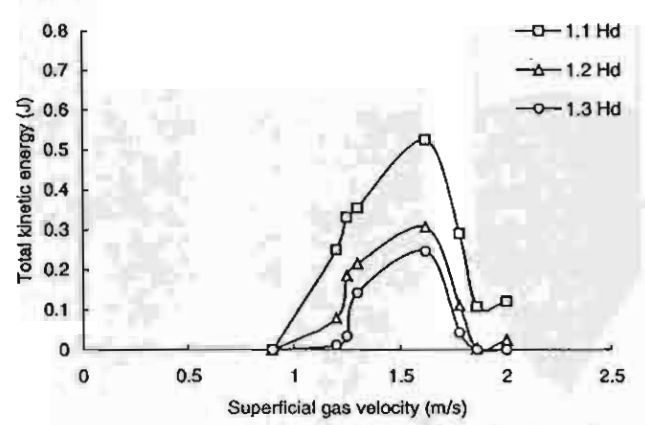


Figure 15. Calculated kinetic energy of the impacting particles time-smoothed over a period of 4.5 seconds as a function of the location of the deflector (H_d) and the superficial eas velocity.

od of 4.5 seconds as a function of the distance of the deflector and the superficial gas velocity. It is found that the kinetic energy upon impact decreases rapidly as the deflector height increases. The impacting kinetic energy at a superficial gas velocity of 1.62 m/s is highest because the slugs at this particular superficial velocity move with the highest average velocity. Beyond 1.62 m/s, the frequency of the slugs decreases and so does their average velocity as shown in Fig. 3. Our simulation results reveal that the impacting kinetic energy at a distance equal to 30% of the draft plate height is sufficiently low to prevent breakage. The average kinetic energy and average velocity of the particle that collide at the deflector are 2.13 · 10⁻⁴ J and 0.9 · m/s respectively. This is consistent with the finding of Kahyar [2].

5 Conclusions

The aerodynamics of particles and fluid flow in the two-dimensional spouted bed with draft plates has been investigated in detail with the aid of the DEM. The validity of the method has been confirmed with published experimental data of Kudra [1] and Kalwar [2]. Our results reveal that some slug flow still occurs in the spout at the minimum spouting velocity. This is the reason why the time-smoothed particle velocity decreases in the spout region as the height increases. The slugs gradually disappear when the gas velocity is further increased.

In the downcomer region, the particle vertical velocities near the draft plates are found to decrease as the height increases, but the velocities near the walls increase with the increasing height. The fluid velocities in the downcomer decrease as the superficial gas velocity increases while the particle circulation rate increases. As expected, the particle circulation rate decreases when the coefficient of friction increases. The calculated particle circulation rate is in good agreement with the experimental value of Kalwar [2] when the friction coefficient is sufficiently small at 0.063. When

the separation height increases, the particle circulation rate also increases. However, the bed height does not significantly affect the particle circulation rate at u_{ms} . The installation of the draft plates in the 2DSB not only reduces the minimum spouting velocity and pressure drop but also increases the maximum spoutable bed height. The impacting kinetic energy of the particles on an overhead deflector placed at a distance equal to 30 % of the draft plate height is sufficiently low to prevent breakage.

Acknowledgement

T. S. is grateful to Thailand Research Fund (TRF) for its Royal Golden Jubilee Ph.D. Scholarship and to Association of International Education Japan (AIEJ) for its 1-year student exchange fellowship to do research at Osaka University. W.T. and T. are grateful to TRF for financial support from it Team Research Promotion Fund. W. T., T. C., and T. T. are grateful to Chulalongkorn University (TJTTTP-JBIC Project), for supporting their short-term stays to carry out research collaboration between Osaka University and Chulalongkorn University.

Received: # [CET 1918]

ce-sectional area of downcomer

Symbols used

A_d	[m ⁻]	cross-sectional area of downcomer			
d_p	[m]	particle diameter			
g	$[m/s^2]$	gravity			
H_b	[m]	bed height			
H_d	[m]	spout height			
H.	[m]	entrance height or separation height			
L_b	[m]	bed length			
p	[Pa]	gas pressure			
R_d	[m]	distance from the spout central axis to			
		the draft plate			
S	[m]	slot width			
и	[m/s]	gas velocity of the ith direction in the coordinate			
u_i	[m/s]	superficial gas velocity at inlet gas			
Ums	[m/s]	minimum spouting velocity			
v_p	[m/s]	particle velocity above slanting base			
$\hat{\nu}_{pi}$	[m/s]	average particle velocity			
Vp	$[m^3]$	volume of a particle			
W	[m]	vessel width			
W_d	[m]	spout width			
W	[m]	width of gas inlet			
W_s	[kg/s]	mass flow rate of particle			
у	[m]	distance from the central spout axis in y-direction			
z	[m]	distance from the bottom of the vessel in z-direction			

Greek letters

3	[-]	void fraction
ρ_b	$[kg/m^3]$	bulk density, $\rho_b = \rho_p(1-\varepsilon)$
$\rho_{\rm g}$	[kg/m³]	gas density
ρ_{P}	$[kg/m^3]$	particle density
φ	[-]	sphericity
$\boldsymbol{\theta}$	[°]	slant angle
μ	[-]	friction coefficient

References

- T. Kudra, A. S. Mujumdar, G. S. V. Raghavan, M. I. Kalwar, Drying 92, 1992, 65, 83.
- M. I. Kalwar, Ph.D. Thesis, McGill University 1991,180.
- L.M. Passos, in Advances in Drying (Eds: L.M. Passos, A. S. Mujumdar, G. S. V. Raghavan), Hemisphere Publishing Corp., New York 1987, 359, 397.

- [4] A. S. Mujumdar, Drying'84, Hemisphere, New York 1984, 151, 157.
- [5] R. J. Rhodes, X. S. Wang, M. Nguyen, P. Stewart, K. Liffman, Chem. Eng. Sci. 2001, 56.
- Y. Tsuji, T. Tanaka, T. Ishida, Powder Technol. 1992, 71.
- Y. Tsuji, T. Kawaguchi, T. Tanaka, Powder Technol. 1993, 77.
 T. Kawaguchi, T. Tanaka, Y. Tsuji, Powder Technol. 1998, 96.
- [9] T. Kawaguchi, M. Sakamoto, T. Tanaka, Y. Tsuji, Powder Technol. 2000. 109.
- [10] Y. Kaneko, T. Shiojima, M. Horio, Chem. Eng. Sci. 1999, 54.
- [11] K. Kawagi, K. Takano, M. Horio, Powder Technol. 2000, 113.
- [12] D. Rong, M. Horio, In. J. Multiphase Flow 2001, 27.
- [13] K. Kuwagi, M. Horio, Chem. Eng. Sci. 2002, 57.
- [14] M. A. Van Nierop, G. Glover, A. L. Hinde, M. H. Moys, Int. J. Min. Process. 2001, 61.

- Process 2001, 61.

 [15] S. Ergun, Chem. Eng. Prog. 1952, 48(2).

 [16] C. Y. Wen, Y. H. Yu, Chem. Eng. Prog. Symp. 1966, 62.

 [17] P. A. Cundall, O. D. L. Strack, General India 1979, 29(1).

 [18] K. B. Mathur, N. Epstein, Spauled Beath Academic Press, Inc., London 1974, 304.

 [19] G. Volpicelli, G. Rast, L. Massimilla, Proc. Eindhoven Fluidization Symp., Nertherlands Press, Amsterdam 1967, 123.

 [20] N. Epstein, P. B. Chandnani, Chem. Eng. Sci. 1987, 42.

 [21] L. Law-Kwet-Chemal K. Malhotra, A. S. Mujumdar, Powder Technol. 1986, 46.
- 1986, 46.
- Y. Lu, Can. J. Chem. Eng. 1964, 42.



tion rate of activated carbon fibers for formaldehyde from 196.5 to 723.6 ml/g.

The adsorbent most widely used for removal of odoriferous substances is activated carbon. Generally, the starting materials for the production of activated carbons are those with high carbon but low inorganic contents, e.g. wood, lignite, peat and coal [4]. Nowadays, the attention is focused on the use of carbonaceous agricultural solid wastes due to their low cost [5]. In fact, a large number of these wastes, such as oil-palm stone [5], coconut shell [6], sugarcane bagasse [7], oil-palm shell [8], and peanut hulls [9] have been successfully converted into activated carbons by a physical activation process in laboratory tests. According to our knowledge, the research on producing the activated carbon from coffee residue has not been done. Coffee residue from coffee production process is an agricultural solid waste. Normally, coffee residue is disposed by landfill or burnout methods. In this work, the activated carbons from coffee residues were prepared by several activating conditions. We investigate the characterization of activated carbons including the capacity of formaldehyde adsorption.

2. Materials and methods

2.1. Materials

Coffee residues were kindly provided by Nestle Products (Thailand), Inc. Zinc chloride of purity 95% was obtained from UNILAB for chemical activation. Nitrogen and carbon dioxide gases were industrial grade from Thai Industrial Gas. Formaldehyde solution (38.0% w/w) was purchased from UNIVAR. The commercial activated carbon (CH-I1000) used to compare the formaldehyde adsorption capacity with coffee activated carbons was purchased from Carbokarn Company (Thailand). The original material of CH-I1000 is coconut shell and hard wood. The specific surface area and iodine number are 1050 m²/g and 1000, respectively. The particle size is under 325 mesh.

2.2. Activation conditions

Six types of activated carbons were prepared with different conditions as follows. Coffee residues were washed with water and dried at 110 °C for 24 h. The dried coffee residues were divided into two portions. One portion was added with ZnCl₂ in form of powder and some of water in ratio of ZnCl₂ to coffee residue 3:1. The mixture was dehydrated in an oven at 110 °C for 12 h. The other portion of coffee residues was left intact. Both portions of (40 g) coffee residues were treated with three procedures: (i) pyrolysis in a stainless steel tube held in a horizontal tube furnace (CARBOLITE) under nitrogen flow; (ii) pyrolysis under nitrogen flow followed with activation by carbon dioxide and (iii) pyrolysis under nitrogen flow followed with activation with steam. Heating rate of pyrolysis was 10 °C/min and the activation temperature was

kept constant at 600 °C for 4 h for all conditions. Then, the coffee activated carbons were cooled to room temperature. The ZnCl₂-impregnated activated carbons were washed with deionized water, 0.1 M HCl and hot deionized water sequentially to remove the residual zinc and chloride. Finally, the coffee activated carbons were dried in air at 110 °C for 12 h.

2.3. Physical characterization

Specific surface area and pore volume of the samples were determined by the nitrogen adsorption—desorption isotherms measured by Gas Sorption Analyzer (Quantachrome Corp., NOVA-1200). Prior to each measurement, carbon samples were outgassed at 300 °C under nitrogen flow for 12 h. The nitrogen adsorption—desorption data were recorded at liquid nitrogen temperature (77 K). The specific surface areas were calculated using BET equation [10]. In addition, the *t*-plot method was applied to calculate the micropore volume and mesopore surface area [10]. The total pore volumes were estimated to be the liquid volume of adsorbate (N₂) at a relative pressure of 0.98. All surface areas were calculated from the nitrogen adsorption isotherms by assuming the projected area of a nitrogen molecule to be 0.162 nm² [10].

2.4. Chemical characterization

The Fourier transform infrared spectroscopy (FTIR) is used to qualitatively identify the chemical functionality of activated carbons prepared from coffee residues. To obtain the observable adsorption spectra, the activated carbon was ground to the average diameter ca. 0.5 μ m. The transmission spectra of the samples were recorded using the KBr pallet containing 0.1% of carbon. The pallets 12.7 mm in diameter and ca. 1 mm thick were prepared in a manual hydraulic press at 10 tonnes and dried overnight at 100 °C before the spectra were recorded. The spectra were measured from 4000 to 400 cm⁻¹ and recorded on a BIO-RAD, FTS 175 spectrometer.

2.5. Thermogravimetric analysis (TGA)

Thermogravimetric experiments were carried out by a thermogravimetric analyzer (SHIMADZU, TGA-50) in order to determine the pyrolysis behaviour of coffee residue and ZnCl₂-impregnated coffee residue. Three samples: coffee residue, ZnCl₂ and ZnCl₂-impregnated coffee residue were subjected to measure in the temperature range of 30–800 °C at heating rate 10 °C/min under flowing of nitrogen gas flow and held at 800 °C for 10 min.

2.6. Proximate analysis

The proximate analysis was conducted according to ASTM D 3172-3175 standards [11] and the results were expressed in terms of moisture, volatile matter, ash and fixed carbon contents. One gram of sample was loaded in a crucible

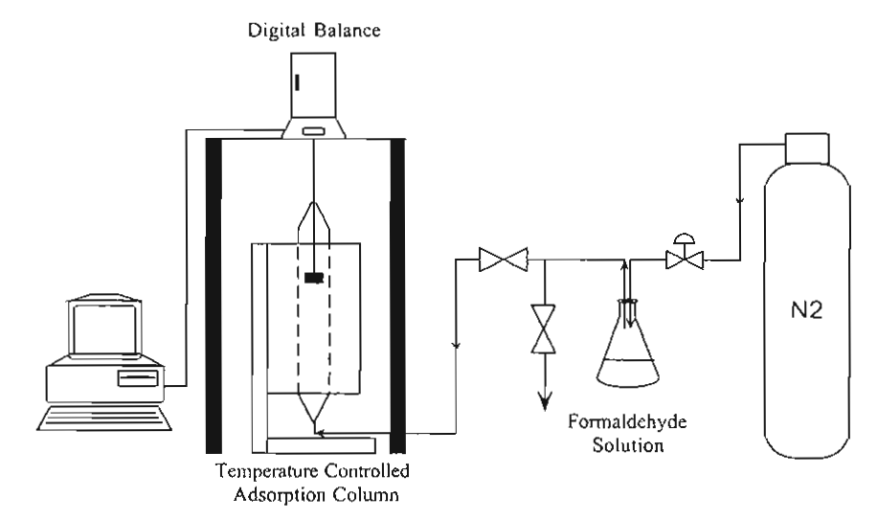


Fig. 1. The experimental apparatus for adsorption of formaldehyde.

with cover and heated from room temperature to 110°C in an oven until complete dehydration was accomplished. Then, the sample was decomposed in tube furnace at 950°C for 6 min to determine the quantity of volatile matters. The covered crucible was removed from the tube furnace and cooled to room temperature in a desiccator. To determine the ash content, approximately I g of sample was placed in covered crucible and heated with the flame for 10 min followed with heating in the muffle furnace from room temperature to 750°C for 3 h. Then, the crucible was placed in a desiccator and allowed to cool at room temperature. The fixed carbon content was obtained by subtracting moisture, volatile matter and ash content from 100%.

2.7. Adsorption of formaldehyde vapor

The derived activated carbons and CH-I1000 were used to adsorb formaldehyde vapor in the experimental apparatus depicted in Fig. 1. This consists of three main parts: (i) vaporizer for the generation of formaldehyde vapor; (ii) adsorption column for sample loading with a stainless mesh basket hung from a digital balance (Sartorius, CP224S) and (iii) a digital balance connected with computer for data acquisition.

The formaldehyde vapor was generated by flowing nitrogen gas at the flow rate 115 ml/min through the formaldehyde solution to the adsorption column. The concentrations of formaldehyde solution used in the experiment were 10, 20, 30 and 38% (w/w) which generated the formaldehyde vapor at the concentration 13767, 30431, 50899 and 74216 ppm, respectively. The average weight of sample loaded in the basket was around 0.1 g. The column temperature was maintained at 30 °C throughout the experiment. Weight change of the sample due to the adsorption was recorded on the computer. The experiment was carried out until adsorption reached equilibrium

3. Results and discussion

3.1. Nitrogen isotherm, specific surface area and pore valume

Table 1 lists the sample identification and production yield of each activated carbon. For example, sample prepared with ZnCl2 under nitrogen flow is named CZn-N2. Fig. 2 shows the N₂ adsorption-desorption isotherms of six types of coffee activated carbon and commercial activated carbon, CH-11000. The amount of N2 adsorbed was plotted against the relative pressure, P/P_0 of N_2 where P is vapor pressure and P_0 is saturated vapor pressure. We found that the N2 isotherms of CZn-N2-CO2, CZn-N2, CN2-ST, CZn-N2-ST and CN2 exhibited type IV isotherms according to IUPAC classification [12] with a hysteresis loop which associated with physical adsorption of gases by mesoporous solids. The lower branch of isotherm (solid line) represents measurements obtained by progressive adsorption of nitrogen gas on the adsorbent and the upper branch (dotted line) by progressive desorption [13]. Meanwhile, the isotherm of CN2-CO2 exhibited type II isotherms, which describe physical adsorption of gases by non-porous solids. Lastly, the N2 isotherms of the commercial activated carbon (CH-I1000) exhibited type I isotherms, which are typical of microporous solids. The micropore filling occurs significantly at relatively low partial

Table 1 Sample identification for activation conditions and production yield

			T-T-		
Sample identification	ZnCl ₂ impregnation	Pyrolysis iπ N ₂	CO ₂ activation	Steam activation	Yield (%)
CN ₂	No	Yes	No	No	22.20
CN_2 — CO_2	No	Yes	Yes	No	21.67
CN ₂ -ST	No	Yes	No	Yes	13.33
$CZn-N_2$	Yes	Yes	No	No	44.33
CZn-N2-CO2	Yes	Yes	Yes	No	32.60
$CZn-N_2-ST$	Yes	Yes	No	Yes	80.30

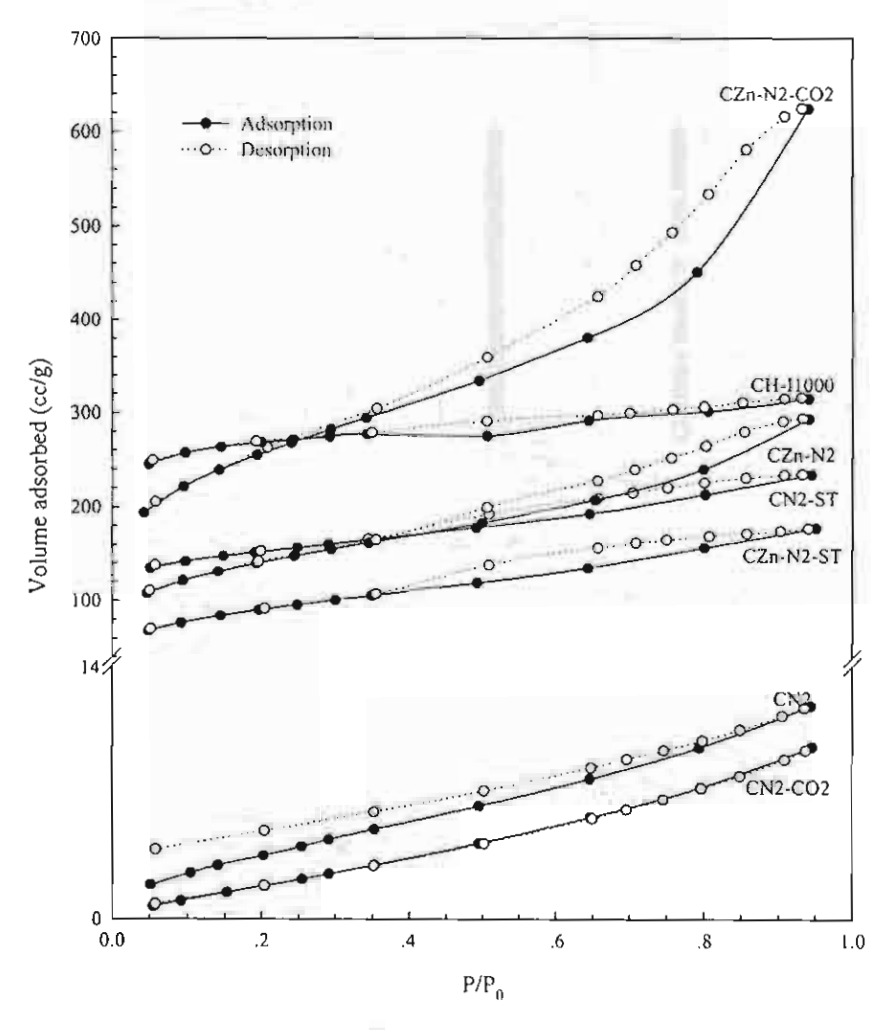


Fig. 2. Nitrogen adsorption-desorption isotherms of tested activated carbons.

pressures <0.1 P/P_0 , the adsorption process being completed at 0.5 P/P_0 [12].

Total surface area, mesopore surface area, total pore volume and micropore volume are tabulated in Table 2. It is noticed that the specific surface areas and pore volumes of carbons activated by ZnCl₂ were higher than that of none ZnCl₂. ZnCl₂ is a dehydrating agent which may alter the pyrolysis behavior of carbonaceous materials. After mixing with carbon materials, ZnCl₂ can be intercalated in the carbon matrix. Upon pyrolysis, a severe interaction between zinc compounds

and the carbon atoms occurred. Hence, atomic layers of carbon may be widened and pores were formed in the carbon matrix. During pyrolysis, ZnCl₂ caused hydrogen and oxygen atoms to be removed from the source materials as water rather than as hydrocarbons or as oxygenated organic compounds [14]. Therefore, more pores were created. The sample activated by ZnCl₂ and carbon dioxide (CZn-N₂-CO₂) yielded the highest specific surface areas and pore volumes. This may be attributed to an amount of ZnCl₂ released from carbon due to the presence of carbon dioxide, so pores were

Table 2
Specific surface area, pore volume and average diameter of tested activated carbons

Sample identification	V _T (cc/g)	V _{mi} (cc/g)	S_{T} (m^{2}/g)	$S_{\rm me}~({\rm m}^2/{\rm g})$	D (Å)
CN ₂	0.018 ± 0.003	0.000 ± 0.002	16 ± 1	14 ± 2	47.01 ± 0.05
CN2-CO2	0.015 ± 0.005	0.000 : 0.004	11 ± 2	11 ± 2	54.26 ± 0.03
CN2-ST	0.362 ± 0.002	0.170 sir 0.003	469 ± 14	136 ±12	30.88 ± 0.02
CZn-N ₂	0.454 ± 0.003	0.090 ± 0.002	470 ± 12	254 ± 15	38.66 ± 0.03
CZn-N2-CO2	1.010 ± 0.003	0.084 ± 0.003	914 ± 21	629 ± 24	44.24 \$ 0.02
CZn-N ₂ -ST	0.275 ± 0.004	0.073 ± 0.003	305 ± 25	139 ± 21	36.02 10.04
CH-11000	0.488 ± 0.002	0.367 ± 0.003	790 ± 11	87 ± 13	24.70 4 0.03

 V_T , total volume; V_{mi} , micropore volume; S_T , total surface area, S_{mc} , mesopore surface area; D_c average diameter.

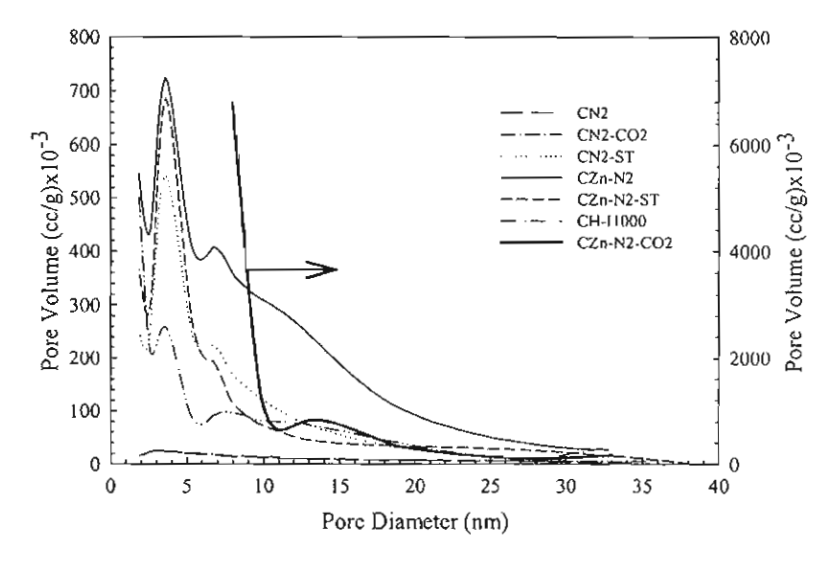


Fig. 3. Pore size distributions of tested activated carbons.

opened during activation with carbon dioxide. Thus, the carbon on the pore-wall was exposed in carbon dioxide and oxidized by carbon dioxide, resulting in an enlargement of the pores [14]. The physicochemical activation used ZnCl₂ and steam (CZn-N₂-ST) did not produce the high-surface area activated carbon as same as that of ZnCl₂ and CO₂. Steam may cause ZnCl₂ melt into liquid and cannot be intercalated in the carbon matrix. Consequently, ZnCl₂ could not react effectively to enlarge pore size.

The adsorption of N_2 on CN_2 and CN_2 — CO_2 was much lower (around 20–100 times) than those of the others because of low specific surface areas and pore volumes as appeared in Table 2. This may be ascribed to CN_2 possessed only the rudimentary pores produced during pyrolysis in N_2 . It was not activated by any activating agent. In the case of CN_2 — CO_2 , the activation process occurred at low temperature (600 °C) so that high-surface area or pore volume could not be expected. Normally, the physical activation should be conducted in the temperature range of 800–1000 °C [14].

3.2. Pore size distribution

Pore size distributions of the coffee activated carbons and CH-I1000 are shown in Fig. 3. The peaks of the pore volume for each sample occur at 2.9 nm for CN₂ and CN₂-CO₂, 3.5 nm for CN₂-ST, 3.7 nm for CZn-N₂ and CZn-N₂-ST, 8.0 nm for CZn-N₂-CO₂ and 2.2 nm for CH-I1000. This provided the evidence that the derived activated carbons yielded a great deal of large pores, indicating these activated carbons are mesoporous materials. The pore diameter of the sample CZn-N₂-CO₂ is the largest. The pore size distributions of all the samples except CZn-N₂ are narrow and smaller than 10 nm. Narrow pore size distribution should be very advantageous for some applications, such as separation [14].

3.3. Thermogravimetric analysis (TGA) and proximate analysis

Fig. 4 shows the weight loss (TG) and derivative thermogravity (dTG) curves of three samples: coffee residue, ZnCl₂ and ZnCl₂-impregnated coffee residue at ratio of ZnCl₂ to coffee residue 3:1 by weight in N₂ atmosphere and at a 10 °C/min heating rate. Fig. 4a shows the thermal decomposition behavior of coffee residue: the first range from 50 to 257 °C presents a little weight loss due to the moisture release, the next range from 257 to 470 °C presents a significant weight loss due to the volatiles release and we can observe that there are two peaks of dTG curve in this range, the last range from 470 to 800 °C.

Fig. 4b shows TG and dTG curves of pure ZnCl₂. A plateau at temperature below 400 °C is the weight loss due to release of moisture. In the temperature range of 400–590 °C, weight loss of ZnCl₂ is significant, particularly at temperature around 570 °C as shown by a sharp dTG peak.

Fig. 4c shows TG and dTG results of coffee residue impregnated with ZnCl2. The weight loss from initial up to 400 °C was gradual and different from that in Fig. 4a. Since ZnCl₂ undergoes little weight loss at these temperatures, the observed weight loss was only for coffee residue weight. This loss of weight is lower than that obtained by untreated coffee residue. Thus, the presence of ZnCl₂ has a significant effect on the pyrolysis behavior of coffee residue. The weight loss from 400 to 590 °C should be due to the release of ZnCl2 including a few volatiles. The sample with ZnCl₂ impregnation yielded 40% of residue, which was higher than that (ca. 15%) obtained for the raw coffee residue (It has to be recognized that ZnCl₂ constituted 75% of total weight of this sample. Then, the yield should be calculated on the basis of 25% coffee residue in the sample.). The significant effect of ZnCl2 suggested that the consequential decrease in the evolution of volatiles would increase the yield. As seen in Table 1 that per-

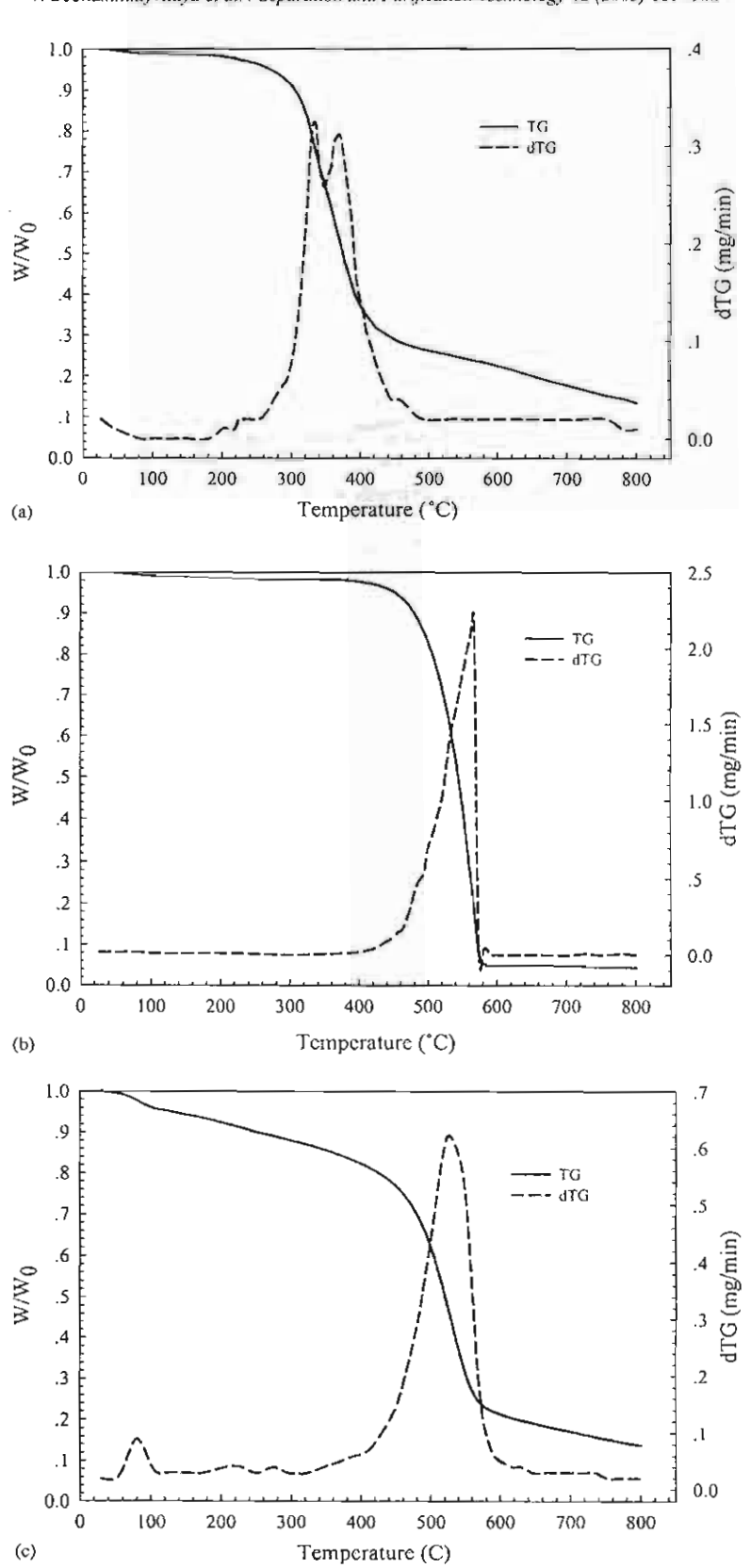


Fig. 4. TGA and dTG curves of: (a) coffee residue; (b) ZnCl₂ and (c) ZnCl₂-impregnated coffee residue at ratio of ZnCl₂ to coffee residue 3:1.

Table 3
Proximate analysis of coffee residue and selected activated carbons

Sample	Moisture (wt.%)	VM (wt.%)	Ash (wt.%)	FC (wt.%)
Coffee residue	4.29 ± 0.04	82.81 ± 0.02	3.92 ± 0.02	13.27 ± 0.02
CZn-N ₂	12.64 ± 0.02	37.38 ± 0.03	11.49 ± 0.02	38.49 ± 0.02
CZn-N2-CO2	5.36 ± 0.03	26.04 ± 0.03	10.46 ± 0.04	58.14 ± 0.03
CZn-N2-ST	7.70 ± 0.02	26.87 ± 0.02	5.15 ± 0.03	60.28 ± 0.02

VM, volatile matter; FC, fixed carbon,

cent yield of the sample prepared with ZnCl₂ impregnation is higher than that of the sample without ZnCl₂ impregnation.

In addition, the results of proximate analysis of coffee residue and coffee activated carbons are shown in Table 3. The raw coffee residue consisted high in volatile matter content and low in fixed carbon and ash content. After activation, the percent fixed carbon of coffee activated carbon increased and percent volatile matter decreased.

3.4. Chemical characterization

FTIR spectra of two groups with and without ZnCl₂-impregnated coffee activated carbons including the commercial one are shown in Fig. 5. Band assignments for Fig. 5 are summarized in Table 4. In Fig. 5a, a strong and broad O-H peak, hydrophilic group, is displayed on the spectrum of CZn-N₂ at 3333 cm⁻¹ and the weaker one is observed on the CZn-N₂-ST spectrum at 3212 cm⁻¹ while it is not observed on CZn-N₂-CO₂. On the contrary, the spectrum

Table 4
FTIR spectrum band assignments [15]

Band number (cm ⁻¹)	Assignment
3594	O-H stretching vibration in free O-H
3333, 3320	O-H stretching vibration in hydrogen bonds
3212	O-H stretching vibration in phenol
2834, 2882, 2884, 2974, 2981	C-H stretching vibration in methyl group
2823, 2886, 2889	C-H stretching vibration in methylene group
2756	C-H stretching vibration in aromatic
2699	C-H stretching vibration in aldehyde
2132, 2174	C≡C stretching vibration in alkyne
1612, 1631, 1656, 1657. 1695, 1732	C=O stretching vibration in ketone
1559, 1570, 1585	C=C stretching vibration in aromatic
1467	C-H deformation vibration in methylene group
1439	C-H deformation vibration in -C(CH ₃) ₃
1418	C-H deformation vibration in alkane
1161, 1206, 1218	C-O stretching vibration in alcohol

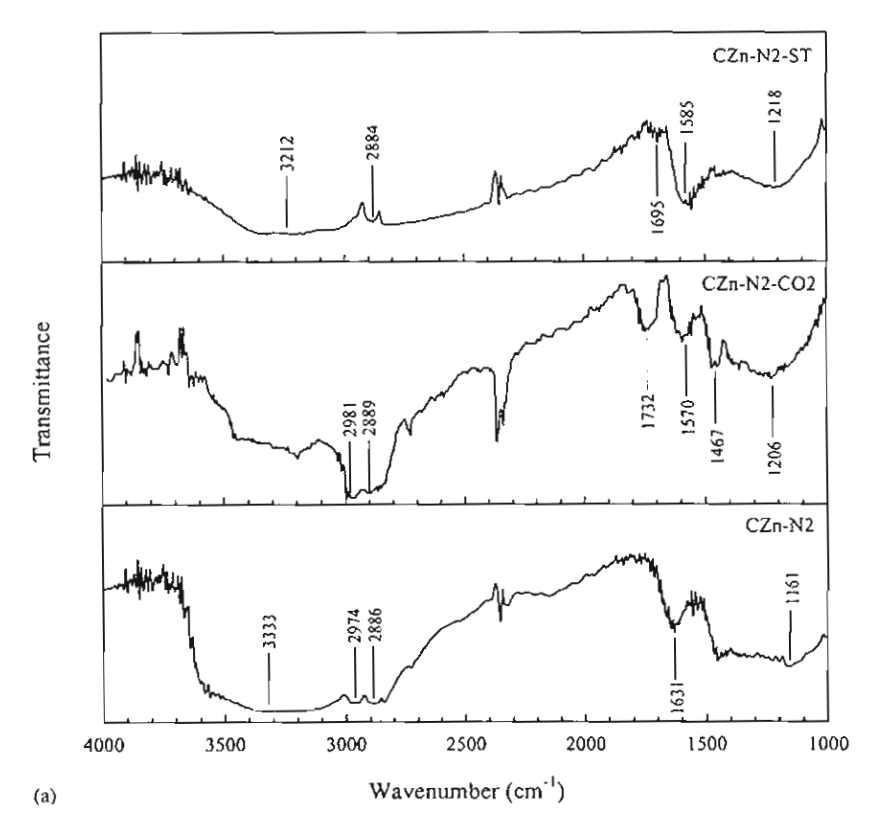


Fig. 5. FTIR spectra of coffee activated carbon with (a) and without (b) ZnCl2-impregnated treatment and (c) CH-11000.

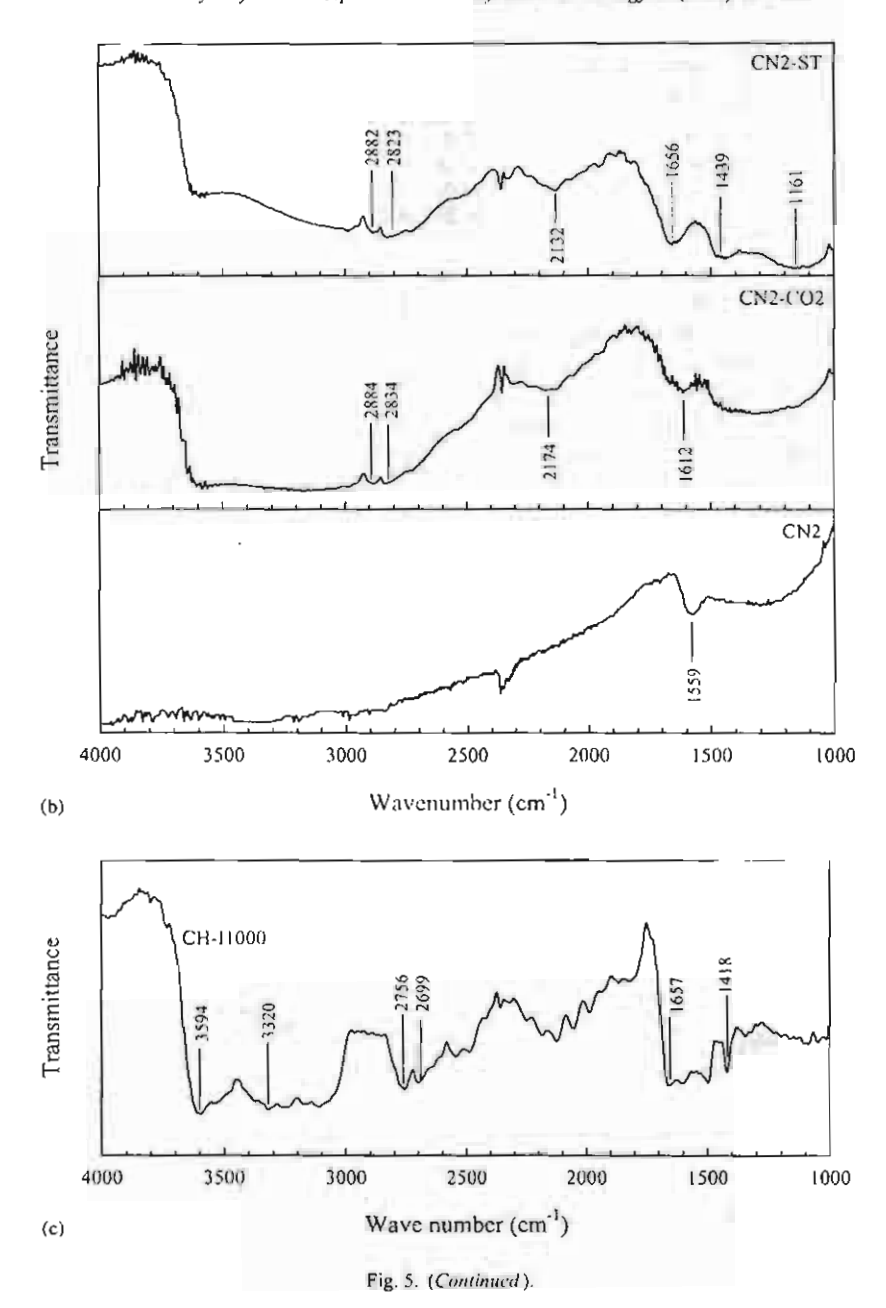


Table 5 Activated carbon listed in the order of formaldehyde adsorption capacity Functional groups Order Sample Pore texture characteristics Total surface area (m2/g) Hydrophilic Hydrophobic Total pore volume (cc/g) 1. CZn-N₂ O-H (strong), C=O, C-O C-H (weak) 470 ± 12 0.454 ± 0.003 2. 3. CH-I1000 O-H, C=O C-H 790 ± 11 0.488 ± 0.002 CZ_n-N_2-ST $CZ_n-N_2-CO_2$ O-H (weak), C=O, C-O C~H 305 ± 25 0.275 ± 0.004 914 ± 21 4. C=0, C-0 C-H (strong), C=C 1.010 ± 0.003 5. CN₂-ST C=0, C-0 С−Н, С≡С 469 ± 14 0.362 ± 0.002 CN2-CO2 C=O C-H, C≡C 11 ± 2 0.015 ± 0.005 CN₂ C=C 16 ± 1 0.018 ± 0.003

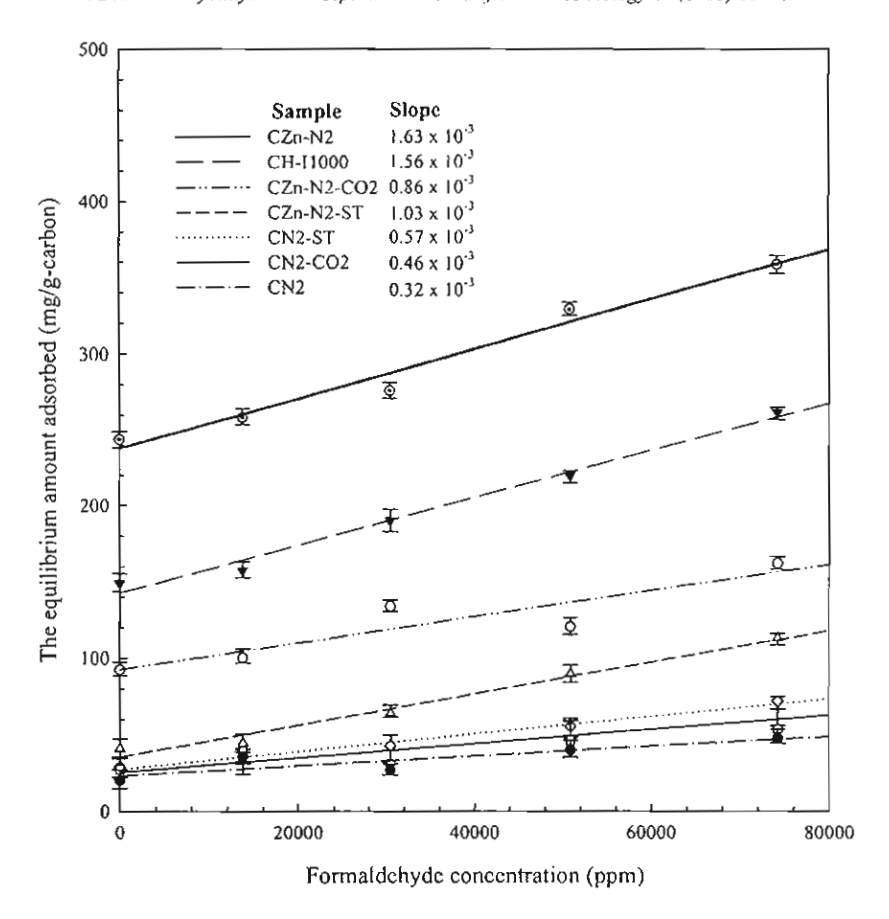


Fig. 6. The equilibrium amount adsorbed by tested activated carbons at various concentrations and temperature of 30 °C.

of CZn-N₂-CO₂ shows the strongest peak of hydrophobic group, C-H, at 2981, 2889 and 1467 cm⁻¹. In addition, another hydrophobic group, C=C, is also located on the spectrum of CZn-N₂-CO₂.

Fig. 5b shows the spectra of coffee activated carbon without $ZnCl_2$ impregnation. There are two hydrophilic groups, C=O and C=O, which display at band 1656 and 1161 cm⁻¹, respectively, on the spectrum of CN_2 -ST while only one hydrophilic group, C=O, at 1612 cm⁻¹ on CN_2 -CO₂ spectrum. There is no hydrophilic group on the spectrum of CN_2 .

The FTIR spectrum of CH-I1000, commercial activated carbon, is shown in Fig. 5c. The main hydrophilic groups detected on the spectrum are O-H at 3594 and 3320 cm⁻¹ and C=O at 1657 cm⁻¹.

3.5. Adsorption of formaldehyde vapor

Fig. 6 shows the equilibrium amount of formaldehyde and water vapor adsorbed onto each type of coffee activated carbons and one commercial activated carbon CH-I1000 at various formaldehyde concentrations. In the experiments where the concentration of formaldehyde is zero, the amount adsorbed by CZn-N₂ is highest among all around 245 mg/g-carbon. This implies that CZn-N₂ can adsorb water superior to the others. This may be ascribed to ZnO contained

in CZn-N₂ since the ash content of CZn-N₂ as shown in Table 3 is 11.49 ± 0.02 wt.%, the highest among all.

Though we cannot quantitatively evaluate the amount of formaldehyde adsorbed on each activated carbon, the slope of graphs in Fig. 6 demonstrates the adsorption capacity of each adsorbent. The order of formaldehyde adsorption capacity is in the following order: CZn-N₂ > CH-I1000 > $CZn-N_2-ST > CZn-N_2-CO_2 > CN_2-ST > CN_2-CO_2 >$ CN2. The adsorption capacity can be affected by both of pore texture characteristics and surface chemistry of activated carbon. The order of the activated carbon with functional groups and pore texture characteristics is summarized in Table 5. It should be noticed that the order of adsorption capacity is significantly influenced by the functional groups of O-H, C=O and C-O contained in CZn-N2, CH-I1000 and CZn-N2-ST. In particular, CZn-N2, which has the strongest peak of O-H group, demonstrates the highest adsorption capacity.

The influence of surface chemistry on adsorption capacity is clearly observed in case of $CZn-N_2-CO_2$. The formaldehyde adsorption should be high since $CZn-N_2-CO_2$ has the highest surface area (914 \pm 21 m²/g) and pore volume (1.010 \pm 0.003 cc/g). However, the adsorption is just about 130 mg/g-carbon (at formaldehyde concentration of 74216 ppm). We considered that hydrophobic groups of

C-H and C=C on the surface of CZn-N₂-CO₂ affected the adsorption.

In the case of CN₂-ST, its total surface area is very closed to CZn-N₂ but the surface of CZn-N₂ is more hydrophilic than that of CN₂-ST. Thus, the adsorption capacity of CN₂-ST is inferior to CZn-N₂. The last two activated carbons CN₂-CO₂ and CN₂ in Table 5 contain less hydrophilic groups and yield low total surface area and pore volume so their adsorption capacities are low.

The commercial activated carbon, CH-I1000 shows good capacity in formaldehyde adsorption owing to its hydrophilic groups and quite large surface.

4. Conclusions

The coffee activated carbons were derived by the variation of activation conditions. These activated carbons were characterized by nitrogen adsorption-desorption isotherm, TGA, FTIR and used to adsorb formaldehyde vapor. The activated carbon prepared by ZnCl2 and nitrogen activation, CZn-N2, exhibited the highest adsorption capacity owing to the hydrophilic functional groups of O-H, C=O, C-O detected on the surface. The coffee activated carbon prepared with ZnCl2 impregnation coupled with carbon dioxide activation (CZn-N2-CO2) yields the highest total surface area $(914 \pm 21 \text{ m}^2/\text{g})$ and total pore volume $(1.010 \pm 0.003 \text{ cc/g})$ but adsorbs formaldehyde less than CZn-N2. We found that CZn-N₂-CO₂ contains hydrophobic groups of C-H, C=C from FTIR results. Therefore the surface chemistry of activated carbon affects the adsorption capacity significantly while the texture characteristics of surface area and pore volume play a minor role in formaldehyde adsorption.

Acknowledgements

This research is financially supported from the Joint Graduate School of Energy and Environment (JGSEE), the Thailand Research Fund (TRFRTA of Dr. Wiwut Tanthapanichakoon 2002-2005) and from University Linkage Grant, Chulalongkorn University. The author would like to acknowledge Nestle Products (Thailand), Inc. for providing the raw coffee residues and Department of Chemical Engineering, Faculty of Engineering, Burapa University for facilitating Gas Sorption Analyzer equipment.

References

- [1] H. Rong, Z. Ryu, J. Zheng, Y. Zhang, Carbon 40 (2002) 2291.
- [2] N. Brais, United States Patent, 5,833,740, 1998.
- [3] H. Rong, Z. Ryu, J. Zheng, Y. Zhang, J. Colloid Interface Sci. 261 (2003) 207.
- [4] R.C. Bansal, J.B. Donnet, F. Stoeckli, Active Carbon, Marcel Dekker, New York, 1988 (Chapter 1).
- [5] A.C. Lua, J. Guo, Colloids Surf. A: Physicochem. Eng. Aspects 179 (2001) 151.
- [6] Z. Hu, M.P. Srinivasan, Microporous Mesoporous Mater. 27 (1999)
- [7] W.T. Tsai, C.Y. Chang, M.C. Lin, S.F. Chien, H.F. Sun, M.F. Hsieh, Chemosphere 45 (2001) 51.
- [8] A.C. Lua, J. Guo, Langmuir 17 (2001) 7112.
- [9] B.S. Girgis, S.S. Yunis, A.M. Soliman, Mater. Lett. 57 (2002) 164.
- [10] S.J. Gregg, K.S.W. Sing, Adsorption Surface Area and Porosity, 2nd ed., Academic Press, London, 1982 (Chapters 2 and 6).
- [11] ASTM D 3172-3175, Annual Book of ASTM Standards, Section 5 Petroleum Products, Lubricants, and Fossil Fuels, Volume 05.05 Gaseous Fuels, Coal and Coke, 1999.
- [12] J.W. Patrick, Porosity in Carbons: Characterization and Applications, Edward Arnold, Great Britain, 1995 (Chapter 1).
- [13] F.O. Rouquerol, J. Rouquerol, K.S.W. Sing, Adsorption by Powders & Porous Solids: Principles Methodology and Applications, Academic Press, San Diego, 1999 (Chapter 1).
- [14] Z. Hu, M.P. Srinivasan, Y. Ni, Carbon 39 (2001) 877.
- [15] G. Socrates, Infrared and Raman Characteristic Group Frequencies: Tables and Charts, 3rd ed., John Wiley & Sons Ltd., West Sussex, 2001.



Water Research 39 (2005) 1347-1353



Adsorption-desorption characteristics of phenol and reactive dyes from aqueous solution on mesoporous activated carbon prepared from waste tires

W. Tanthapanichakoon^{a,*}, P. Ariyadejwanich^b, P. Japthong^b, K. Nakagawa^c, S.R. Mukai^c, H. Tamon^c

^aNational Nanotechnology Center, Thailand Science Park, 111 Paholyothin Road, Klony Luang, Pathumthani 12120, Thailand

^bDepartment of Chemical Engineering, Chidalongkorn University, Bangkok 10330, Thailand

^cDepartment of Chemical Engineering, Kyoto University, Katsura, Kyoto 615-8510, Japan

Received 19 June 2004, received in revised form 4 November 2004; accepted 27 December 2004 Available online 16 March 2005

Abstract

Liquid-phase adsorption—desorption characteristics and ethanol regeneration efficiency of an activated carbon prepared from waste tires and a commercial activated carbon were investigated. Water vapor adsorption experiments reveal that both activated carbons showed hydrophobic surface characteristics. Adsorption experiments reveal that the prepared activated carbon possessed comparable phenol adsorption capacity as the commercial one but clearly larger adsorption capacity of two reactive dyes, Black 5 and Red 31. It was ascertained that the prepared activated carbon exhibited less irreversible adsorption of phenol and the two dyes than its commercial counterpart. Moreover, ethanol regeneration efficiency of the prepared AC saturated with either dye was higher than that of the commercial AC. Because of its superior liquid-phase adsorption—desorption characteristics as well as higher ethanol regeneration efficiency, the prepared activated carbon is more suitable for wastewater treatment, especially for adsorbing similarly bulky adsorbates.

© 2005 Elsevier Ltd. All rights reserved.

Keywords: Activated carbon; Waste tires; Adsorption; Desorption; Ethanol regeneration; Porosity

1. Introduction

Activated carbons are widely used as adsorbents in both gas-phase and liquid-phase separation processes and are produced from various carbonaceous materials, for instance, coal, coconut shell, wood, and polymer scrap (Jankowska et al., 1991). Activated carbons were also prepared from municipal and industrial wastes such

Generally, activated carbon is used for the tertiary treatment of wastewater in many industries, for exam-

as PET waste (Tamon et al., 1999) and refuse derived fuel (RDF) (Nagano et al., 2000; Nakagawa et al., 2002). Waste tires represent another interesting source of raw material because highly mesoporous activated carbons can be prepared from waste tires rubber (Ariyadejwanich et al., 2003). Since the production of activated carbon from waste tires transforms hard-to-dispose waste to pollution-cleaning adsorbent, it is considered a doubly effective solution for environmental pollution.

^{*}Corresponding author. Tel./fax: +6622186894. E-mail address: wiwut@nanotec.or.th (W. Tanthapanichakoon).

Nomen	clature	$V_{\rm p}$	pore volume (cm ³ /g)
		Vmeso	mesopore volume (cm ³ /g)
P/P^{0}	relative pressure (dimensionless)	Vmere	micropore volume (cm ³ /g)
q_N	the amount of N ₂ adsorbed (cm ³ (STP)/g)	SBET	BET surface area (m ² /g)
g _w	the amount of water vapor adsorbed (cm3	λ_{\max}	maximum wavelength (nm)
	(STP)/g	Q	the amount of adsorbate adsorbed (g/g AC)
$R_{\rm p}$	pore radius (nm)	Ce	equilibrium concentration (mg/l)

ple, food, textile, chemical and pharmaceutical (Smisek and Cerny, 1970). In some applications, especially those involving large molecules or macromolecules which cannot easily penetrate into the micropores (<2 nm diameter) and adsorb onto them, the activated carbons should possess not only micropores but also interconnecting mesopores (Hsieh and Teng, 2000; Tamai et al., 1999). In particular, it was shown that, among several solid wastes, activated carbons prepared from PET and waste tires are highly mesoporous and bave remarkably high adsorption capacity for large molecules (Nakagawa et al., 2004).

In practice, the feasibility of the carbon adsorption process depends on many factors including the costs of regeneration and disposal of spent activated carbon. Thermal regeneration is the most common regeneration method, but 5-10% of the carbon is typically lost by attrition and burnoff during each cycle, and the cost of the required fuel is not negligible. Therefore, solvent regeneration in which negligible carbon loss by attrition occurs is an attractive alternative (Tamon et al., 1990). It should be noted that, in practice, regeneration of spent carbons is limited to granular carbons.

The purpose of the present study is to investigate the potential application of the mesoporous activated carbon obtained from waste tires to liquid-phase adsorption—desorption as well as the solvent regeneration of the spent activated carbons by ethanol.

2. Experimental

2.1. Activated carbon

Highly mesoporous activated carbon was prepared from waste tires via carbonization, HCl treatment, and steam activation. In the carbonization step, waste tire rubber was put in a quartz tube reactor and electrically heated in N₂ atmosphere from room temperature to 500°C at a constant heating rate of 5°C/min. The prepared char was immersed in 1 M HCl at room temperature for 1 day, and then the acid-treated char was thoroughly rinsed with distilled water and dried in an oven. In the activation step, the obtained char was steam-activated in a quartz tube reactor which was heated to 850°C at a rate of 20°C/min. The steam used

for activation was generated from a heated pot at a constant rate of $0.5\,\mathrm{g/min}$, and was introduced to the reactor with a $200\,\mathrm{cm}^3/\mathrm{min}$ flow of N_2 . Accordingly, the partial pressure of the water vapor in the N_2 stream was around 46 kPa and the achieved average % burn-off was around 65%. For comparison, a commercial activated carbon, CAL (Calgon Co. Ltd., USA), was used. The particle sizes of the prepared activated carbon and the commercial one are $600\,\mu\mathrm{m}$ and $425\,D\times1700\,L\,\mu\mathrm{m}$, respectively.

2.2. Characterization of activated carbons

The pore size distribution, BET surface area $S_{\rm BET}$, mesopore volume $V_{\rm meso}$, and micropore volume $V_{\rm micro}$, of the AC samples were determined from N₂ adsorption and desorption isotherms measured at 77 K using an adsorption apparatus (AUTOSORB-I-C, Quantachrome, USA). The pore size distributions and the $V_{\rm meso}$ values were evaluated by applying the Dollimore Heal method (Dollimore and Heal, 1964) to the desorption isotherm, whereas the t-plot method (Lippens and de Boer, 1965) was used to estimate the $V_{\rm micro}$ values. Furthermore, the adsorption isotherms of water vapor on the activated carbons were measured using another adsorption apparatus (BELSORP 18, BEL Japan Inc., Japan).

2.3. Batch adsorption-desorption experiments

Phenol (Fisher Scientific UK Limited, UK) and two reactive dyes, Black 5 and Red 31 (Asia Dyestuff Industries, Thailand), were selected as adsorbates. Their molecular sizes and structures, which were estimated using the WINMOPAC program, are shown in Fig. 1. Several solutions of various initial concentrations were prepared by diluting the adsorbates with distilled water and the AC powder was left in contact with the prepared solutions for sufficiently long times to reach equilibrium which are normally 10, 14, and 15 days for phenol, Black 5, and Red 31, respectively. To maintain their well-mixed condition, these mixtures were put in a shaking water bath which was kept at 30°C. The amount adsorbed was determined from the difference in the initial and residual concentrations of the adsorbates in the liquid phase. After the adsorption

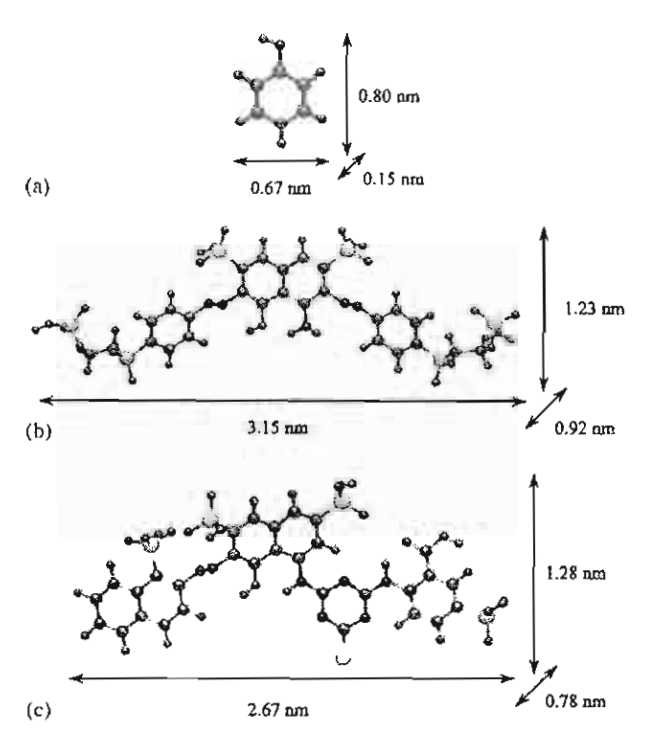


Fig. 1. Molecular sizes and structures of adsorbates: (a) Phenol (C_6H_5OH); (b) Black 5 ($C_{26}H_{21}N_5O_{19}Na_4S_6$); (c) Red 31 ($C_{30}H_{15}N_7O_{15}Na_5Cl$).

step, the activated carbons were filtered and then left in contact with distilled water for the same time duration as the previous adsorption. The ultimate concentration of the adsorbate in the liquid phase was measured and the amount desorbed was determined. The concentrations of the adsorbates were determined using a UV-visible spectrophotometer (UV-6405, Jenway, England) at the calibrated maximum wavelengths (λ_{maxx}) of 270, 595, and 540 nm for phenol, Black 5, and Red 31 solutions, respectively.

Generally, adsorption characteristics on activated carbons in liquid phase depend on pH because the surface charge changes with pH. The surface functional groups contribute to the surface charge. We can get information on the pH dependence from the following review paper (Moreno-Castilla, 2004) and book (Radovic et al., 2000). Though we did not do experiments with varied pH, the change in the surface charge with pH on the carbons prepared from waste tires is not different from the typical commercial activated carbon because the hydrophobicity of the carbon prepared is almost the same as the commercial carbon and the surface functional groups are also the same (Nakagawa et al., 2004). Hence, we consider that the present results can generally be applied by taking into account the previous works (Moreno-Castilla, 2004; Radovic et al., 2000) even though the influence of pH on the adsorption characteristics on the carbon prepared is not experimentally clarified.

2.4. Ethanol regeneration of spent activated carbons

We select ethanol as a regenerant because we have published the following papers on solvent regeneration of spent activated carbons (Tamon et al., 1990; Tamon and Okazaki, 1993, 1996, 1997). Ethanol regeneration was applied to activated carbons which adsorbed 40 kinds of adsorbates (Tamon et al., 1990). In all nine solvents were used in the solvent regeneration of the spent activated carbons (Tamon et al., 1990). For the regeneration of activated carbons which adsorbed phenol, ethanol is found to be a better solvent than 2,4-dioxane; acetone, N,N-dimethylformamide, methanol, benzene, tetrahydrofuran and triethylamine.

To investigate the efficacy of ethanol regeneration, the spent activated carbons saturated with the adsorbates were filtered and dried in a N_2 stream at 110 °C. The adsorbates were next desorbed by ethanol at 30 °C for the same time duration as the previous adsorption. The regenerated AC powder was filtered and the residual ethanol was removed with nitrogen at 110 °C. The regenerated activated carbon was again used for adsorption of the same adsorbate.

Though elucidation of the mechanism of solvent regeneration is beyond the scope of the present paper, we may consider the following mechanism (Tamon et al., 1990; Tamon and Okazaki, 1993, 1996, 1997). Because the solubility of the adsorbate in the solvent in higher than in water, the adsorbate is desorbed from the activated carbon in the solvent. Another role of the solvent is to weaken the adsorptive interaction between the adsorbate and adsorbent surface. We also tried to elucidate the mechanism by using a semi-empirical molecular orbital calculation (Tamon and Okazaki, 1996, 1997).

It should be pointed out that if the preadsorbed compounds are different, the efficiency of ethanol regeneration would be different. Generally, the regeneration of activated carbons which adsorb aromatic compounds with electron-donating substituent groups such as phenol, cresol, etc. is quite difficult. On the other hand, aromatic compounds with electron-attracting substituent groups can easily be desorbed from activated carbons by solvent (Tamon et al., 1990). After solvent regeneration, the used solvent containing the adsorbates are distilled and the solvent is used again for regeneration. This is a typical process of solvent regeneration.

3. Results and discussion

3.1. Characteristics of activated carbons

The N₂ adsorption-desorption isotherms on the activated carbon prepared from waste tires, AC-Tire, and the commercial activated carbon, AC-Com, are

shown in Fig. 2, where q_N and P/P^0 are the amount of N₂ adsorbed and the relative pressure, respectively. From the shape and hysteresis of the isotherms, it was plausible to suggest that AC-Tire shows a more extensive mesoporous structure than AC-Com. It was found that, even though the N2 adsorption capacity of the former was nearly the same as that of the latter at low relative pressures, the former showed clearly larger adsorption capacity than the latter at P/P^0 above 0.3. By applying Dollimore-Heal method, the pore-size distributions of both activated carbons were obtained and presented in Fig. 3, where R_p and V_p are the pore radius and pore volume, respectively. It was obvious that AC-Tire shows significantly higher mesoporosity and has the tallest peak in pore size distribution at the pore radius around 2 nm.

The porous properties calculated from the above isotherms are given in Table I. It is clear that AC-Tire has an obviously larger $V_{\rm meso}$ value than, and nearly the same $V_{\rm micro}$ and $S_{\rm BET}$ values as AC-Com. Fig. 4 shows the adsorption isotherms of water vapor on both activated carbons at 25 °C, where $q_{\rm W}$ is the amount of water vapor adsorbed. This figure shows that the amounts of water vapor adsorbed on AC-Tire are almost the same as those on AC-Com at $P/P^0 < 0.4$. This more or less indicates that the surface nature of AC-Tire is as nearly hydrophobic as that of AC-Com.

3.2. Adsorption-desorption characteristics

The adsorption-desorption isotherms of phenol, Black 5, and Red 31 on both activated carbons are shown in Figs. 5-7, respectively. Q and C_e are the adsorbed amount and the equilibrium concentration of the adsorbate, respectively. It was found in Fig. 5 that, although the $V_{\rm micro}$ value of AC-Tire is essentially the

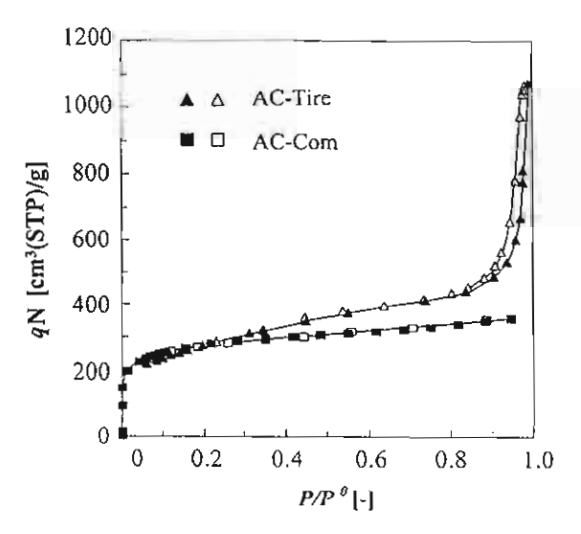


Fig. 2. N₂ adsorption-desorption isotherms of activated carbons; closed symbols: adsorption, open symbols: desorption.

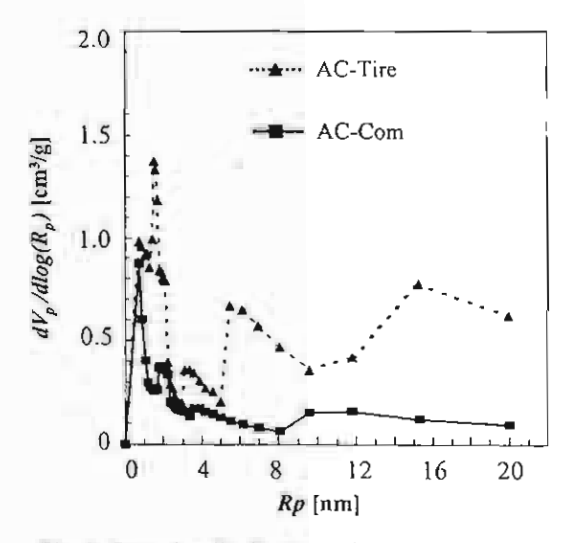


Fig. 3. Pore size distributions of activated carbons.

same as that of AC-Com, the former shows a slightly lower phenol adsorption capacity than the latter. Since the hydrophobicity of both carbons is found to be essentially the same, the difference in phenol adsorption may be attributed to the observation that the micropore size distribution of AC-Tire is somewhat different from that of AC-Com. Interestingly, a certain extent of irreversible adsorption of phenol on both activated carbons was observed which may be attributed to the fact that phenol has the electron-donating functional group, the hydroxyl group (Tamon and Okazaki, 1996).

Having a larger $V_{\rm meso}$ value, AC-Tire shows obviously higher Black 5 adsorption capacity in Fig. 6 than AC-Com. Furthermore, the hysteresis observed between the adsorption and desorption branches on both carbons signifies the appearance of irreversible adsorption, which is caused by the presence of electron-donating functional groups in Black 5, the amino and hydroxyl groups (Tamon et al., 1996). In particular, it was observed that Black 5 can be desorbed from AC-Tire more easily than from AC-Com.

As shown in Fig. 7, it is clear that the adsorption capacity of Red 31 on AC-Tire is apparently higher than that on AC-Com due to the larger $V_{\rm meso}$ value of the former. Also, the observed irreversible adsorption of Red 31 on AC-Com can similarly be explained as in the case of Black 5. In contrast, a significant amount of the adsorbed Red 31 could be desorbed from AC-Tire. It may be suggested that the mesopores play an important role in the adsorption and desorption of bulky molecular adsorbates.

3.3. Ethanol regeneration

Figs. 8-10 present the adsorption capacities of phenol, Black 5, and Red 31 on the virgin and ethanolregenerated activated carbons prepared from waste tires

Table 1 Porous properties of activated carbons

Sample	Burn-off (%)	V _{meso} (cm ³ /g)	$V_{\rm micro}~({\rm cm}^3/{\rm g})$	$S_{\rm BET}$ (m ² /g)
AC-Tire	65.0	0.79	0.37	985
AC-Com	N.A.	0.24	0 39	956

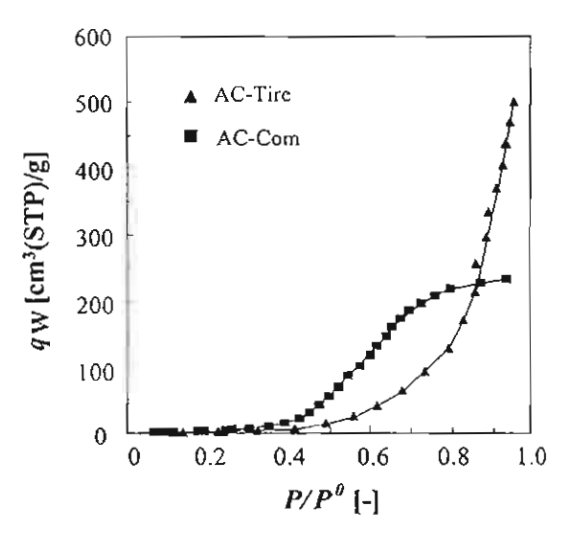


Fig. 4. Water vapor adsorption isotherms of activated carbons.

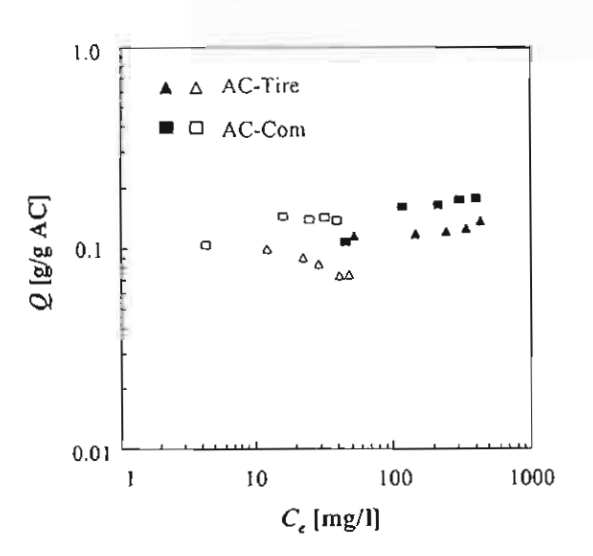


Fig. 5. Adsorption-desorption isotherms of phenol on activated carbons; closed symbols: adsorption, open symbols: desorption.

as well as their commercial counterparts. Fig. 8 reveals that the phenol adsorption capacities on AC-Tire and AC-Com regenerated with ethanol come to about 35-45% and 50-60% of those on the virgin ones, respectively. As shown in Fig. 9, after regeneration with ethanol, the activated carbon from waste tires retained Black 5 adsorption capacity in the range of 40-50% of

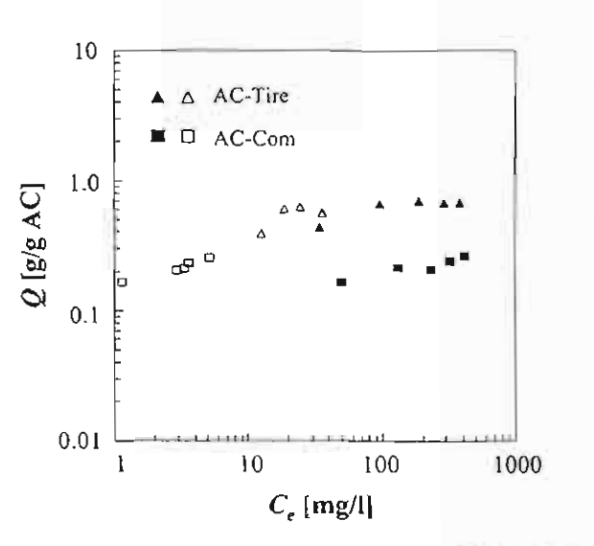


Fig. 6. Adsorption-desorption isotherms of Black 5 on activated carbons; closed symbols: adsorption, open symbols: desorption.

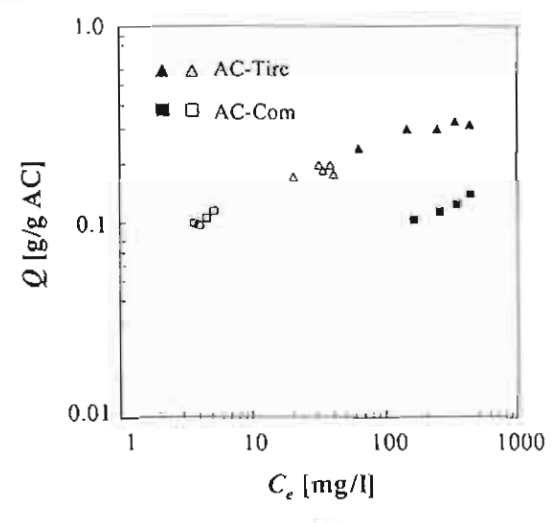


Fig. 7. Adsorption—desorption sotherms of Red 31 on activated carbons; closed symbols: adsorption, open symbols: desorption.

the virgin state, while the similarly ethanol-regenerated commercial carbon showed a significantly lower regeneration efficiency, approximately 25–30%. Similarly, it was found that the regeneration efficiencies of Red 31 on AC-Tire are significantly higher than those on AC-Com, about 30–40% versus 15–20%, respectively.

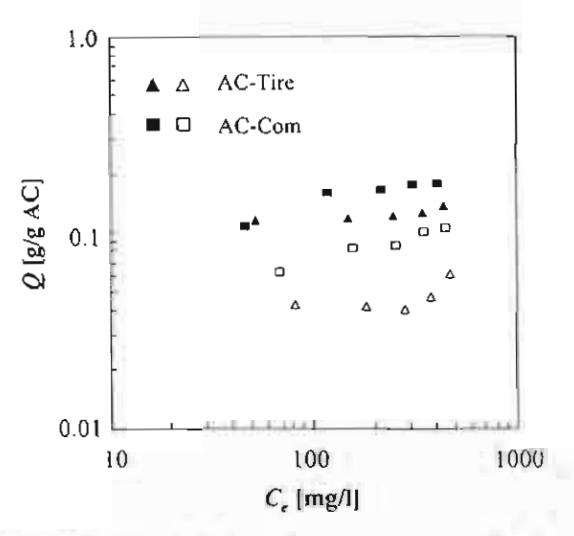


Fig. 8. Adsorption isotherms of phenol on activated carbons; closed symbols: virgin carbon, open symbols: regenerated carbon.

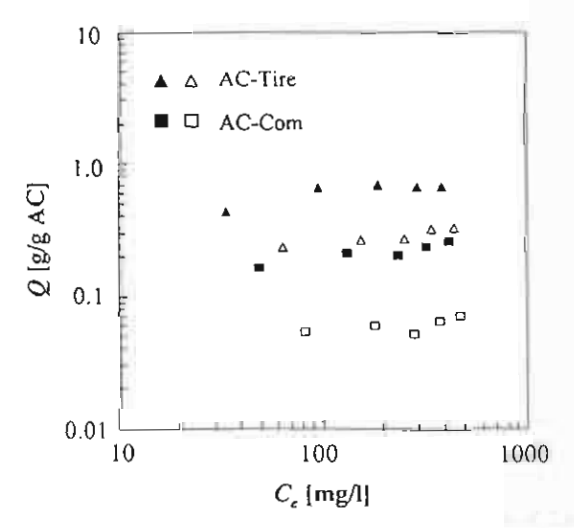


Fig. 9. Adsorption isotherms of Black 5 on activated carbons; closed symbols: virgin carbon, open symbols: regenerated carbon.

Since both reactive dyes can desorb from AC-Tire more easily than from AC-Com, it is reasonable to expect that the ethanol regeneration efficiency of the former is higher than the latter. As for phenol adsorption, AC-Tire, however, showed a lower regeneration efficiency than AC-Com. This may be attributed to the difference in the micropore size distribution of AC-Tire versus AC-Com.

In the present work, we have selected phenol and reactive dyes because ethanol regeneration of spent activated carbons which adsorb these compounds is quite difficult (Tamon et al., 1990). If aromatic compounds, whose substituent groups are electron

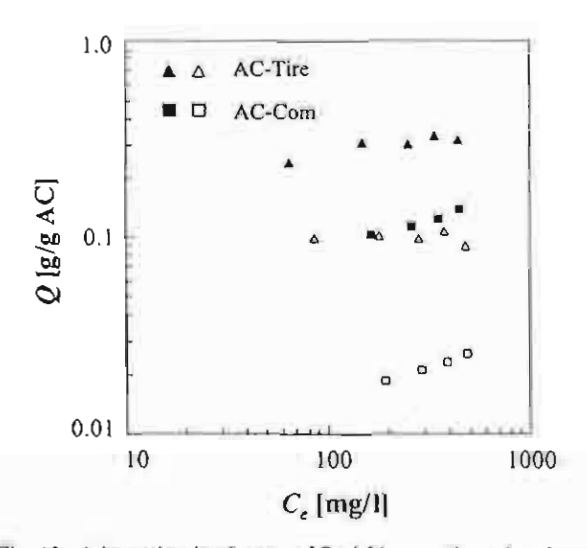


Fig. 10. Adsorption isotherms of Red 31 on activated carbons; closed symbols: virgin carbon, open symbols: regenerated carbon.

attracting, are adsorbed on the activated carbon, the regeneration efficiency becomes high (Tamon et al., 1990). Hence, we may consider that ethanol regeneration of spent activated carbons prepared from waste tires is fairly good though the obtained regeneration efficiency of 40–50% is not high for phenol and reactive dyes.

The expected effect of repeated regeneration of the spent commercial carbon which adsorbed phenol was reported in the previous papers (Tamon et al., 1990; Tamon and Okazaki, 1997). The decrease in adsorption capacity becomes small as regeneration is repeated and the capacity ultimately reaches an asymptotic value.

Since the ethanol regeneration efficiency of the spent AC-Tire used for adsorption of organic dyes is significantly higher than that of the spent AC-Com, it may be concluded that the activated carbon obtained from waste tires is practically more useful than the commercial carbon. However, even the former could not be perfectly regenerated yet. More effective regeneration conditions are under investigation.

Liquid-phase adsorption mainly depends on the molecular size of an adsorbate, the chemical structure of the adsorbate, the porous properties of an adsorbent, the surface characteristics of the adsorbent, and the kind of solvent. As for the activated carbon prepared from waste tires, we have estimated the surface hydrophobicity of the carbon by using water vapor adsorption and found that the hydrophobicity is almost the same as a typical AC-Com (Nakagawa, et al., 2004). From the results, we consider that the chemical characteristics of both activated carbons are more or less the same and the pore volume is a major factor of liquid-phase adsorption of the reactive dyes.

4. Conclusion

Highly mesoporous activated carbon was prepared from waste tires, and the adsorption-desorption characteristics of phenol and two reactive dyes on the prepared activated carbon and a commercial one were studied in the liquid phase. Furthermore, the efficiency of the ethanol regeneration of the spent activated carbons was investigated. The following conclusions have been obtained.

- Although the prepared activated carbon possesses essentially the same micropore volume and BET surface area as a commercial one, the former shows a slightly lower phenol adsorption capacity than the latter.
- (2) Having a significantly larger mesopore volume, the prepared activated carbon possesses higher dyes adsorption capacities than a commercial one.
- (3) The activated carbon from waste tires shows less irreversible adsorption of phenol and the two dyes than a commercial carbon.
- (4) Ethanol regeneration efficiency of the prepared activated carbon saturated with the two dyes is higher than that of a commercial one.
- (5) Therefore the activated carbon obtained from waste tires is more suitable for the adsorption of bulky molecular adsorbates than a commercial one.

Acknowledgments

P.A. and W.T. receive research fellowship under the Royal Golden Jubilee Ph.D. Program and financial support from the Senior Research Scholar Project of Thailand Research Fund (TRF), respectively. P.J. receives research assistantship under University-Industry Linkage Project of CU. H.T., S.R.M., and K.N. visited CU and pursued this collaborative research under TJTTP-JBIC Project of CU.

References

- Ariyadejwanich, P., Tanthapanichakoon, W., Nakagawa, K., Mukai, S.R., Tamon, H., 2003. Preparation and characterization of mesoporous activated carbon from waste tires. Carbon 41, 157-164.
- Dollimore, D., Heal, G.R., 1964. An improved method for the calculation of pore size distribution from adsorption data. J. Appl. Chem. 14, 109-114.

- Hsieh, C., Teng, H., 2000. Influence of mesopore volume and adsorbate size on adsorption capacities of activated carbons in aqueous solutions. Carbon 38, 863-869.
- Jankowska, H., Swiatkowski, A., Choma, J., 1991. Active Carbon. Ellis Horwood, Chichester, UK.
- Lippens, B.C., de Boer, J.H., 1965. Pore system n catalysts V: the t-method. J. Catal. 4, 319-323.
- Moreno-Castilla, C., 2004. Adsorption of organic molecules from aqueous solutions on carbon materials. Carbon 42, 83-94.
- Nagano, S., Tamon, H., Adzumi, T., Nakagawa, K., Suzuki, T., 2000. Activated carbon from municipal waste. Carbon 38, 915-920.
- Nakagawa, K., Tamon, H., Suzuki, T., Nagano, S., 2002. Preparation and characterization of activated carbons from refuse derived fuel (RDF). J. Porous Mater. 9, 25-33
- Nakagawa, K., Namba, A., Mukai, S.R., Tamon, H., Ariyadejwanich, P., Tanthapanichakoon, W., 2004. Adsorption of phenol and reactive dye from aqueous solution on activated carbons derived from solid wastes. Water Res. 38, 1791-1798.
- Radovic, L.R., Moreno-Castilla, C., Rivera-Utrilla, J., 2000.
 Carbon materials as adsorbents in aqueous solutions. In:
 Radovic, L.R. (Ed.), Chemistry and Physics of Carbon, vol.
 27. Marcel Dekker, New York, pp. 227-405.
- Smisek, M., Cerny, S., 1970. Active Carbon. Elsevier, Anisterdam, Netherlands.
- Tamai, H., Yoshida, T., Sasaki, M., Yasuda, H., 1999. Dye adsorption on mesoporous activated carbon fiber obtained from pitch containing yttrium complex. Carbon 37, 983-989.
- Tamon, H., Okazaki, M., 1993. Influence of surface oxides of carbonaceous adsorbent on liquid-phase desorption characteristics of aromatic compounds. In: Suzuki, M. (Ed.), Fundamentals of Adsorption. Kodansha, Tokyo, Japan, pp. 663-668.
- Tamon, H., Okazaki, M., 1996. Desorption characteristics of aromatic compounds in aqueous solution on sold adsorbents. J. Colloid Interface Sci. 179, 181-187.
- Tamon, H., Okazaki, M., 1997. Influence of surface oxides on ethanol regeneration of spent carbonaceous adsorbents. J. Colloid Interface Sci. 196, 120-122.
- Tamon, H., Saito, T., Kishimura, M., Okazaki, M., Toei, R., 1990. Solvent regeneration of spent activated carbon in wastewater treatment J. Chem. Eng. Japan 23, 426-432.
- Tamon, H., Atsushi, M., Okazaki, M., 1996. On irreversible adsorption of electron-donating compounds in aqueous solution. J. Colloid Interface Sci. 177, 384-390.
- Tamon, H., Nakagawa, K., Suzuki, T., Nagano, S., 1999. Improvement of mesoporosity of activated carbons from PET by novel pre-treatment from steam activation. Carbon 37, 1643-1645.



Available online at www.sciencedirect.com



Carbon 43 (2005) 525-531



www.elsevier.com/locate/curbon

Improvement of mesoporosity of carbon cryogels by ultrasonic irradiation

N. Tonanon a,*, A. Siyasukh a, W. Tanthapanichakoon b, H. Nishihara c, S.R. Mukai c, H. Tamon c

Department of Chemical Engineering, Faculty of Engineering, Chulalongkorn University, Bangkok 10330, Thailand
 National Nanotechnology Center, 111 Thailand Science Park, Klong Luang, Pathumthani 12120, Thailand
 Department of Chemical Engineering, Graduate School of Engineering, Kyoto University, Katsura, Kyoto 615-8510, Japan

Received 25 August 2004; accepted 9 October 2004 Available online 24 November 2004

Abstract

Mesoporous carbon gels are usually obtained by pyrolyzing resorcinol-formaldehyde (RF) gels, which are synthesized via the sol-gel polycondensation of resorcinol with formaldehyde in a slightly basic aqueous solution followed by drying. However, mesoporous carbon gels cannot be prepared under the conditions of high catalyst concentration or high pH of RF solution even by using supercritical drying or freeze drying. In this work, mesoporosity of carbon cryogels is improved by ultrasonic irradiation to RF solution. It is found that the gelation time of RF solution becomes greatly short by ultrasonic irradiation and that ultrasonic can improve mesoporosity of carbon cryogels prepared at high catalyst concentration (C/W). Although the carbon cryogels prepared from C/W = 80 mol/m³ have no mesopores, the carbon sonogels prepared by ultrasonic irradiation under the same catalyst condition have sharp mesopore size distribution. The utilization of ultrasonic in the preparation of RF gel is an interesting way in improving mesoporosity of carbon gels prepared at high C/W or pH.

© 2004 Elsevier Ltd. All rights reserved.

Keywords: A. Porous carbon; B. Pyrolysis; C. Adsorption, Scanning electron microscopy; D. Porosity

1. Introduction

RF gel was first synthesized by Pekala et al. by solgel polycondensation of resorcinol (R) and formaldehyde (F) with sodium carbonate (C) as a basic catalyst [I-4]. Carbon cryogels prepared by freeze drying and pyrolysis of RF gels are porous materials with moderately high BET surface areas (500-1200 m²/g) and large mesopore volume (>0.89 cm³/g) [5], therefore, carbon cryogels are suitable for many applications such as column packing materials for high-performance liquid chromatography, electrode materials for electric double layer capacitors and materials for catalyst supports

The unique power of ultrasonic in driving chemical reactions under extreme conditions comes from the hot-spot and thermal theories [12], extreme pressures and hot spots accompanied by rapid heating and cooling

⁽both metal catalyst and enzyme). Morphologies and porous properties of carbon cryogels can be changed in many ways. From previous work [6–9], the effect of catalyst concentration, drying conditions of gels, gelation conditions and carbonizations on porous properties of RF carbon cryogels, have been investigated. The effect of surfactant types and concentrations was also studied [10]. Previous works on the effect of synthesis method (RF sol-gel polycondensation) such as reactant concentration, initial pH of RF solutions, gelation and curing on the properties of RF gel have been reported in the review [11].

^{**}Corresponding author. Tel.: +66 2 218 6865; fax: +66 2 218 6877. E-mail address: nattaporn.t@chula.ac.th (N. Tonanon).

created by cavitation bubble collapse [13]. Cavitation has three stages, nucleation, growth and impulsive collapse of cavitating bubbles [14]. The number of cavitation site depends on the ultrasonic intensity [15].

Since there are many special properties can be obtained after sonication, there are many works such as polymerization and other chemical reactions accelerated by ultrasonies. In some materials, structure has been improved outstandingly by ultrasonic irradiation. Most of interesting works and unique role of ultrasonic in chemistry can be found in the reviews [13-15]. Ultrasonic is found to be very helpful by increasing reaction rates and yields of products, shortening the reaction time, altering the reaction path and making milder reaction conditions (lower temperature) possible. Some examples of interesting effects of ultrasonic irradiation on increasing reaction rate and yield, decreasing reaction time and introducing milder reaction condition are obviously shown in increasing the reactivity of reactive metals (Mg, Li or Zn) [15], the addition-rearrangement in the reaction of 4-bromobenzenesulfonyl azide with 1,2cyclohexadiene and cyclohexene substrates [12] and the synthesis of diaryl ethers [12]. There are many applications of ultrasonic into polymer chemistry for both thermoplastics and thermosetting polymers such as dispersion of particles in polymer matrix, shortening the reaction time [12,16,17]. Many sonochemistry researches have been done in polymerization (initiation) of vinylic monomers such as styrene, methylmethacrylate and N-vinylcarbazole [12,15].

When ultrasonic irradiation is applied on sol-gel reaction, sonogel with unique properties such as porous property and density is obtained [14]. The obvious result of ultrasound irradiation is outstandingly shorter gelation time in the preparation of sonogel [14]. In silica sonogel finer, sphere-shaped pore was obtained compared to the silica aerogels [15]. For zirconium sonogel, short gelation time and much smaller particle size was observed after ultrasonic irradiation [15]. For ormosils after sonication, denser structure and less porosity were obtained [14]. Interesting structural changes was found in nanostructural materials [15]. After sonication hydroxyapatite got better crystallinity and shorter reaction time. For MoS₂, a big difference in morphology was observed by high intensity ultrasonic irradiation. Interesting results can be seen from inorganic sonogels. What will happen when ultrasonic is applied into organic resorcinol-formaldehyde polycondensation has not been reported.

In this work, ultrasonic with different intensities is applied to RF gel prepared under different catalyst concentrations (the ratio of catalyst to water, C/W) and the effect of ultrasonic on porous properties of carbon cryogels is clarified. In general by using high C/W (high pH) RF carbon gel with high surface area, good mesoporosity and short gelation time cannot be obtained. Hence, the authors want to emphasize that ultrasonic can make

synthesis of mesoporous RF carbon gel (with short gelation time) at high C/W (high pH) possible. Ultrasonic irradiation in the preparation of RF gel is an interesting way in improving mesoporosity of carbon gels prepared at high C/W (high pH).

2. Experimental

2.1. Preparation of RF sonogels

In order to prepare RF hydrogels, resorcinol-formaldehyde (RF) solutions were prepared from resorcinol (C₆H₄(OH)₂) (R), formaldehyde (HCHO) (F), sodium carbonate (Na₂CO₃) (C) and distilled water (W). All chemicals are research grades from Wako Pure Chemical Industries. Na₂CO₃ and distilled water were used as a basic catalyst and a diluent, respectively. The synthesis conditions are presented in Table 1. Here the molar ratio of resorcinol to formaldehyde (R/F) was fixed at 0.5. Ultrasonic was applied into RF solution by Vibra Cell model VC 130 (frequency 20 kHz, adjustable output between 0 and 30 W) with a titanium alloy transducer (6mm in diameter) at different intensities 0, 57, 78, 106 W/cm². The temperature of RF solution was controlled at $\sim 308 \pm 5 \,\mathrm{K}$. When no cavitation bubbles was observed in high viscosity RF solution the ultrasonic irradiation was stopped then the RF solution was poured into the cylindrical glass tube (inner diameter = 3 mm, length = 40 mm) followed by aging for 7 days at 348 K in the oven. Before freeze drying, water in RF sonogels was replaced by solvent exchange with t-butanol for three times. After that, RF sonogels were freeze-dried at 263 K for 3h to obtain freeze dried RF sonogel.

2.2. Preparation of carbon sonogels

RF carbon sonogels were obtained by pyrolyzing RF sonogels at 1023 K. Pyrolysis was conducted under a 200 cm³-STP/min flow of nitrogen gas. At first, the RF cryogels were heated to 523 K at a constant heating rate of 250 K/h, and were kept at this temperature for 2h. Then they were heated to 1023 K at a constant heating rate of 250 K/h and were kept at 1023 K for 4h.

2.3. Characterization of gels

The porous properties of RF carbon gels were determined by the N_2 adsorption method using an adsorption apparatus (BEL Japan Inc.; BELSORP28). BET surface area, $S_{\rm BET}$ mesopore size distribution, and mesopore volume, $V_{\rm mes}$, were evaluated. The pore size distributions and $V_{\rm mes}$ were obtained by applying the Dollimore–Heal method [18] to their desorption isotherms.

The cross sections of RF carbon gels were observed by a scanning electron microscope (JEOL, JSM-6700F).

Table I
Synthesis conditions and porous properties of RF carbon gels prepared by application of various ultrasonic intensities with different catalyst concentrations in the starting RF solution

Sample	R/C (mol/mol)	C/W (mol/m³)	Ultrasonic intensity (W/cm²)	S _{BET} (m ² /g)	V _{mes} (cm ³ /g)	V _{mic} (cm '/g)	Mesopore size peak radius (nm)
Cl	400	20	iù.	650	0.53	0.19	4
C2	400	20	57	590	0.67	0.16	6
C3	400	20	78	630	0.91	0.17	6
C4	400	20	106	660	0.93	0.16	6
C5	200	40	0	750	0.61	0.17	3
C6	200	40	57	690	0.73	0.16	3
C7	200	40	78	740	0.75	0.17	3
C5	200	40	106	740	0.71	0.17	3
C9	100	80	0	360	0.08	0.12	ND
C10	100	80	57	720	0.60	0.10	2
CH	100	80	78	740	0.65	0.11	2
C12	100	80	106	690	0.54	0.11	2

Mole ratio of resorcinol to formaldehyde (R/F) = 0.5 mol/mol; ratio of resorcinol to water (R/W) = 0.89 g/cm^3 ; gelation temperature (T_{gel}) = 308 K; pyrolysis temperature (T_{pyro}) = 1023 K ND = not detected.

3. Results and discussion

The authors have experimentally elucidated that RF sol-gel polycondensation cannot be proceeded by only ultrasonic irradiation. Therefore, it is found that the catalyst, Na₂CO₃, is required as a basic catalyst for the polycondensation. Here the effect of ultrasonic on gelation time of RF gels and the porous properties of carbon cryogels prepared under several catalyst concentrations (C/W = 20, 40 and 80 mol/m³) has been investigated.

3.1. Effect of ultrasonic irradiation on gelation time of RF gel

Fig. 1 shows the gelation time of RF gels and RF sonogels prepared under the conditions of C/W = 20, 40 and 80 mol/m3. One can see that the gelation time decreases with the increase of the catalyst concentration (C/W) from Fig. 1(a). This result can be explained by the model proposed by the authors [9]. During the first stage of the gelation process, each particle grows individually at the position of the catalyst, subsequently they aggregate with each other to form the interconnected structure, and finally the cross-linked structure (RF hydrogel) is formed. If the concentration of catalyst is high (large C/W), the starting points of the growth of the particles exist densely. Since they easily aggregate and form interconnected structure, the gelation time becomes short. On the other hand, if the concentration of catalyst is low (small C/ W), the starting points exist sparsely. Hence, it takes long time to form the cross-linked structure.

It is found that RF sonogels prepared under the conditions of ultrasonic intensity = 57, 78, 106 W/cm² have much shorter gelation time compared with their RF carbon gel counterparts from Fig. 1(a) and (b). One can also see that the gelation time of RF sonogel depends on both the catalyst concentration in the starting RF

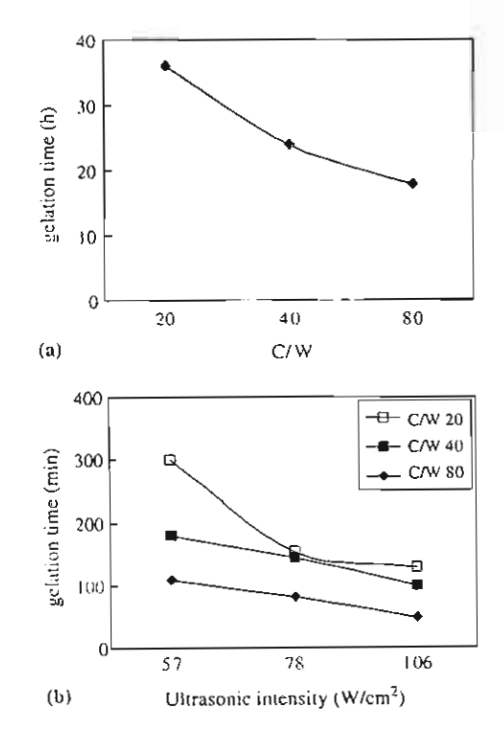


Fig. 1. Gelation time of (a) RF gel and (b) RF sonogel.

solution and the ultrasonic intensity. For example, when RF starting solutions with C/W = 20, 40 and 80 mol/m³ are irradiated by ultrasonic 106 W/cm², the gelation times change from 36, 24 and 18 h to 130, 100 and 50 min, respectively. For the same C/W ratio, the higher ultrasonic intensity, the shorter gelation time it becomes.

3.2. Effect of ultrasonic irradiation on porous properties of carbon gel

Fig. 2 shows adsorption and desorption isotherms of nitrogen on carbon cryogels and carbon sonogels

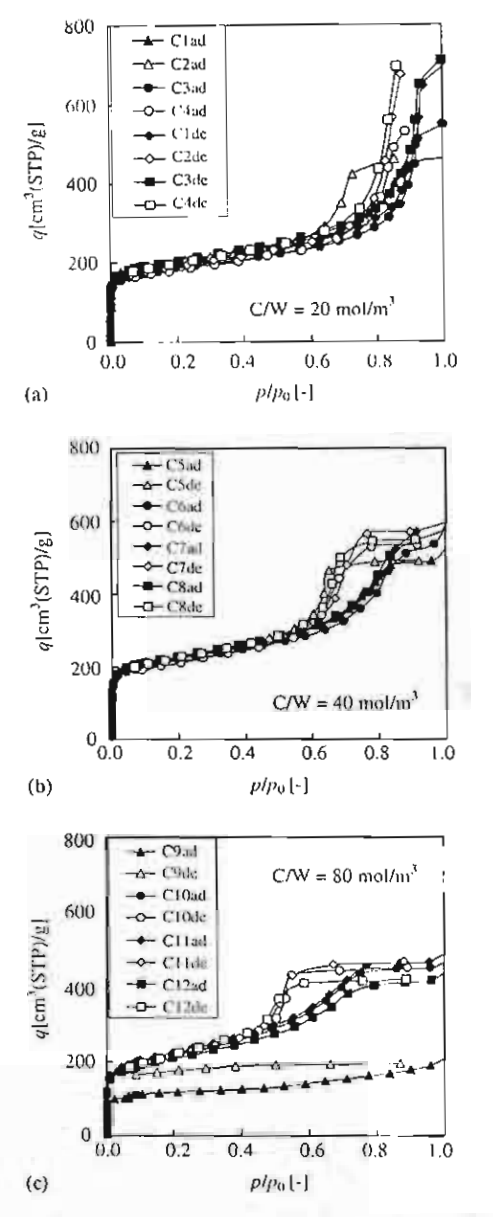


Fig. 2. Adsorption and desorption isotherms of nitrogen on RF carbon gel (with different C/W ratios and ultrasonic intensities) at 77 K. Closed symbols, adsorption; open symbols, desorption.

prepared under the conditions shown in Table 1. This figure suggests that the amounts of nitrogen adsorbed (q) at low relative pressure (p/p_0 , p: partial pressure, p_0 : saturated vapor pressure) are the same in all RF carbon gels (except the carbon gel prepared from $C/W = 80 \text{ mol/m}^3$: pH = 7.4) and sonogels. The results mean that microporosities of the carbon cryogels and sonogels are the same. On the other hand, the amounts of nitrogen adsorbed at high relative pressure are different between carbon gels and carbon sonogels prepared from C/W = 20 and 40 mol/m^3 . This difference means the

change of mesoporosity of carbon gels by irradiation of ultrasonic. Although the change in mesoporosities of carbon gel and carbon sonogel is very obvious for C/W = 20 mol/m³, the change is not big for carbon gels prepared under the condition of C/W = 40 mol/m³. Note that for RF carbon gel prepared from C/W = 80 mol/m³ (starting pH = 7.4), the shape of isotherm is different from other RF carbon gels or sonogels. The amounts of nitrogen adsorbed are increased by irradiation of ultrasonic. The outstanding changes in both microporosities and mesoporosities of carbon gel and carbon sonogel can be observed for C/W = 80 mol/m³ (starting pH = 7.4).

Fig. 3 shows pore size distributions of the carbon gels and the carbon sonogels prepared under the conditions

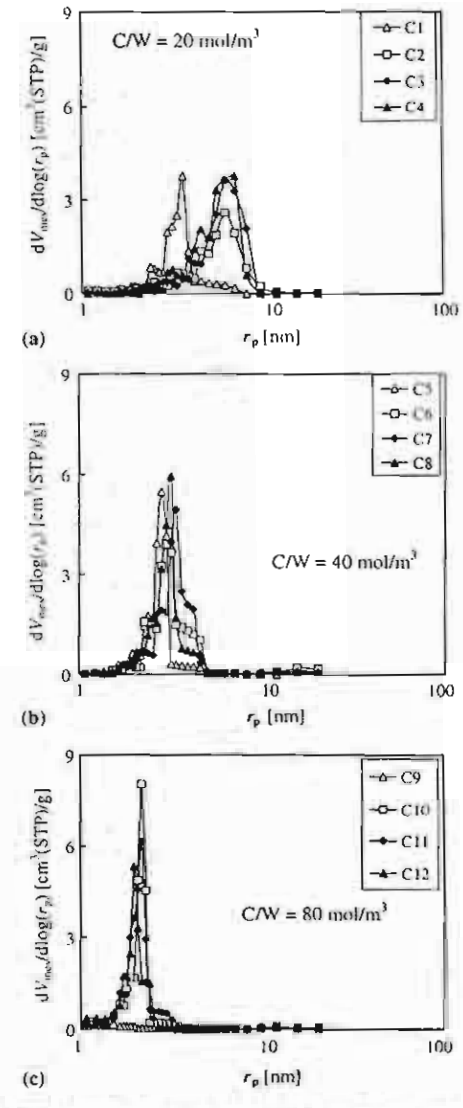


Fig. 3. Mesopore size distributions of RF carbon gel (with different C/W ratios and ultrasonic intensities).

shown in Table 1. There are remarkable changes in mesopore size distribution between carbon gels and carbon sonogels prepared from C/W = 20 and $80 \,\text{mol/m}^3$ (starting pH = 7.4). However, from both adsorption-desorption isotherm of nitrogen in Fig. 2 and mesopore size distribution in Fig. 3, there is no outstanding effect of ultrasonic intensities on porous properties except the carbon sonogel prepared from $C/W = 20 \,\text{mol/m}^3$ with ultrasonic intensity $57 \,\text{W/cm}^2$.

Although the carbon cryogel (C9) prepared from $C/W = 80 \text{ mol/m}^3$ (starting pH = 7.4) has no mesopores as shown in Fig. 3, the carbon sonogels prepared for the same C/W has sharp pore size distributions. Under the condition of $C/W = 20 \text{ mol/m}^3$, the peak radius of pore size distribution, r_{peak} of the carbon gels increases from 4nm to 6nm by ultrasonic irradiation. However, no change in r_{peak} can be observed on the carbon cryogels prepared for $C/W = 40 \text{ mol/m}^3$.

The preparation conditions and the porous properties of carbon cryogels and carbon sonogels are shown in Table 1. Ultrasonic can clearly increase $V_{\rm mes}$ and $r_{\rm peak}$ of carbon cryogels prepared under the conditions of C/W = 20 and $80\,{\rm mol/m^3}$ (starting pH = 7.4). Especially, $S_{\rm BET}$, $V_{\rm mes}$ and $r_{\rm peak}$ of carbon sonogels are much larger than those of carbon cryogel counterparts. Hence, ultrasonic irradiation to RF solution can outstandingly improve the mesoporosity of carbon cryogel prepared under the conditions of C/W = 20 and $80\,{\rm mol/cm^3}$ (high pH).

3.3. Effect of ultrasonic irradiation on inside structure of carbon gel

Fig. 4 shows the cross sections of carbon cryogel and carbon sonogel prepared under the condition shown in Table 1. The carbon cryogels (C1 and C5) are composed of primary particles of nanosize as shown in Fig. 4. The carbon sonogels (C4 and C8) have the similar inside structure to C1 and C5, respectively. Hence the pictures suggest that the carbon sonogels with almost the similar structure to the carbon cryogels can be prepared by using ultrasonic under the conditions of C/W = 20 and 40 mol/cm³.

The cross sections of carbon cryogel (C9) prepared under the condition of C/W = 80 mol/m³ suggests that the inside structure is collapsed during freeze drying and pyrolysis and that the cryogel has no mesopores, which result is confirmed by the mesoporosity estimated by nitrogen adsorption as shown in Fig. 3. Hence, it is impossible to keep mesoporosity during freeze drying and pyrolysis for C/W = 80 mol/m³. On the other hand, the cross section of carbon sonogel (C12) prepared from C/W = 80 mol/m³ suggests that the sonogel is composed of primary particles of nanosize similar to C1, C4, C5 and C8. The mesoporosity of carbon cryogel prepared

from high catalyst concentration (high pH) can be greatly improved by irradiation of ultrasonic.

3.4. Effect of ultrasonic irradiation on preparation of carbon cryogels

Most works on mesoporosity improvement of carbon gels focus only on the initial stage of gelation such as addition and condensation but in the present work ultrasonic is applied to RF solution from the beginning until viscosity of RF solution becomes too high. Sonication can shorten the gelation time of RF solution and greatly improve mesoporosity of RF carbon gels. The results may be explained by co-working of ultrasonic and catalyst during the gelation process of RF solution such as the addition reaction, polycondensation, cluster formation, particle formation and gelation. It has been reported that ultrasonic can generate more free radicals and active species [15] which results in faster addition reaction together with faster condensation and gelation as a consequence. Since ultrasonic irradiation increases the number of free radicals/active species in RF solution and promotes the addition reaction at the first stage of the process, the gelation time is shorten by ultrasonic irradiation as shown in Fig. 1. However, ultrasonic does not alter the reaction path because the catalyst concentration influences both carbon gel and carbon sonogel as shown in Figs. 2 and 3.

In addition to promotion for sol-gel polycondensation and gelation by free radicals and active species, ultrasonic may have another role in the next step. Pitting in the surface (much larger surface area compared with cavitation bubbles' resonance) caused by ultrasonic irradiation has been reported [12]. Hence, there is also a possibility that ultrasonic can play an important role in improving porous properties such as $S_{\rm BET}$ and $V_{\rm mes}$ due to the surface modification by ultrasonic irradiation.

In this present work the authors have particular interest in synthesis of RF carbon gels at high C/W (high pH), which have high surface area, good mesoporosity and short gelation time. It has been reported that carbon xerogels synthesized from the starting RF solution with pH = 6.5 or higher are non-porous [19]. RF carbon cryogels prepared at C/W = 45 mol/m³ have no mesoporosity [9]. From previous works, a suitable pH range for synthesis of RF carbon gels is 5.4-7.6 [11]. In the present work for C/W = 80 mol/m3 (starting pH = 7.4), after ultrasonic irradiation carbon sonogels with good mesoporosity can be obtained, on the contrary without ultrasonic irradiation mesoporous structure can not be obtained in carbon gel. There is also an outstanding improvement in mesopore volume and mesopore size distribution when $C/W = 20 \text{ mol/m}^3$ (lower pH). It is obviously seen that when C/W or pH is high in starting RF solution, sonochemistry produces a mesoporous

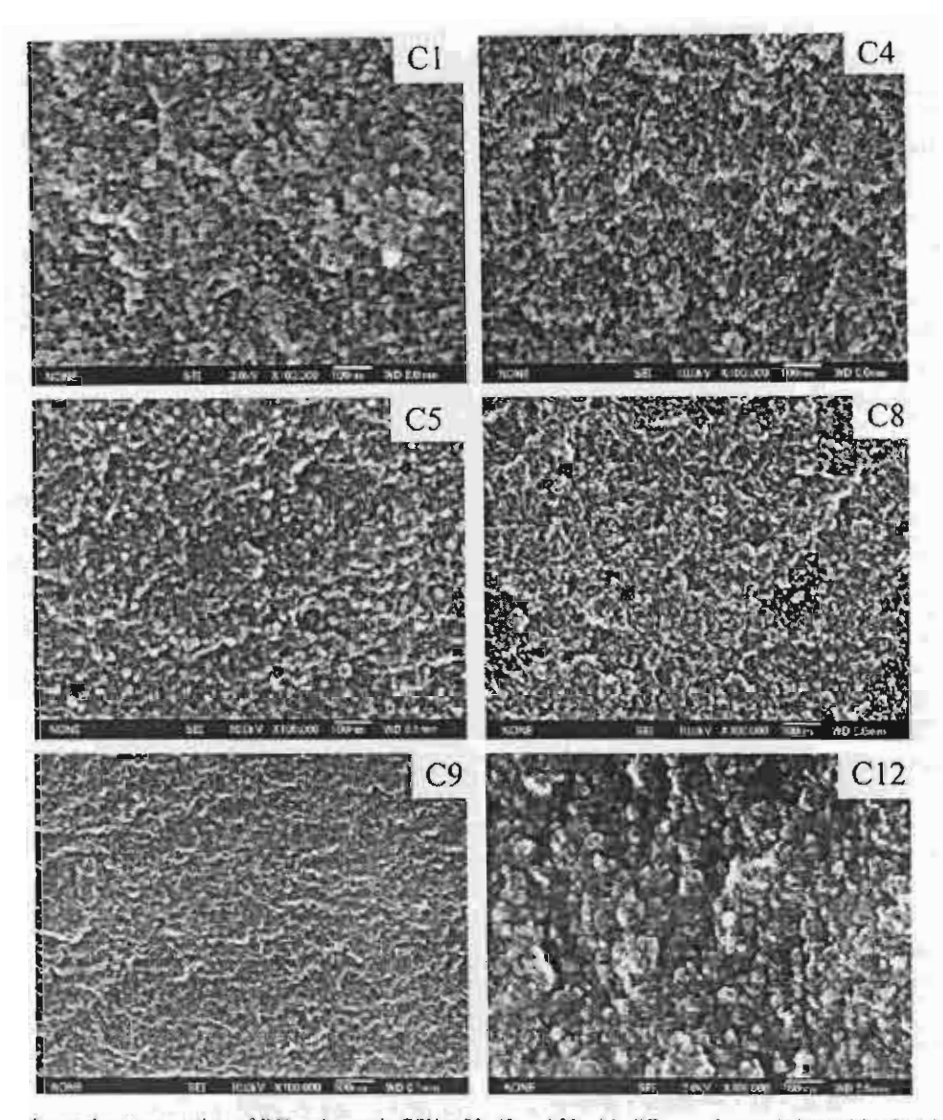


Fig. 4. SEM micrographs on the cross section of RF carbon gels C/W = 20, 40 and 80 with different ultrasonic intensities 0 and 30 W/cm² (sonogel).

carbon which cannot be produced by methods already established.

The mesoporosity of carbon cryogels prepared from C/W = 20 and 80 mol/cm³ (high pH) are improved by ultrasonic irradiation. On the other hand, ultrasonic does not influence porous properties of carbon cryogels prepared for C/W = 40 mol/cm³. However, the authors cannot completely explain the effect of ultrasonic on the changes in mesoporosity of carbon cryogels with the catalyst concentration used in sol-gel polycondensation.

RF carbon gels with good mesoporosity can be synthesized at high C/W (high pH) by using ultrasonic irradiation to the RF solution. In other word the synthesis conditions of RF carbon gel are expanded by ultrasonic application. Although the carbon gels prepared in this work are not outstandingly different from carbon gels prepared in previous works. However, further investiga-

tion will be needed in near future for this interesting work on resorcinol-formaldehyde carbon sonogels.

4. Conclusion

By ultrasonic irradiation together with suitable catalyst concentrations, interesting improvement in mesoporosity of resorcinol-formaldehyde carbon gels can be observed especially when the catalyst concentration (C/W) or pH is high. The gelation time is also greatly shortened by ultrasonic irradiation. Although the carbon cryogels prepared by the existing synthesis method at C/W = 80 mol/cm³ have no mesopores, the carbon sonogels prepared by ultrasonic irradiation under the same catalyst concentration have sharp mesopore size distribution. Hence, ultrasonic irradiation is useful for expanding the synthesis conditions of mesoporous car-

bon cryogels via sol-gel polycondensation of resorcinol with formaldehyde.

Acknowledgments

This research was partially supported by the Thai Government (Matching Fund), the Thailand Research Fund (Senior Researcher Scholarship), Thai-Japan Technology Transfer Project (TJTTP)/Chulalongkorn University, Metal and Materials Research Institute/Chulalongkorn University, Silver Jubilee Research Fund/Chulalongkorn University, National Metal and Materials Technology Center (Thailand). N.T. would like to thank Dr. Hathaichanok Vanichsri for an introduction to sonochemistry.

References

- Pekala RW. Organic aerogels from the polycondensation of resorcinol with formaldehyde. J Mater Sci 1989;24:3221-7.
- [2] Pekała RW, Alviso CT, Kong FM, Hulsey SS. Aerogels derived from multifunctional organic monomers. J Non-Cryst Solids 1992;145:90-8.
- [3] Pekala RW, Alviso CT. Carbon aerogels and xerogels. Mater Res Soc Symp Proc 1992;270:3–14.
- [4] Pekala RW, Schaefer DW. Structure of organic aerogels. 1. Morphology and scaling. Macromolecules 1993;26:5487–593.
- [5] Tamon H, Ishizaka H, Yamamoto T, Suzuki T. Preparation of mesoporous carbon by freeze drying. Carbon 1999;37:2049-55.
- [6] Yamamoto T, Sugimoto T, Suzuki T, Mukai SR, Tamon H. Preparation and characterization of carbon cryogel microspheres. Carbon 2002;40:1345-51.

- [7] Tamon H, Ishizaka H, Yamamoto T, Suzuki T. Influence of freeze-drying conditions on the mesoporosity of organic gels as carbon precursors. Carbon 2000;38:1099-105.
- [8] Yamamoto T, Nishimura T, Suzuki T, Tamon H. Effect of drying conditions on mesoporosity of carbon precursors prepared by solgel polycondensation and freeze drying. Carbon 2001;39:2374-6.
- [9] Yamamoto T, Nishimura T, Suzuki T, Tamon H. Control of mesoporosity of carbon gels prepared by sol-gel polycondensation and freeze drying. J Non-Cryst Solids 2001;288:46-55.
- [10] Tonanon N, Tanthapanichakoon W, Yamamoto T, Nishihara H, Mukai SR, Tamon H. Influence of surfactants on porous properties of carbon cryogels prepared by sol-gel polycondensation of resorcinol and formaldehyde. Carbon 2003;41:2981-90.
- [11] Al-Muhtaseb SA, Ritter JA. Preparation and properties of resorcinol-formaldehyde organic and carbon gels. Adv Mater 2003;15:101-14.
- [12] Pestman JM, Engberts JBFN, Jong FD. Sonochemistry: theory and applications. Recl Trav Chim Pays-Bas 1994;113:533-42.
- [13] Suslick KS, Didenko Y, Fang MM, Hyeon T, Kolbeck KJ, McNamarallI WB, et al. Acoustic cavitation and its chemical consequences. Philos Trans R Soc Lond A 1999;357:335-53.
- [14] Blanco E, Esquivias L, Litran R, Pinero M, Ramirez-del-Solar M, Rosa-Fox N. Sonogels and derived materials. Appl Organometal Chem 1999;13:399-418.
- [15] Suslick KS, Price GJ. Applications of ultrasound to materials chemistry. Annu Rev Mater Sci 1999;29:295-326.
- [16] Limin G, Jian L, Gang W, Zhen H. Initiation of polymerization with ultrasound in dental composite resin. Biomater Art Cell Immob Biotechnol 1992;20:125-9.
- [17] Hoshi K, Akatsu T, Tanabe Y, Yasuda E. Curing properties of furfuryl alcohol condensate with carbonaceous fine particles under ultrasonication. Ultrason Sonochem 2001;8:89-92.
- [18] Dollimore D, Heal GR. An improved method for the calculation of pore-size distribution from adsorption data. J Appl Chem 1964;14:109-14.
- [19] Job N, Pirard N, Marien J, Pirard JP. Porous carbon xerogels with texture tailored by pH control during sol-gel process. Carbon 2004;42:619-28.

Preparation and Characterization of Activated Carbons from Wastes Generated during Lactic Acid Fermentation from Garbage

Kyuya Nakagawa¹, Toru Sugiyama¹,
Shin R. Mukai¹, Hajime Tamon¹,
Yoshihito Shirai² and Wiwut Tanthapanichakoon³

'Department of Chemical Engineering, Kyoto University,
Katsura, Nishikyo-ku, Kyoto-shi, Kyoto 615-8510, Japan

'Graduate School of Life Science and System Engineering,
Kyushu Institute of Technology, 1-1, Sensui-cho, Tobata-ku,
Kitakyushu-shi, Fukuoka 804-8550, Japan

'Department of Chemical Engineering, Faculty of Engineering,
Chulalongkorn University, Bangkok 10330, Thailand

Keywords: Activated Carbon, Porosity, Mesopore, Steam Activation, Waste Material, Lactic Acid Fermentation

Activated carbons were prepared from LFG (wastes generated during Lactic acid Fermentation of kitchen Garbage). Activated carbons were prepared by conventional steam activation and via the acid treatment prior to the steam activation. Porous properties of the prepared activated carbons were evaluated from nitrogen adsorption isotherms at 77 K. Activated carbons prepared by steam activation from LFG had much more mesopores than a commercial activated carbon, and had unique broad-shaped pore size distributions. It was evident from the ultimate analysis at each preparation stage of the carbons that the activated carbons prepared from LFG contain much nitrogen as carbonaceous materials. It was found that the burnoff of nitrogen during steam activation of LFG contributes to the formation of unique pore size distributions of the activated carbons. Activated carbons prepared via the acid treatment had not only more mesopores but also more micropores than the commercial activated carbon. It was suggested that LFG was useful as a resource for practical activated carbons, especially, for mesoporous activated carbons. It was also beneficial to apply the acid treatment to improve the porous properties of the prepared activated carbons.

Introduction

More than 10 million tons of garbage is annually produced from kitchens in Japan. The treatment of kitchen garbage is a serious problem because the garbage easily decays and smells. Although the garbage can be easily composted, it is difficult for urban residents to make use of the compost from garbage because they have very little land area to utilize for it. A method for producing lactic acid, which is a raw material for biodegradable plastics, from kitchen garbage by an anaerobic reaction with microorganisms has been proposed (Shirai, 1999). The wastes generated during the anaerobic fermentation should be effectively utilized in the lactic acid production from the garbage, but a good solution has not been found yet.

Production of activated carbons from waste materials is one of the solutions for solid waste utilizaThe authors also reported a possibility of solid wastes as precursors of activated carbons in the previous papers (Nagano et al., 2000; Nakagawa et al., 2001, 2002; Ariyadejwanich et al., 2003). Refuse derived fuel, waste coffee beans and waste tires were selected as raw materials, and their usefulness as precursors of activated carbons was demonstrated. It is noteworthy in those reports that activated carbons with abundant

tion. Activated carbons have been used not only for gas purification or solvent recovery but also in various other applications. Pore size distributions of activated carbons depend on the raw materials and activation methods (Bansal et al., 1988). Investigations on the preparation of activated carbons from agricultural by-products have been well conducted (Rivera-Utrilla et al., 1991; Lopez-Gonzalez et al., 1994; Gergova and Eser, 1996; Toles et al., 1997; Lua and Guo, 1998; Xia et al., 1998). Many kinds of agricultural by-products were selected, and activated carbons with high specific surface area (500-1000 m²/g) were obtained. It is shown that some of those carbons have reasonable adsorption capacities towards organic compounds in aqueous solutions, and a practical application is anticipated.

Received on November 27, 2003. Correspondence concerning this article should be addressed to H. Tamon (E-mail address: tamon@cheme.kyoto-u.ac.jp).

Presented at the 65th Annual Meeting of The Society of Chemical Engineers, Japan, at Tokyo, March 2000.

Table 1 Carbonization yields and ash contents of chars

Char	Heating rate	Yield ^b	Ash contents	Yield (daf base)"	Ash contents
C-1	0.2	0.27	0.053	0.26	0.020
C-2	20	0.25	0.051	0.24	0.041

*heating rate at carbonization [K/min]; *carbonization yield [kg-char/kg-raw material]; *cash content [kg-ash/kg-char]; *carbonization yield (dry ash free base) [kg-carbon/kg-combustible]; *cash content after HCl treatment [kg-ash/kg-char]

mesopores are produced by applying the pre-treatment method proposed by the authors (Tamon et al., 1999; Nakagawa et al., 2003). As a consequence, the wastes generated during the lactic acid fermentation from garbage as well as agricultural by-products would be useful for producing activated carbons, and an interesting pore structure might be formed on the prepared carbons. In this paper, activated carbons are prepared from the wastes generated during the lactic acid fermentation from kitchen garbage (LFG) by a conventional steam activation method and via the acid treatment prior to the steam activation. The porous properties of the prepared activated carbons are determined by the nitrogen adsorption method at 77 K, and the effects of the carbonizing condition and the acid treatment on the properties are elucidated.

1. Experimental

1.1 Raw material

Wastes generated during the lactic acid fermentation from kitchen garbage (LFG) were used as a raw material of activated carbons. The wastes were vacuum-dried and crushed into small lumps (~5 mm). The results of the ultimate analysis of the dry LFG are as follows; C (27.2 wt%), H (57.1 wt%), N (3.60 wt%), O (10.8 wt%) and ash (1.40 wt%).

1.2 Carbonization

10 g of LFG was set in a quartz reactor and heated by an electric furnace. The reactor was kept under inert atmosphere with an N₂ flow of 80 cm³/min. The reactor was heated from room temperature to 773 K at either 0.2 or 20 K/min, and kept at the maximum temperature for 1 h. Two groups of chars were obtained, one carbonized at 0.2 K/min (C-1) and the other at 20 K/min (C-2). The obtained chars were ground in a mortar.

1.3 Acid treatment

Acid treatments of the chars were carried out to improve the porous properties of the activated carbons. Three groups of acid treated chars were prepared from group C-1 char. 1 g of the C-1 char was soaked in 100 cm³ 1.0 N HCl solution at room temperature for 24 h with continuous stirring (C-a1), in 1.2 N HNO₃ solution at room temperature for 24 h (C-a2), and in 1.2 N HNO₃ solution at 353 K for 1 h (C-a3). After

that, these samples were washed with distilled water, and then dried in an oven at 383 K.

1.4 Steam activation

Activated carbons were prepared from the chars by steam activation. 0.4 g of chars was set in a quartz reactor and heated with an electric furnace from room temperature to 1123 K at 20 K/min. The gas flow rate was 200 cm³/min and the steam concentration was 0.0025 g/cm³. Activation time (i.e., the holding time at 1123 K) was changed from 0 to 70 min in order to prepare carbons associated with different burnoffs.

1.5 Characterization of activated carbons

Adsorption and desorption isotherms of N, on the activated carbons were measured at 77 K by using a volumetric adsorption apparatus (BELSORP28, BEL Japan, Inc.). BET surface area $S_{\rm BET}$ was determined by the BET method. Micropore volume V was evaluated by the t-plot method from the adsorption isotherm. Mesopore volume V_{mes} and mesopore size distributions (range: $R_0 = 1.0-25$ nm) were estimated by applying the Dollimore-Heal method to the desorption isotherms. The adsorption isotherm of N, on Spheron 6 was adopted, which had been measured by BEL Japan, Inc., as the standard isotherm. A commercial activated carbon for dioxin adsorption was used for comparing its porous properties with those of prepared activated carbons because the activated carbon has relatively many mesopores. Ash contents of the chars obtained were determined by a thermogravimetric (TG) analyzer (TG-8120, Rigaku Co., Ltd.). Ultimate analyses of LFG and the obtained carbons were carried out by an elemental analyzer (CHN CORDER MT-3, Yanaco Analytical Instruments Co.).

2. Results and Discussion

2.1 Carbonization yield and ash contents

The carbonization yield and the ash content of the chars are listed in **Table 1**. It is confirmed that the carbonization yields of the two obtained chars are 0.27 and 0.25, and the heating rate during the carbonization does not greatly influence the char yield of LFG. Table 1 suggests that the ashes are eliminated by the acid treatment. The amount of ashes in group C-1 decreases by half in the acid treatment while that of group C-2 does not decrease much. It is considered that the

Table 2 Porous properties of activated carbons from LFG

Char	Activated carbon	Burnoff [wt%]	S _{BET} " [m²/g]	Vm² [cm³/g]	V(cm³/g)
C-I	AC-11	39	420	0.20	0.13
	AC-12	63	720	0.23	0.49
	AC-13	71	840	0.25	0.65
	AC-14	78	790	0.15	0.91
C-2	AC-21	34	340	0.15	0.08
	AC-22	61	530	0.24	0.30
	AC-23	76	680	0.26	0.51
	AC-24	84	680	0.22	0.57
	AC-com ^d		670	0.30	0.26

^{*}BET surface area; *micropore volume; *mesopore volume; *commercial activated carbon

structure of the char is changed by the heating rate (Brunner and Roberts, 1980).

2.2 Porous properties of prepared activated carbons

Porous properties of the activated carbons prepared from groups C-1 and C-2 chars are shown in Table 2. S_{BET} , V_{mic} and V_{mes} of them are plotted as a function of the burnoff in Figure 1. The BET surface area of the obtained activated carbons varies between 340-840 m²/g. Micropore volumes and mesopore volumes vary between 0.15-0.26 cm³/g and 0.08-0.91 cm³/g, respectively. Although the heating rate does not greatly influence $V_{\rm mic}$, the $V_{\rm mes}$ values of group C-1 are larger than those of group C-2 as shown in Figure 1 at higher burnoff. The difference in $S_{\rm BET}$ between the two groups is attributed to the difference in mesoporosity. Hence, it is considered that the different heating rate during carbonization results in structural changes of the chars as carbon precursors. Since the low heating rate gives high mesoporosity of activated carbons, the C-1 group of chars is used for the preparation of activated carbons via acid treatments in the following sections.

Pore size distributions of activated carbons prepared from C-1 and C-2 groups of chars are illustrated in Figure 2. It is confirmed that the development of mesopores occurs as the increase of burnoff, and that broad pore size distribution (in the region of pore radii 2-5 nm) is observed at higher burnoff. AC-14 has more pores in the region than AC-24. The shapes of the distributions of AC-14 and AC-24 are different from that of the commercial activated carbon because a larger region is highly developed in mesopores in the LFGderived carbons. One can see that the mesopores of AC-12, AC-14 and AC-24 are larger in the whole region than the commercial activated carbon. The commercial activated carbon is often used for dioxin adsorption; hence it has many mesopores compared with ordinary activated carbons. It is suggested that LFG is useful as a raw material for practical activated carbons, especially, for mesoporous activated carbons.

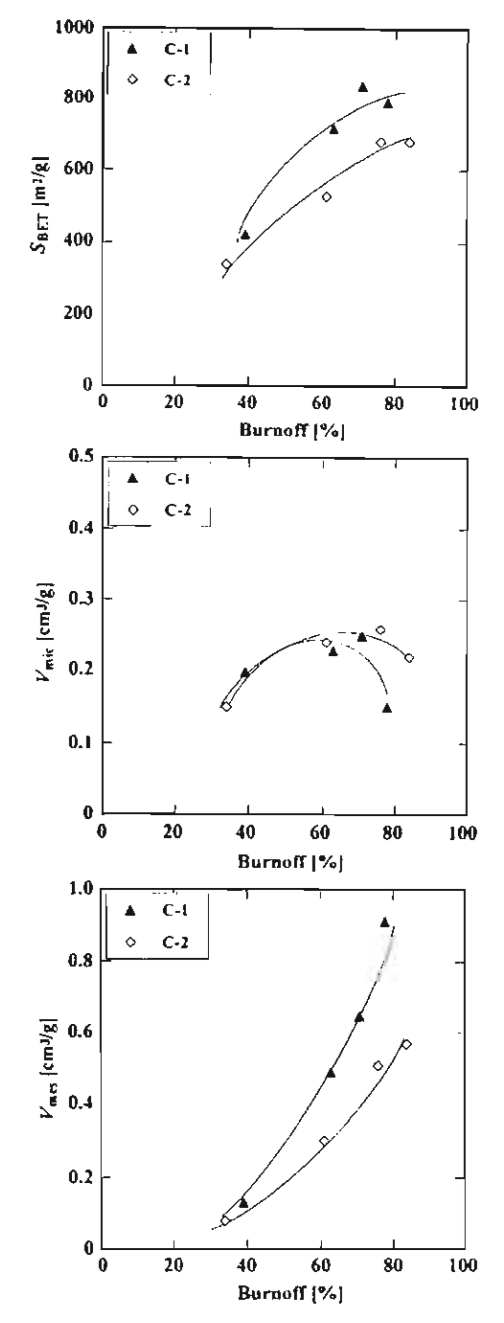


Fig. 1 Porous properties of activated carbons from LFG as a function of burnoff

It is interesting that the activated carbons from LFG have unique pore size distributions compared with the ordinary activated carbons. It is supposed that the chemical composition of LFG is different from the ordinary carbonaceous precursors because LFG is prepared via a fermentation process. For example, the LFG contains a relatively large amount of nitrogen. More precise discussion about the ultimate analysis will be given in the next section.

VOL. 37 NO. 7 2004 891

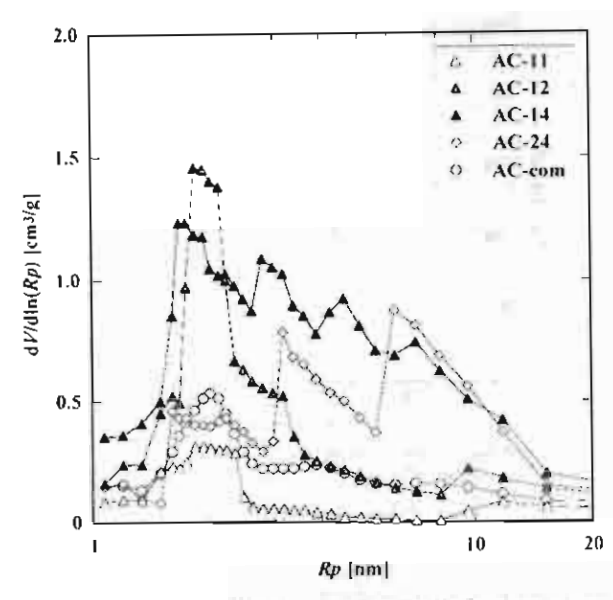


Fig. 2 Pore size distributions of activated carbons from LFG

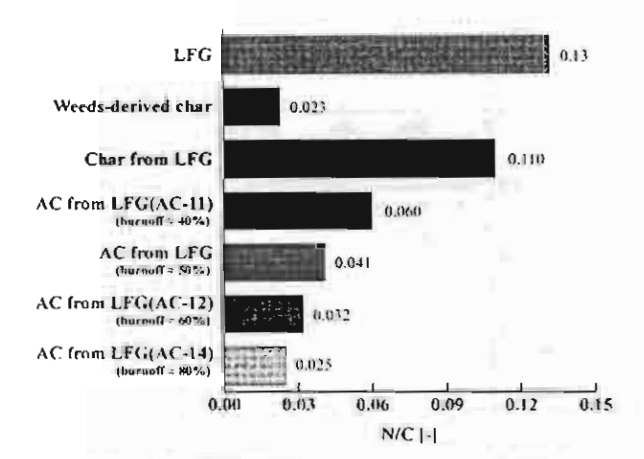


Fig. 3 Ultimate analysis of carbons from LFG

2.3 Ultimate analysis

Mesoporous activated carbons were prepared from LFG and their pore size distributions are rather unique compared with the ordinary activated carbons. This is because the difference in chemical composition of LFG (i.e., large nitrogen contents) influences the porous properties of the resultant activated carbons. Ultimate analysis at each preparation stage of a sample (precursor, char and activated carbons) was carried out, and their carbon–nitrogen ratios N/C were determined (Figure 3). The N/C of a weeds-derived char carbonized at 773 K is also shown in Figure 3 for comparison.

One can see that the N/C of the char from LFG is much higher than that of the weeds-derived char. A significant amount of nitrogen remains in the char after the carbonization. The N/C of the activated carbons

Table 3 Porous properties of activated carbons prepared via the pre-treatment

Char	Activated carbon	Burnoff [wt%]	$S_{\rm HET}^{\bullet}$ [m ² /g]	V _{mc} * [cm ³ /g]	[cm'/g]
C-a1	AC-all	35	120	0.04	0.07
	AC-a12	64	870	0.41	0.31
	AC-a13	72	1050	0.42	0.51
	AC-a14	88	1260	0.26	1.32
C-a2	AC-a21	34	280	0.15	0.11
	AC-a22	78	1190	0.41	0.80
	AC-a23	85	1410	0.40	1.09
C-a3	AC-a31	51	420	0.24	0.09
	AC-a32	86	1370	0.70	0.68
	AC-a33	87	1480	0.61	0.76

*BET surface area; *micropore volume; *mesopore volume

from LFG decreases as the burnoff during activation increases. This means that not only carbon but also nitrogen is burned off by the activation reaction, and the depletion of nitrogen is higher than that of carbon. However, the N/C ratios are still kept higher than that of the weeds-derived char. Figures 2 and 3 suggest that the mesopores develop with the burnoff of nitrogen. This is because the nitrogen content strongly influences the carbonaceous structures of the activated carbons from LFG, and these heterogeneous nitrogen-containing carbon structures contribute to the formation of unique pore structures on the activated carbons.

2.4 Porous properties of activated carbons prepared via the acid treatment

The porous properties of the activated carbons prepared from C-a1, C-a2 and C-a3 groups of chars are shown in Table 3. Their $S_{\rm BET}$, $V_{\rm min}$ and $V_{\rm mes}$ are plotted as a function of the burnoff in Figure 4. Here, the solid line indicates the porous properties of group C-1 carbons. The BET surface area of the obtained activated carbons varies between 120–1480 m²/g. Micropore volumes and mesopore volumes vary between 0.04–0.70 cm³/g and 0.07–1.32 cm³/g, respectively. It is confirmed that the BET surface areas and micropore volumes of the carbons are greatly enhanced by the acid treatments. On the other hand, mesopore volumes of the carbons prepared via acid treatments (groups C-a1, C-a2 and C-a3) are not larger than those of the carbons without acid treatments (group C-1).

Figure 5 shows the pore size distributions of the activated carbons prepared from groups C-a1, C-a2 and C-a3 of chars at high burnoff. It is confirmed that the mesopores in the region of 1.5-3 nm (AC-a13, AC-a22 and AC-a32) were developed. The shape of the distributions is sharper than that of AC-11, which possesses broad distributions, and significant development of pores cannot be seen in the region having pore radii larger than 5 nm. It is confirmed that the activated carbons prepared from LFG via the acid treatment have

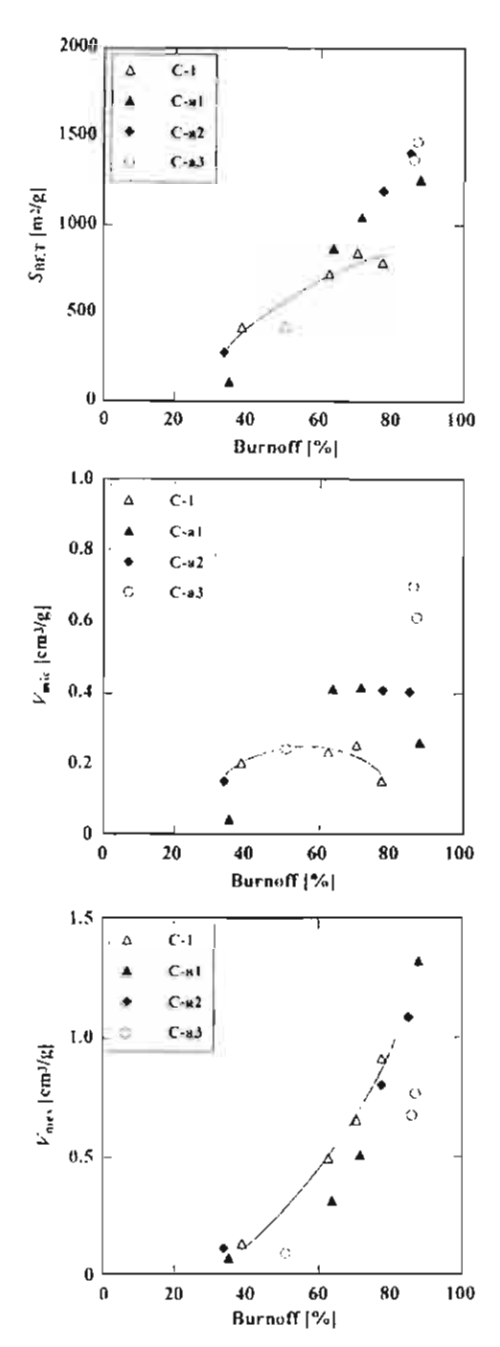


Fig. 4 Porous properties of activated carbons from LFG prepared via the pre-treatment as a function of burnoff

significantly more micropores and mesopores than the commercial activated carbon.

It should be mentioned that the trend of the pore size distributions between the activated carbons prepared with or without an acid treatment from LFG is similar to the trend of activated carbons from waste tires as reported in a previous paper (Ariyadejwanich et al., 2003). The activated carbons prepared from waste tires had mesopores of broad pore size distribu-

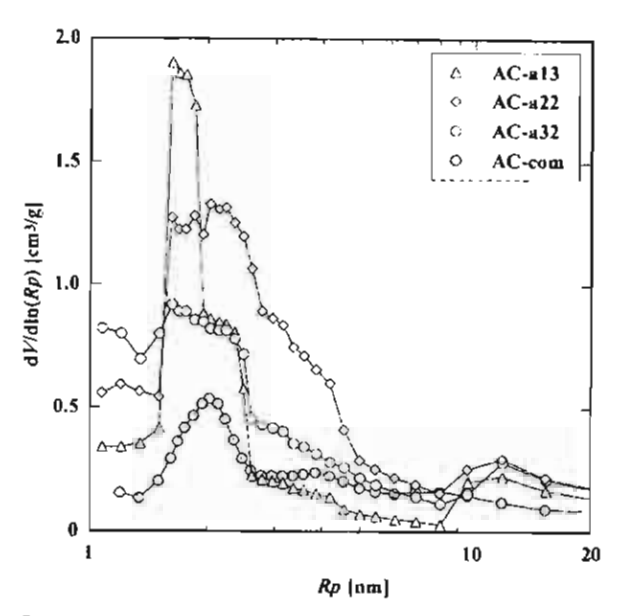


Fig. 5 Pore size distributions of activated carbons from LFG prepared via the pre-treatment

tion, while the activated carbons from the acid treated char had mesopores of sharp pore size distribution, whose peak was around pore radii 2 nm. It is considered that the acid treatment moderates the activation reactions by decreasing localized active sites belonging to the ash. The burning of carbons by activation agents occurs predominantly on these sites. If there is an abundance of active sites, the activation reactions are greatly accelerated and do not develop into large pores. However, if there are a proper number of active sites, the acceleration of the activation reaction is regulated and various pore structures are formed by different conditions of acid treatments as shown in Figure 5. Evidently LFG represents an interesting resource for activated carbons that possess many mesopores and unique pore size distributions.

Conclusions

Activated carbons were prepared from wastes generated during anaerobic fermentation of kitchen garbage, and their porous properties were evaluated from nitrogen adsorption isotherms at 77 K. Ultimate analysis at each preparation stage of a sample was carried out to elucidate the effects of nitrogen content in LFG. The effects of the acid treatment prior to the steam activation on the porous properties of the resultant activated carbons were also evaluated and discussed. The following conclusions were obtained.

1. Activated carbons prepared by steam activation from LFG have much more mesopores than the commercial activated carbon. Although the heating rate during carbonization does not greatly influence the char

VOL. 37 NO. 7 2004 893

yield, a low heating rate gives high mesoporosity. The activated carbons from LFG have unique broad-shaped pore size distributions. It is suggested that LFG is useful as a resource for practical activated carbons, especially, mesoporous activated carbons.

- 2. It is suggested from the ultimate analysis that the activated carbons from LFG contain significantly more nitrogen as carbonaceous materials, and part of the nitrogen content is burned off during steam activation. It is considered that the burnoff of the nitrogen contributes to the formation of unique pore size distributions on the prepared activated carbons.
- 3. The acid treatments prior to steam activation increase the micropore volumes of the carbons. The pore size distributions of the activated carbons prepared via acid treatments have a peak around pore radii 2 nm and less development of pores in the region having pore radii larger than 5 nm. The mesopores and micropores of the activated carbons prepared via the pre-treatments are larger than that of the commercial activated carbon. It is useful to apply the pre-treatment to improve the porous properties of the activated carbons from LFG.

Acknowledgment

This research was supported by the Special Coordination Funds for Promoting Science and Technology from Science and Technology Agency of the Japanese Government (2000). K. N. and H. T. visited Chulalongkorn University as Visiting Scholars under TJTTP-JBIC Project. W. T. receives partial financial support from TRF-RTA Program.

Literature Cited

Ariyadejwanich, P., W. Tanthapanichakoon, K. Nakagawa, S. R. Mukai and H. Tamon; "Preparation and Characterization of Mesoporous Activated Carbon from Waste Tires," Carbon, 41, 157-164 (2003)

- Bansal, R. C., J. B. Donnet and F. Stoekli; Active Carbon, p. 8, Marcel Dekker, New York, U.S.A. (1988)
- Brunner, P. H. and P. V. Roberts; "The Significance of Heating Rate on Char Yield and Char Properties in the Pyrolysis of Cellulose," Carbon, 18, 217-224 (1980)
- Gergova, K. and S. Eser, "Effects of Activation Method on the Pore Structure of Activated Carbons from Apricot Stones," Carbon, 34, 879-888 (1996)
- Lopez-Gonzalez, J., M. Molina-Sabio and F. Rodriguez-Reinoso; "Steam Activation of Olive Chars, Development of Porosity," Carbon, 32, 1407-1413 (1994)
- Lua, A. C. and J. Guo; "Preparation and Characterization of Chars from Oil Palm Waste," Carbon, 36, 1663-1670 (1998)
- Nagano, S., H. Tamon, T. Azumi, K. Nakagawa and T. Suzuki; "Activated Carbon from Municipal Waste," Carbon, 38, 915-920 (2000)
- Nakagawa, K., A. Fuke, H. Tamon, T. Suzuki and S. Nagano; "Preparation of Activated Carbons from Waste Coffee Beans," Japan. J. Food Eng., 2, 141-146 (2001)
- Nakagawa, K., H. Tamon, T. Suzuki and S. Nagano: "Preparation and Characterization of Activated Carbons from Refuse Derived Fuel (RDF)," J. Porous Mat., 9, 25-33 (2002)
- Nakagawa, K., S. R. Mukai, T. Suzuki and H. Tamon; "Gas Adsorption on Activated Carbons from Mixtures of PET with Metal Salt," Carbon, 41, 823-831 (2003)
- Rivera-Utrilla, J., E. Utrera-Hodalgo and M. A. Ferro-Garcia; "Comparison of Activated Carbons Prepared from Agricultural Raw Materials and Spanish Lignites When Removing Chlorophenols from Aqueous Solutions," Carbon, 29, 613-619 (1991)
- Shirai, Y.; "Lactic Acid Production from Urban Refuses," Proc. Asia-Pacific Chemical Reaction Engineering Symposium. pp. 383-386, Hong Kong, P.R. China (1999)
- Tamon, H., K. Nakagawa, T. Suzuki and S. Nagano; "Improvement of Mesoporosity of Activated Carbons from PET by Novel Pre-Treatment for Steam Activation," Carbon, 37, 1643-1645 (1999)
- Toles, C. A., W. E. Marshall and M. M. Johns; "Granular Activated Carbons from Nutshells for the Uptake of Metal and Organic Compounds," Carbon, 35, 1407-1414 (1997)
- Xia, J., K. Noda, S. Kagawa and N. Wakao; "Production of Activated Carbon from Bagasse (Waste) of Sugarcane Grown in Brazil," J. Chem. Eng. Japan, 31, 987-990 (1998)



Science and Technology of Advanced Materials 6 (2005) 364-369



Classification of silica fine particles using a novel electric hydrocyclone

Wongsarivej Pratarna, Tanthapanichakoon Wiwutb.*, Hideto Yoshidac

*Department of Chemical Engineering, Faculty of Engineering, Chulalongkorn University, Bangkok 10330, Thailand

bNutional Nanotechnology Center, Thailand Science Park, 111 Paholyothin Road, Klong Luang, Pathumthani 12120, Thailand

*Department of Chemical Engineering, Faculty of Engineering, Hiroshima University, Hiroshima, Japan

Received 12 January 2005; revised 15 February 2005; accepted 15 February 2005

Available online 20 June 2005

Abstract

A novel electric hydrocyclone is developed and tested. Aqueous suspensions of silica with a median diameter of 754 nm and 0.2% volumetric concentration are tested using a 20-mm-diameter hydrocyclone. The ratios of tested underflow rate to throughput are: 0, 0.1, 0.2 and 0.3. The tested volumetric flow rates are 0.083×10^{-3} , 0.117×10^{-3} and 0.167×10^{-3} m³/s (5, 7 and 10 1/min). The conical part of the electric hydrocyclone is connected to a cylindrical dust box having 42 mm diameter. This dust box has a central metal rod cone and a cylindrical metal wall between which the desired 50-volt DC electric potential or no potential is applied. The investigated lengths of the dust box are 53 and 106 mm. The three different conditions investigated are: (a) no applied electric potential, (b) positive potential applied at the central rod side and negative potential at the side wall, and (c) positive potential applied at the side wall and negative potential at the central rod side. In both the absence and presence of the underflow, the hydrocyclone with a long dust box is found to give better classification efficiency than that with a short dust box. Interestingly, the effect of electric potential is reversed with respect to the presence and absence of the underflow unexpectedly increase the 50% particle cut size when electric potential is applied. However, the effect of electric potential is reversed when there is no underflow. The electric potential can reduce the 50% particle cut size by up to 10% compared to the absence of electricity. It is found that condition (c) exhibits a stronger effect than condition (b). As expected, the higher the flow ratio, the smaller the particle cut size becomes. Based on the experimental results, an empirical correlation for the 50% particle cut size has been obtained.

© 2005 Elsevier Ltd. All rights reserved.

Keywords: Classification; Silica; Particles; Electric; Hydrocyclone

1. Introduction

Silica is a hard abrasive mineral used in numerous industries. Grinding is a common important process to produce silica fine particles. In the dry grinding process, fugitive dust is easily created. When people inhale the fine dust of crystalline silica, it can lead to silicosis, a potentially fatal lung disease. Wet grinding not only eliminates fugitive dust but also gives higher grinding efficiency. The coarse oversize particles have to be separated out and sent back for regrinding. The conventional hydrocyclone is suitable for

the classification of relatively fine, though not too fine, particles unclassifiable by sifting.

A hydrocyclone [1,2] is simple in construction, has no moving parts, requires low installation and maintenance investment for the separation, classification and thickening in many solid-liquid processes. Though originally designed to promote solid-liquid separations, they are also used for solid-solid [3], liquid-liquid [4], and gas-liquid separation [5]. Although the first patent on a hydrocyclone is about 115 years old, research works are still in progress aiming at developing new applications [6–10] or understanding the complex phenomena inside it.

Two well-known theories for particle separation in hydrocyclones are the equilibrium orbit theory [11] and the residence time theory [12]. The former assumes that particles of a given size will reach an equilibrium radial orbit position inside the hydrocyclone where their outward terminal settling velocity is equal to the inward radial velocity of the liquid. Accordingly to this theory, larger

E-mail address: wiwut@nanotec.or.th (T. Wiwut).

1468-6996/\$ - see front matter © 2005 Elsevier Ltd. All rights reserved. doi:10.1016/j.stam.2005.02.015

^{*} Corresponding author. W. Tanthapanichakoon Tel.: +66 2 564 7123; fax: +66 2 564 7122.

	nclature		
d_{50}	50% Particle cut size (µm)	L	Total length of hydrocyclone (m)
$D_{\rm c}$	Hydrocyclone body diameter (m)	Q	Suspension feed flow rate (m ³ /s)
D _i	Inlet diameter (m)	R_{f}	Underflow to throughput ratio (flow ratio) (-)
D_{o}	Overflow diameter (m)	μ	Viscosity of suspension (kg/ms)
D_{u}	Underflow diameter (m)	ρ	Density of water (kg/m ³)
$G^{"}$	Grade efficiency (-)	$ ho_{ m p}$	Density of silica particle (kg/m ³)
l	Vortex finder length (m)	17.4	

particles will attain a radial orbit position near the wall, where the axial fluid velocity has a downward direction. These particles will leave the cyclone through the underflow. The radial orbit position of smaller particles will be located near the center, inside the region where the axial fluid velocity is upward. These particles will escape through the overflow. The cut size is defined as the particle size whose equilibrium orbit is coincident with the locus of zero vertical velocity of the fluid. Such a particle will have equal chances to escape the hydrocyclone either through the underflow or through the overflow. According to the residence time theory, a particle will be separated as a function of both the position it enters the cyclone and the available residence time. The cut size will be the size of the particle which entering the equipment exactly in the center of the inlet pipe will just reach the wall in the residence time available. Several authors have used either theory to derive different equations for predicting the cut size [13-16].

The study of size classification performance, in terms of both fundamental and operational variables has been undertaken by several authors [17-20]. Empirical models have been developed [18-21] which are used for predicting hydrocyclone performance in terms of capacity, cut size and water split. With respect to the empirical modeling of small diameter hydrocyclones, some studies [22-24] describe hydrocyclone performance with new correlations for the capacity, cut size and water split. The flow pattern in hydrocyclones has been examined experimentally [18.23, 25] and theoretically [12,18,26]. Expressions for d_{50} have been obtained empirically [27-30] and theoretically [31,32]. The purpose of this study is to verify the collection efficiency of a new type of electric hydrocyclone with and without underflow under applied electric potential at the dust box. The simple correlation for the 50% cut size is discussed.

2. Materials and methods

Silica is used as the test powder which has the particle size distribution as shown in Fig. 1. The median diameter is 754 nm. The density of powder is 2210 kg/m³. Deionised water is used in all experiments. Suspensions of 0.2% solid content by weight are tested in hydrocyclone

of 20 mm body diameter. All design proportions are as shown in Table 1.

The ratios of tested underflow rate to throughput are: 0, 0.1, 0.2 and 0.3. The tested volumetric flow rates are 0.083×10^{-3} , 0.117×10^{-3} and 0.167×10^{-3} m³/s. The operating time is 20 min to assure that the system is in steady state.

The simplified experimental apparatus is shown in Fig. 2. As can be seen, it consists of a tank equipped with impeller for mixing at constant speed of 250 rpm. The discharged underflow and overflow are returned to the feed tank. The flow meter and pressure gauge are installed to measure flow rate and pressure drop. The suspension temperature in the tank is constantly controlled at 30 °C by using cooler and heater.

The conical part of the electric hydrocyclone is connected to a cylindrical dust box having 42 mm diameter. This dust box has a central metal rod cone and a cylindrical metal wall between which the desired 50-volt DC electric potential or no potential is applied. The investigated lengths of the dust box are 53 and 106 mm. The three different conditions investigated are: (a) no applied electric potential, (b) positive potential applied at the central rod side and

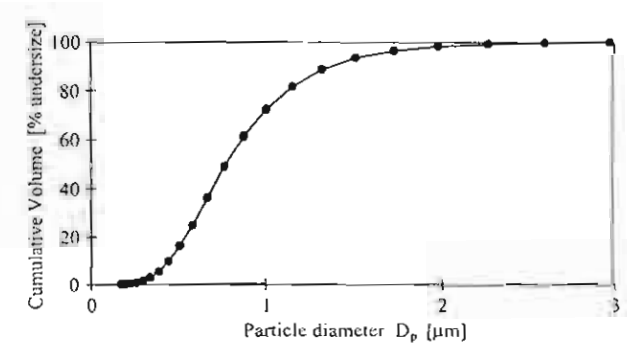


Fig. 1. Particle size distribution of the feed materials.

Table I Hydrocyclone proportions

D_i/D_c	D,JDe	$D_i J D_c$	I/D _c	UD_c	Cone angle (*)
0.20	0.16	0.20	1.00	7.40	7.68

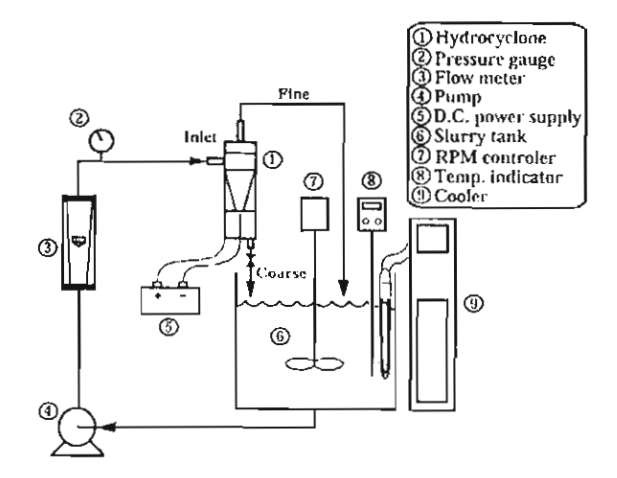


Fig. 2. Experimental apparatus.

negative potential at the side wall, and (c) positive potential applied at the side wall and negative potential at the central rod side.

The particle size analyses of both effluent streams are carried out by Laser Scattering Particle Size Distribution Analyser, HORIBA LA-920 with $(NaPO_3)_6$ 0.3 g as a dispersing agent. The concentrations of solids in the underflow and overflow samples are measured by evaporation and weighing. The grade efficiency, G, and the cut size, d_{50} , are evaluated according to the procedure recommended by Svarovsky [2].

3. Results and discussion

Fig. 3 shows the effect of dust box length in the absence of the underflow. The hydrocyclone with a longer dust box exhibits higher separation efficiency because coarse particles have less chance to escape from the vortex finder than that with a short one. At steady state, the 50% cut size are 2.260 and 1.858 μ m for the short dust box at flow rate 0.117×10^{-3} and 0.167×10^{-3} m³/s, respectively but

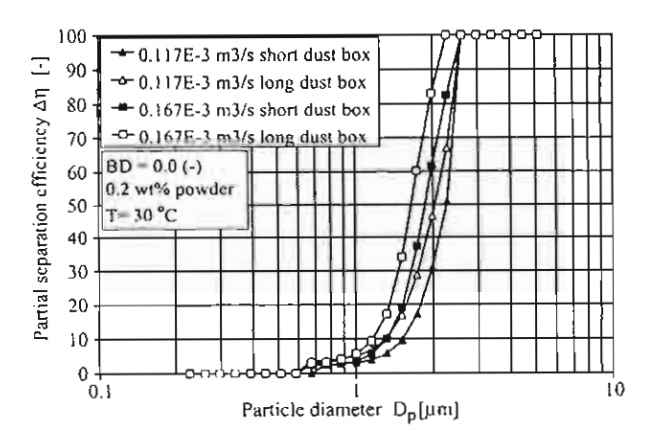


Fig. 3. Effect of dust box length in the absence of underflow.

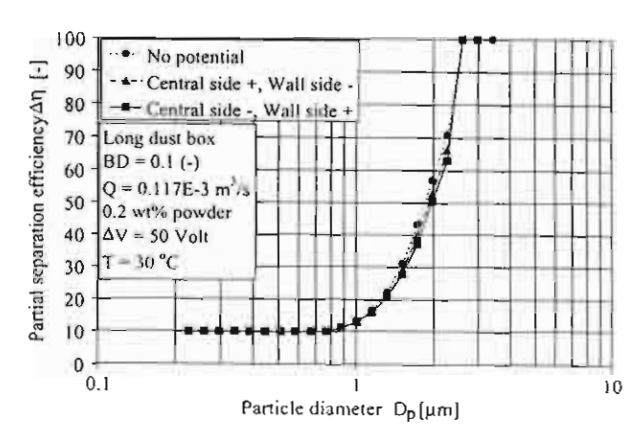


Fig. 4. Effect of potential in the presence of underflow.

decreases by 10.22% to $2.029\,\mu m$ and by 11.52% to $1.644\,\mu m$ for the long dust box.

Figs. 4 and 5 show the particle separation efficiency when electric potential is applied to the long dust box of the hydrocyclone in the presence and absence of the underflow, respectively. The effect of electric potential is reversed with respect to the presence and absence of the underflow. More specifically, the electric potential for positive pole at both the central rod and side wall increases the 50% particle cut size when compared with no application of electric potential in the presence of the underflow. The trend is reversed in the absence of the underflow. Both in the absence and presence of the underflow, effect of the potential when the positive pole is connected to the side wall is stronger than when the positive pole is connected to the central rod.

Fig. 6 shows the relationship between 50% particle cut size, d_{50} , and the underflow to throughput ratio, $R_{\rm f}$, by using the long dust box at feed flow rate 0.117×10^{-3} m³/s with and without electric potential. As expected, the higher the flow ratio, the smaller the particle cut size becomes. The choice is between high flow ratios at low-pressure drops, or low flow ratios at high-pressure drops. However,

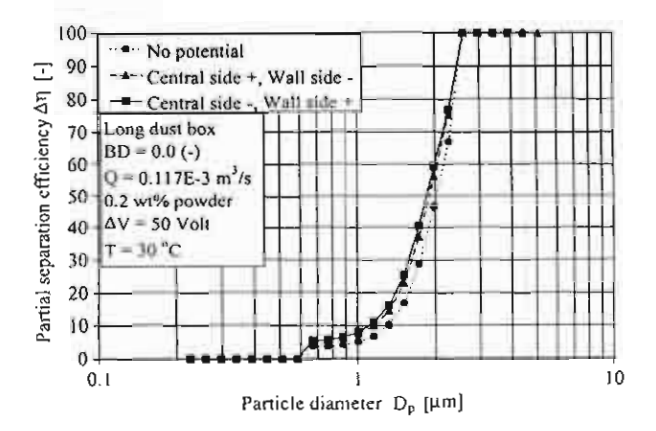


Fig. 5. Effect of potential in the absence of underflow.

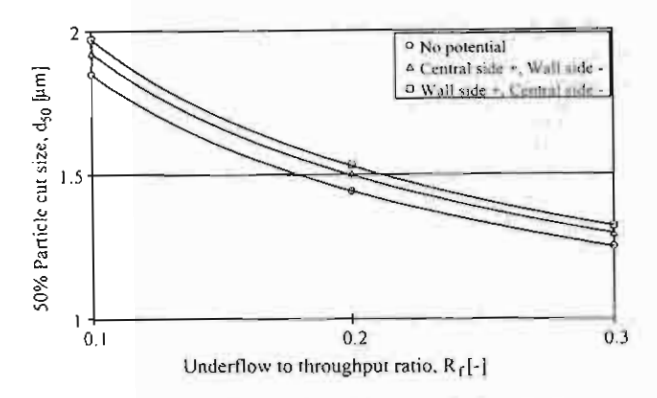


Fig. 6. Relationship between d_{50} and R_{Γ} using the long dust box.

a higher flow ratio results in a lower solid concentration and vice versa. Depending on the particle size of the feed solids and the cost of further dewatering of the solids in the underflow, the two running costs of dewatering of the solids in the underflow and pressure drop should be weighed against each other and the operating conditions optimized accordingly.

Fig. 7 shows the relationship between d_{50} and suspension feed flow rate, Q, for either the short or long dust box at operating flow ratio 0.1 with and without electric potential. As anticipated, the higher the feed flow rate, the smaller the particle cut size. The results confirm both the effect of dust box length in Fig. 3 and trend of electric potential effects in Figs. 4 and 6. Similarly, Fig. 8 shows the relationship between d_{50} and Q for short or long dust boxes with no underflow in the absence and presence of electric potential. The higher feed flow rate reduces the smaller particle cut size. The results again confirm both effects of dust box length in Fig. 3 and trend of electric potential in Fig. 5. In order to obtain the smallest cut size the long dust box should be selected and the system operated with positive electric potential at the wall and no underflow.

Fig. 9 shows the correlation results for the d_{50} in the presence and absence of underflow using parameters K_3 ,

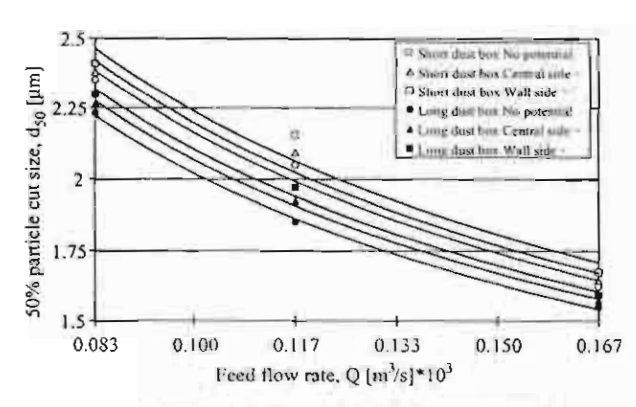


Fig. 7. Relationship between d_{50} and Q at flow ratio 0.1.

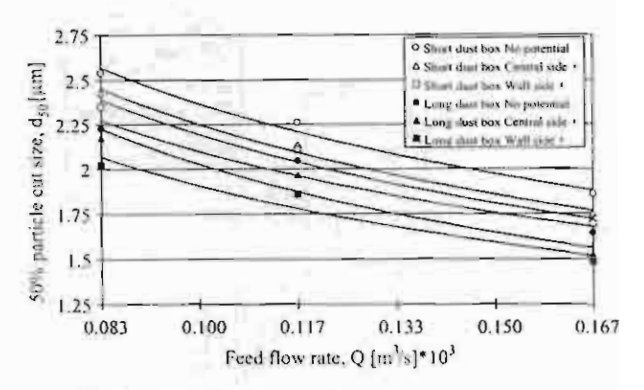


Fig. 8. Relationship between d_{50} and Q with no underflow.

 C_1 and C_2 (see Appendix A) compared with experimental results in the presence and absence of underflow, respectively. The estimated parameters are agreed well with experimental results.

4. Conclusion

In both the absence and presence of the underflow, the hydrocyclone with a long dust box is found to give better classification efficiency than that with a short dust box. Interestingly, the effect of electric potential is reversed with respect to the presence and absence of the underflow. The presence of the underflow unexpectedly increase the 50% particle cut size when electric potential is applied. However, the effect of electric potential is reversed when there is no underflow. The electric potential can reduce the 50% particle cut size by up to 10% compared to the absence of electricity. It is found that condition (c) with positive potential applied at the side wall and negative potential at the central rod side exhibits a stronger effect than condition (b) with positive potential applied at the central rod side and negative potential at the side wall. As expected, the higher the flow ratio, the smaller the particle

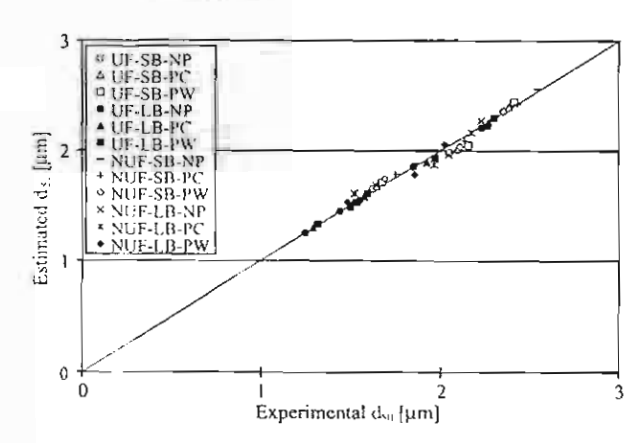


Fig. 9. Correlation results for the d_{50} in the presence and absence of underflow (UF, underflow; NUF, no underflow; SB, short box; LB, long box; NP, no potential; PC, positive center; PW, positive wall).

Table A1	
The constants for the presence and absence of the underflow in Eq. (A.4)	

		C_1	C_2		
			No	Center +	Wall+
Presence of underflow	Short dust box	3067	0	744	1698
	Long dust box	0	0	1036	1815
Absence of underflow	Short dust box	5836	0	2759	-4045
	Long dust box	0	0	-2114	-4323

cut size becomes. Based on the experimental results, an empirical correlation for the 50% particle cut size has been obtained as Eqs. (A.3)–(A.6).

Acknowledgements

P.W. acknowledged Royal Golden Jubilee PhD scholarship from Thailand Research Fund (TRF), 1-year Student Exchange Scholarship from Association of International Education Japan and useful comments from Dr Kunihiro Fukui, Hiroshima University. This work was partially supported by Thailand-Japan Technology Transfer Project and TRF-RTA Project of Prof. Wiwut Tanthapanichakoon.

Appendix A

The correlation derived from equation of motion is

$$m\frac{\mathrm{d}u_{\mathrm{r}}}{\mathrm{d}t} = -3\pi\mu D_{\mathrm{p}}(u_{\mathrm{r}} - v_{\mathrm{r}}) + \frac{mv_{\mathrm{b}}^2}{r} \tag{A.1}$$

where u and v are particle and fluid velocity that respect to coordinate, respectively. At steady state the left hand term is zero, so that:

$$D_{\rm p} = \sqrt{\frac{18 \, \mu r (u_{\rm r} - v_{\rm r})}{(\rho_{\rm p} - \rho) v_{\theta}^2}}$$

At critical particle velocity, $u_r = 0$:

$$D_{pc} = \left(\frac{18 \,\mu r(-\nu_{t})}{\rho_{p} - \rho)\nu_{\theta}^{2}}\right)^{1/2} = \left(\frac{18 \,\mu r(\nu_{R})}{(\rho_{p} - \rho)\nu_{\theta}^{2}}\right)^{1/2}$$

Normally, $v_0 = v_i$, $v_R = \alpha v_i$, $v_i = 4Q/\Pi D_i^2$ and $r = D_c/2$

$$D_{pc} = (7.07\alpha)^{1/2} \left(\frac{\mu D_c D_i^2}{(\rho_p - \rho)Q} \right)^{1/2}$$

$$= K \left(\frac{\mu D_c D_i^2}{(\rho_p - \rho)Q} \right)^{1/2}$$
(A.2)

Substitute with the cyclone dimensions and property:

$$d_{50} = K \left(\frac{0.8328 \times 10^{-3} \times 20 \times 10^{-3} \times (3.9 \times 10^{-3})^2}{(2210 - 995.647)Q} \right)^{0.5}$$

$$d_{50} = K \left(\frac{2.0862 \times 10^{-13}}{Q} \right)^{0.5}$$
(A.3)

The semi-empirical constant K is denoted by:

$$K = K_1 + C_1 + C_2 \tag{A.4}$$

where K_1 is a constant. C_1 and C_2 denote the dust box length effect and electric effect respectively. The correlation for the presence of the underflow is:

$$K_1 = \frac{15338}{Q^{0.0245} R_\ell^{0.359}} \tag{A.5}$$

The correlation for the absence of the underflow is:

$$K_1 = 79746Q^{0.0599} \tag{A.6}$$

The constants for the presence and absence of the underflow in Eq. (A.4) are shown in Table A1.

References

- [1] D. Bradley, The Hydrocyclone, Pergamon, London, 1965, p. 1.
- [2] L. Svarovsky, Solid-Liquid Separation, Butterworth, New York, 1981, p. 202.
- [3] M.S. Klima, B.H. Kim, Dense-medium separation of heavy-metal particles from soil using a wide-angle hydrocyclone, J. Environ. Sci. Health., Part A 33 (1998) 1325–1340.
- [4] C.A. Capela Moraes, C.M. Hackenberg, C. Russo, R.A. Medronho, Theoretical analysis of oily water hydrocyclones, in: D. Claxton, L. Svarovsky, M. Thew (Eds.), Hydrocyclones'96, Mechanical Engineering Publications, London and Bury Saint Edmunds, 1996, pp. 383-398.
- [5] S. Marti, Analysis of gas carry-under in gas-liquid cylindrical cyclones, in: D. Claxton, L. Svarovsky, M. Thew (Eds.), Hydrocyclones'96, Mechanical Engineering Publications, London and Bury Saint Edmunds, 1996, pp. 399-421.
- [6] V.M. Matta, R.A. Medronho, A new method for yeast recovery in batch ethanol fermentations: filter aid filtration followed by separation of yeast from filter aid using hydrocyclones, Bioseparation 9 (2000) 43-53.
- [7] M. Lubberstedt, R.A. Medronho, F.B. Anspach, W.D. Deckwer, Separation of mammalian cells using hydrocyclones, in: Proceedings of the World Congress on Biotechnology—Biotechnology 2000, Berlin, vol. 1, 2000, pp. 460–462.

- [8] M. Lubberstedt, R.A. Medronho, F.B. Anspach, W.D. Deckwer, Abtrennung tierischer Zellen mot Hydrozyklonen, Chem. Ing. Technol. 72 (2000) 1089-1090.
- [9] J.J. Cilliers, S.T.L. Harrison, The application of mini-hydrocyclones in the concentration of yeast suspensions, Chem. Eng. J. 65 (1997) 21– 26
- [10] H. Yaun, D. Rickwood, I.C. Smyth, M.T. Thew, An investigation into the possible use of hydrocyclones for the removal of yeast from beer, Bioseparation 6 (1996) 159–163.
- [11] M.G. Driessen, Theory of flow in a cyclone, Rev. L'Industrie Min. spl. (1951) 449–461.
- [12] K. Rietema, Performance and design of hydrocyclones, Parts I-IV, Chem. Eng. Sci. 15 (1961) 298-325.
- [13] L. Svarovsky, Hydrocyclones, Holt, Rinehart and Winston, London, 1984.
- [14] R.A. Medronho, Scale-up of hydrocyclones at low feed concentrations, PhD Thesis, University of Bradford, Bradford, UK, 1984.
- [15] R.A. Medronho, L. Svarovsky, Tests to verify hydrocyclone scale-up procedure, in: Proceedings of the Second International Conference on Hydrocyclones, BHRA, Bath, UK, 1984, pp. 1–14.
- [16] M. Antunes, R.A. Medronho, Bradley hydrocyclones: design and performance analysis, in: L. Svarovsky, M.T. Thew (Eds.), Hydrocyclones: Analysis and Applications, Kluwer, Dordrecht, 1992, pp. 3-13.
- [17] D.A. Dahlstrom, Cyclones operating factors and capacities on coal and refuse slurries, Mining Trans. 184 (1949) 331–422.
- [18] N. Yoshioka, Y. Hotta, Liquid cyclones as a hydraulic classifier, Chem. Eng. Jpn 19 (12) (1959) 632-640.

- [19] A.J. Lynch, T.C. Rao, Modeling and scale-up of hydrocyclone classifiers, in: Proceedings of the 11th International Mineral Processing Congress, Cagliari, 1975.
- [20] R. Plitt, Mathematical model of the hydrocyclone classifier. CIM Bulletin (1976) 114-123.
- [21] A.J. Lynch, m: D.W. Fuerstenau (Ed.), Mineral Crushing and Grinding Circuits, vol. 1 (1977).
- [22] G. Rouse, et al., Confirmation of modeling techniques for small diameter cyclones, in: P. Wood, et al. (Ed.), Third International Conference on Hydrocyclones, BHRA, Session A, 1987.
- [23] D. Bradley, D. Pulling, Flow patterns in the hydraulic cyclone and their interpretation in terms of performance, Trans. Inst. Chem. Eng. (1959) 37.
- [24] G. Brookes, et al., Hydrocyclones performance related to velocity parameters, in: Second International Conference on Hydrocyclones, BHRA, Session C, 1984.
- [25] D.F. Kelsall, A study of motion of sofid particles in a hydraulic cyclone, Trans. Inst. Chem. Eng. 30 (1952) 87.
- [26] F.J. Fontein, C. Dijksman, Recent Developments in Mineral Dressing, Institution of Mining and Metallurgy, London, 1953, p. 229.
- [27] D.A. Dahlstrom, Chem. Eng. Prog. Symp. Ser. No. 15 (1954) 50, 41.
- [28] B. Elcox, Trans. Corn. Inst. Min. Mech. Metall. Engrs 9 (1953) 26.
- [29] P.A. Haas, et al., Chem. Eng. Prog. 53 (1957) 203.
- [30] I.R.M Chaston, Trans. Inst. Mining Met. 67 (1958) 203.
- [31] A.L. De Gelder, Scaling-up of Chemical Plant and Processes, Institution of Chemical Engineers, London, 1957, p. S47.
- [32] H. Trawinski, Chemie-Ingr-Tech. 30 (1958) 85.



Science and Technology of Advanced Materials 6 (2005) 307-311



Structural improvement to quadruple service life of a high-efficiency electret filter

Weeraya Sae-lim^a, Wiwut Tanthapanichakoon^{b,*}, Chikao Kanaoka^c

^aCenter of Excellent in Particle Technology, Chulalongkorn University, Bangkok 10330, Thailand
^bNational Nanotechnology Center, Thailand Science Park, 111 Paholyothin Road, Klong Luang, Pathumtham 12120, Thailand
^cIshikawa National College of Technology, Ta 1 Aza-Kitachujo, Tsubatacho, Kahoku-gun, Ishikawa 929-0392, Japan

Received 12 January 2005; revised 14 February 2005; accepted 14 February 2005 Available online 20 June 2005

Abstract

The electret filter is composed of permanently charged electret fibers highly capable of collecting charged and uncharged nanosize particles. Compared to the ordinary non-electret fiber, the aerosol collection efficiency η of the electret fiber can initially be significantly higher. In our previous study, η of the electret fiber under dust loading is found to be approximated as the sum of the electrical and mechanical collection efficiencies. It is also shown that the former efficiency can be approximated as a logarithmic function of the dust load. Since the expensive electret filter cannot practically be cleaned and re-used, it is crucial to lengthen its service life without compromising its collection efficiency. In the present study, the time-dependent dust-loaded collection efficiencies of four electret filters with the same average packing density of 0.04 but different linear spatial distributions of the packing density along the filter thickness (0.04 throughout, front 0.03-back 0.05, front 0.02-back 0.06, front 0.01-back 0.07) are simulated and compared. The maximum penetrations and clogging points of the four filters are different. At the maximum 4% penetration through filter D (front 0.01-back 0.07) is two times higher than filter A (0.04 throughout), but the dust load at clogging point of filter D is about 4 times higher than filter A. The results show a significant difference in the distributions of the mass deposited particles along the filter thickness as time passes. As a result, it is possible to quadruple the filter service life by packing the filter loosely on the inlet side and progressively more densely towards the outlet side, while maintaining a sufficiently high aerosol collection efficiency at all times.

Keywords: Dust loading effect; Electret filter

1. Introduction

Fibrous air filters are used in various industries for dust collection and environmental protection. The electret filter is used to clean gas streams of dilute particle concentrations at low pressure drop and high efficiency. It is composed of permanently charged electret fibers highly capable of collecting charged and uncharged fine particles. Compared to the ordinary non-electret fiber, the aerosol collection efficiency of the electret fiber can initially be significantly higher, even if the aerosol particles are uncharged. Therefore, electret fibers are often employed to enhance the collection efficiency of HEPA and ULPA filters.

1468-6996/\$ - see front matter © 2005 Elsevier Ltd. All rights reserved. doi:10.1016/j.stam.2005.02.009 As the constituent fibers are covered with collected particles, the filter characteristics change with the dust load. The electret fiber has four different mechanisms of particle deposition, namely, inertial capture, interception, diffusion and electrostatic mechanism. The collection efficiency of the clean electret fiber in the initial stage is remarkably high because of its strong electrostatic effects. As dust loading proceeds, the collection efficiency of the electret filter might briefly fall as a function of dust load because the electrostatic effect exhibited by the fiber surface is screened by the deposited particles. It is known that most on-coming particles are collected on already captured particles to form complicated agglomerates on an electret fiber. As a consequence, the mechanical effect on the overall efficiency gradually picks up and ultimately becomes the dominant collection mechanism.

The collection efficiency of clean air filter are well known and widely studied [1-7]. The collection efficiency

^{*} Corresponding author. Tel.: +66 2 564 7123; fax: +66 2 564 7005. E-mail address: wiwut@nanotec.or.th (W. Tanthapanichakoon).

C_{i}	influent particle concentration (kg/m ³)	η_{OM}	mechanical single-fiber collection efficiency of
C_c	effluent particle concentration (kg/m ³)		the clean fiber (-)
d_{f}	diameter of a fiber (m)	η_{E}	electrical single-fiber collection efficiency under
C_i C_c d_f E_m	collection efficiency of filter (-)		dust load condition (-)
M	dust load in a unit filter volume (kg/m ³)	η_{M}	mechanical single-fiber collection efficiency
Pn	penetration (-)		under dust load condition (-)
ŧ	time (s)	λ_{E}	electrical enhancement factor (m³/kg)
v	face velocity (m/s)	λM	mechanical enhancement factor (m³/kg)
η	single-fiber collection efficiency (-)	α	packing density of filter (-)
η _{OE}	electrical single-fiber collection efficiency of the		
104	clean fiber (-)		

of the electret filters could initially degrade with the agglomerative deposition of particles [8-12].

The collection efficiency of the electret filter depend on many parameters such as the aerosol particle sizes, the fiber charge density, charge on particles, filtration velocity, filter packing density and the filter thickness. Kanaoka et al. [13] proposed a three-dimensional stochastic model of an ordinary fiber for the case of deposition of aerosol particles by convective Brownian diffusion. They found that the ratio of the collection efficiency of a single dust-loaded fiber to that of a clean fiber was expressible as a linear function of the mass of particles in a unit filter volume. Baumgartner and Loffler [9] studied the initial and dust loading condition of the electret filter. They were interested in the particle sizes ranging from 10 nm to 10 µm for various types of electret filters. They also simulated the particle deposition around a cylindrical electret fiber to predict the collection efficiency of clean fibers. Brown et al. [10] found that the collection efficiency of the electret filters exponentially decreases with the operation time because the electrical effect decreases. Walsh and Stenhouse [11] carried out experiments to study the effect of particle size, charges and composition on the electret filter under dust-loading condition. They showed that the uniformly small particles can reach the maximum penetration and the clogging point faster than the uniformly large particles. Kanaoka et al. [14] studied a practical three-dimensional simulation method for predicting the agglomerative deposition process of submicron aerosol particles on an electret fiber. This study led to prediction of how the morphology of particle accumulates on a constituent fiber changed and affected the collection efficiency of the filter under the dust-loaded condition. Ji et al. [12] conducted experiments to study the effect of dust loading on the collection performance of the electret cabin air filters. They proposed that the amount of charge, the particle sizes and the particle material affected the collection performance. They also showed the collection efficiency degraded as more particles deposited, and showed a minimum efficiency at steady state. Tanthapanichakoon et al. [15] developed a three dimensional stochastic model to

simulate the deposition process on an electret fiber by considering the effect of Brownian diffusion in the model. The model was shown to predict the agglomerative deposition process reasonably well and, in the case of weak electrical effects, they also approximated the collection efficiency enhancement factor as linear function of dust load.

In our previous study, the collection efficiency of the electret fiber under dust loading is found to be approximated as the sum of the electrical and mechanical collection efficiencies. It is also shown that the electrical collection efficiency can be approximated as a logarithmic function of the dust load [16]. In the present study, the time-dependent dust-loaded collection efficiencies of electret filters with the same average packing density but different spatial distributions of packing density along the filter thickness are simulated and compared. The results show a significant difference in the distributions of the mass deposited particles along the filter thickness as time passes. It is possible to significantly lengthen the filter service life by packing the filter loosely on the inlet side and progressively more densely towards the outlet side, while maintaining a sufficiently high aerosol collection efficiency at all times.

1.1. Simulation of the collection efficiency of the electret filter

In our previous study, the correlation for the collection efficiency of the electret fiber (η) is found by summing a logarithmic function for the electrical collection efficiency (η_E) and the previously obtained linear function of mechanical collection efficiency (η_M) .

$$\eta = \eta_{\rm E} + \eta_{\rm M}
= \eta_{0\rm E} [1 + (\beta \ln m + \gamma)m] + \eta_{0\rm M} [1 + \lambda_{\rm M} m]$$
or
$$\eta = \eta_{0\rm E} [1 + \lambda_{\rm E} m] + \eta_{0\rm M} [1 + \lambda_{\rm M} m],$$
(1)

$$\eta = \eta_{0E}[1 + \lambda_{E}m] + \eta_{0M}[1 + \lambda_{M}m],$$
where $\lambda_{E} = \beta \ln m + \gamma$
(2)

Under dust-loaded condition, the local aerosol concentration C and dust load m in the filter can be obtained by numerically integrating Eqs. (3) and (4) together with Eq. (2) and the applicable initial and boundary conditions.

$$\frac{\partial C}{\partial x} = -\frac{4}{\pi} \frac{\alpha}{1 - \alpha} \frac{\eta}{d_{\rm f}} C \tag{3}$$

$$\frac{\partial C}{\partial x} = -\frac{1}{v} \frac{\partial m}{\partial t} \tag{4}$$

Initial condition t=0: m=0 for 0 < x < LBoundary condition x=0: $C=C_1$ for t>0

The filter collection efficiency is calculated from $C_e = C$ at x = L as follows.

$$E_{\rm m} = 1 - \frac{C_{\rm c}}{C_{\rm i}} \tag{5}$$

To estimate the collection efficiency of the electret filter under dust-loaded condition, the following assumptions are made:

- (1) The local collection performance (between x and $x + \Delta x$) can be regarded as constant for a sufficiently short time interval (t and $t + \Delta t$).
- (2) When the local dust load a single fiber is the same, the local electrical enhancement factor is the same regardless of the fiber location in the filter and filtration time.

The simulation conditions are listed in Table 1. The simulation is carried out until the filter becomes clogged. The % penetration P is defined as $P = 100(1 - E_{\rm m})$. Table 2 shows the equation of the filter packing density of four filters. The four filters have same average packing density, $\alpha = 0.04$, but different spatial distributions of packing density along the filter thickness. Fig. 1 shows the filter packing density distribution of the filters along thickness. Fibers are packed uniformly in filter A. For filters B-D,

Table 1 Simulation conditions used

Simulation conditions used Time step $\Delta t = 0.03$ s Differential filter thickness $\Delta x = 0.00002$ m Packing density of filter $\alpha = 0.04$ (-) Face velocity of filtration = 0.1 m/s Influent dust concentration $C_t = 0.01$ mg/m³ Electret fiber diameter $d_f = 20$ μm Particle diameter $d_p = 1$ μm Electret fiber charge = 1.2×10^{-4} C/m²

Table 2 Packing density of the electret filter

Packing density
0.04
6.67L + 0.03
13.333L + 0.02
20L + 0.01

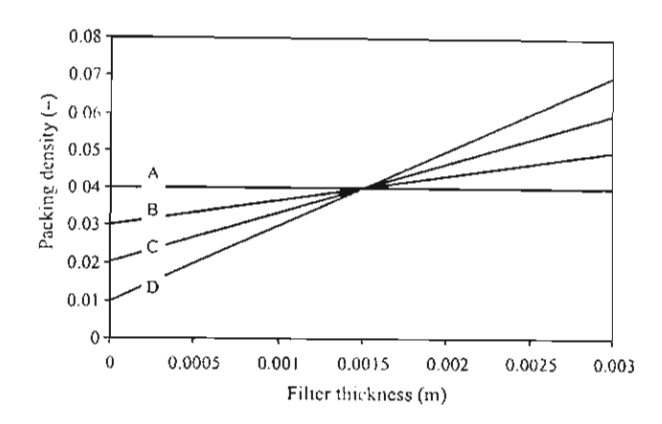


Fig. 1. Electret fiber packing density distribution along thickness.

the packing density changes along the filter thickness, with a minimum packing density at the inlet side and a maximum packing density at the outlet side of filter.

2. Results and discussion

As fine particles deposit on the fibers, their collection efficiencies increase while the filter gradually becomes clogged. Filter collection efficiency depends not only on filtration condition and particle properties, but also on the filter properties, such as fiber diameter, packing density, packing structure.

To clearly demonstrate the intended effect, the value of C_i is deliberately set quite high while the electret fiber diameter, much larger than the conventional HEPA filter. As a result, the collection efficiency would drop as low as 96% on the number basis with respect to the 1 μ m particles.

Fig. 2 compares the penetration through four different filter structures with the same average packing density. The penetrations of the four filters initially increase with dust load with filter A's raising the most rapidly. After a period of time, the penetration through all filters starts to gradually decrease and becomes zero upon clogging. In this calculation, all conditions except for the packing density distribution of fibers are equal. As expected, the maximum

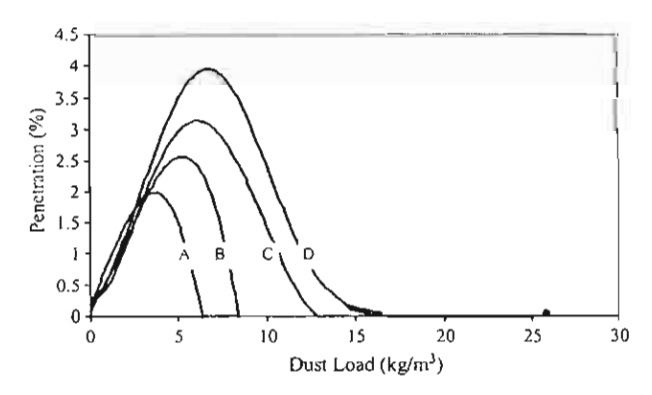


Fig. 2. Penetration of different electret fiber under loading condition.

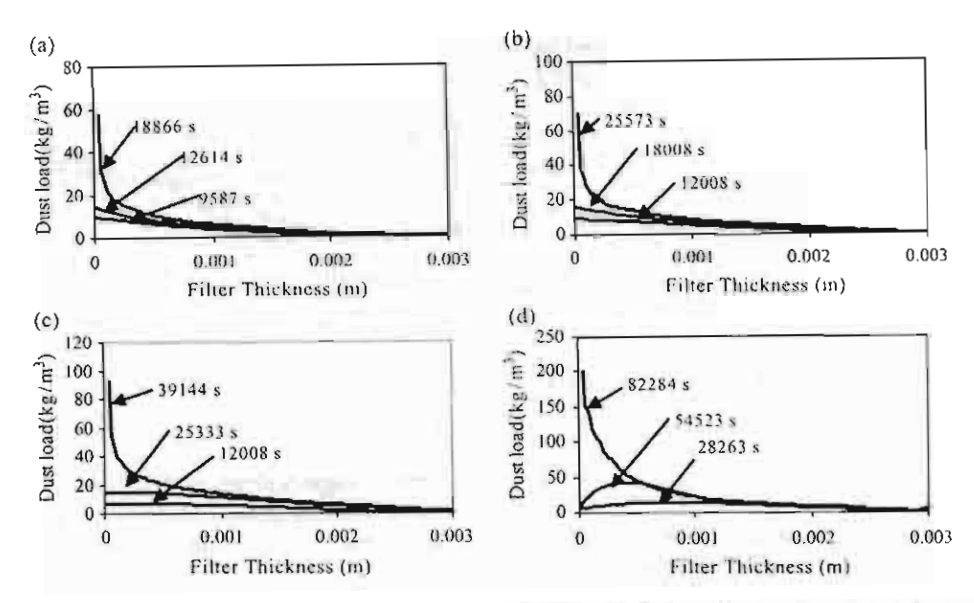


Fig. 3. Distribution of dust inside the four electret filters. (a) Filter A; (b) filter B; (c) filter C; (d) filter D

penetrations and clogging points of four filters are different. At 4% the maximum penetration of filter D is two times higher than filter A, but the dust load at clogging point of filter D is about 4 times higher than filter A. Similarly, filter C shows a maximum penetration which is around 1.5 times of filter A, and the dust load at clogging point around 2 times of the case of filter A. For filter B, the maximum penetration is about 1.25 times of filter A, and the dust load at clogging point is 1.3 times of filter A. Obviously, we can lengthen the filter service life white maintaining sufficiently high aerosol collection efficiency at all times, for example by designing the filter structure as that of B, C or D.

Fig. 3 shows the distribution of mass deposited inside four filters. In Fig. 3(a), the maximum dust load always appears at L=0, the inlet side of the filter, and decreases steeply inside it. The front side of filter A will reach to clogging point of 60 kg/m^3 at 18,866 s or 314 min.

Similarly, in Fig. 3(b), the clogging time of filter B is around 25.573 s or 426 min. It shows about 1.4 times longer service life than filter A. In Fig. 3(c), the maximum dust loaded initially appears at L=0. After about 15,000 s, the maximum dust load of filter C slightly shifts back words. At 25,333 s, the maximum dust load appears at a filter depth of 0.0005, and then the maximum dust load starts to shift to the inlet side of filter. At the clogging point, the maximum dust load appears at the front end of the filter after 39,144 s, a service life about 2 times longer than filter A. Fig. 3(d) shows that the clogging time of filter D is around 82,284 s, about 4.3 times that of filter A.

3. Conclusion

The expensive electret filter cannot practically be cleaned and re-used. Therefore, it is vital to improve

the filter service life. Our simulation results show that it is possible to significantly lengthen the filter service life by packing the filter loosely on the front side and progressively more densely towards the back side, while maintaining a sufficiently high aerosol collection efficiency at all times. To obtain the optimal filter packing density, it is necessary to know only the correlation between the collection efficiency of the fiber and the dust load. Once the fiber packing density in a filter has been selected, we can reasonably predict the collection efficiency (or penetration) as a function of overall dust load or filtration time as well as the clogging condition.

Acknowledgements

W. S. receives TRF-RGJ PhD scholarship and support from the Association of International Education, Japan (AIEJ). W. T. receives partial financial support from Senior Research Scholar Project of Thailand Research Fund (TRF). C. K. visited Chulalongkorn University under Thailand–Japan Technology Transfer Project of CU.

References

- H. Emi, C. Kunaoka, Most Penetrating Particle Size in Electret Fiber Filtration, Aerosols, Elsevier, Amsterdam, 1984, pp. 567–572.
- [2] H. Emi, C. Kanaoka, Y. Otani, T. Ishiguro, Collection mechanisms of electret filter, Part. Sci. Technol. 5 (1987) 161-171.
- [3] C. Kanaoka, H. Emi, Y. Otani, T. Jiyama, Effect of charging state of particles on electret filtration, Aerosol Sci. Technol. 7 (1987) 1–13.
- [4] J. Pich, H. Emi, C. Kanaoka, Coulombic deposition mechanism in electret filters, J. Aerosol Sci. 18 (1987) 29–35.
- [5] F.J. Romay, B.Y.H. Liu, S.J. Chae, Experimental study of electrostatic capture mechanisms in commercial electret filters, Aerosol Sci. Technol. 28 (1988) 224–234.

- [6] Y. Otani, H. Emi, J. Mori, Initial collection efficiency of electret filter and its durability for solid and liquid particles. Kona (1993) 11207– 11214
- [7] M. Lee, Y. Otani, N. Namiki, H. Emi, Prediction of collection efficiency of high-performance electret filter, J. Chem. Eng. Jpn 33 (1) (2002) 57-62.
- [8] C. Kanaoka, H. Emi, Time Dependency of Collection Performance of Electret Filters, Aerosol, Elsevier, Amsterdam, 1984, pp. 613–616.
- [9] H.P. Baumgartner, F. Loffler, The collection performance of electret filters in the particle size range 10 nm-10 μm, J. Aerosol Sci. 17 (3) (1986) 438-445.
- [10] R.C. Brown, W.R. Gray, D.B. Blackford, G.J. Bostock, Effect of industrial aerosols on the performance of electrically charged filter material, Ann. Occup. Hyg. (1988) 3271-3294.
- [11] D.C. Walsh, J.I.T. Stenhouse, The effect of particle size, charge and composition on the loading characteristics of an electrically active fibrous filter material, J. Aerosol Sci. 28 (2) (1997) 307-321.

- [12] J.H. Ji, G.N. Bae, S.H. Kang, J. Hwang, Effect of particle loading on the collection performance of an electret cabin air filter for submicron aerosols, J. Aerosol Sci. 34 (2003) 1493–1504.
- [13] C. Kanaoka, H. Emi, W. Tanthapanichakoon, Conventive diffusional deposition and collection efficiency of aerosol on a dust-loaded fiber, Am. Inst. Chem. Eng. J. 29 (6) (1983) 895–902.
- [14] C. Kanaoka, S. Hiragi, W. Tanthapanichakoon, Stochastic simulation of the agglomerative deposition process of aerosol particles on an electret fiber, Powder Technol. 118 (2001) 97–106.
- [15] W. Tanthapanichakoon, K. Maneeintr, W. Charinpanitkul, C. Kanaoka, Estimation of collection efficiency enhancement factor for an electret fiber with dust load, J. Aerosol Sci. 34 (2003) 1505– 1522.
- [16] W. Sae-lim, W. Tanthapanichakoon, C. Kanaoka, Collection efficiency enhancement factor of an electret fiber under dust load. Regional Symposium on Chemical Engineering, Bangkok, Thailand, 2004, p. 56.



Science and Technology of Advanced Materials 6 (2005) 266-271



Effects of cosurfactant on ZnS nanoparticle synthesis in microemulsion

Tawatchai Charinpanitkul^{a,*}, Amornsak Chanagul^{a,*}, Joydeep Dutta^b, Uracha Rungsardthong^c, Wiwut Tanthapanichakoon^{a,c}

^aCenter of Excellence in Particle Technology, Faculty of Engineering, Chalalongkorn University, Bangkok 10330, Thailand

^bMicroelectronics and Microelectronics Laboratory, School of Advanced Technologies, Asian Institute of Technology, Pathumthani 12120, Thailand

^cNational Nanotechnology Center, National Science and Technology Development Agency, Pathumthani 12120, Thailand

Received 12 January 2005; revised 25 February 2005; accepted 25 February 2005 Available online 1 July 2005

Abstract

ZnS nanoparticles with different morphology; spherical, ellipsoidal particles' nanotubes and nanorods, could be successfully synthesized from quaternary W/O microemulsion system. The morphology of the final products could be clearly confirmed by the scanning electron microscopy (SEM) and the transmission electron microscopy (TEM). The effect of cosurfactant on size and morphology of the obtained products have been explored in this work. The key controlling parameters such as the molar ratio of water to surfactant (w_n) and the reactant concentration, which affect the product characteristics, have also been investigated.

© 2005 Elsevier Ltd. All rights reserved.

Keywords: Microemulsion; Cosurfactant; Zinc sulfide; Nanoparticle

1. Introduction

At the moment nanostructural materials have become attractive because of their unique characteristics that can hardly be obtained from conventional bulk materials owing to their quantum size and surface effects. In particular, much attention has been paid to synthesis of group II-VI semiconductor materials due to their excellent prospective in catalysis, optical and magnetic functionality, and so on [1].

To date there are many methodologies available for synthesizing ZnS nanocrystals, such as laser ablation, electrochemical fabrication and solvothermal methods [2]. However, water-in-oil (w/o) microemulsions or reverse micelles technique is one of the most recognized methods due to its several advantages, for instance, soft chemistry, demanding no extreme pressure or temperature control, easy to handle, and requiring no special or expensive equipment. In general, microemulsion or ME is an isotropic,

It is also known that addition of cosurfactant can reduce the surfactant concentration in microemulsion preparation. Normally, low molecular weight alcohols, such as *n*-butanol can be used for this purpose. Their short hydrophobic chain and terminal hydroxyl group is known to enhance the interaction with surfactant monolayers at the interface, which can influence the curvature of the interface and internal energy. The amphiphilic nature of cosurfactants

thermodynamically stable dispersion of oil, water, surfactant and often cosurfactant, which is normally alcohol. Microemulsion can be characterized as oil-in-water (O/W). water-in-oil (W/O) or bicontinuous system. Oil-in-water is microemulsion containing an excess oil phase with surfactant molecules existing in the aqueous phase in form of normal micelles. On the other hand, water-in-oil (W/O) microemulsion is the coexistence of an excess water phase and the surfactant molecules which aggregate in the oil phase in the form of reverse micelle. It is well known that these micelles could perform as nano-scaled reactors [3]. Once two microemulsions of which one contains the precursor and the other contains the precipitating agent are uniformly mixed, the reaction will occur in controlled manner in the micelles which have the size in order of nanometers, resulting in formation of nanoparticles of controlled characteristics.

^{*} Corresponding author. Fax: + 66 2 218 6480.

E-mail addresses: ctawat@chula.ac.th (T, Charinpanitkul), c_amornsak@hotmail.com (A, Chanagul).

^{1468-6996/\$ -} see front matter © 2005 Elsevier Ltd. All rights reserved, doi:10.1016/j.stam.2005.02.005

could also enable them to distribute between the aqueous and oil phase [4].

The most challenging problem for this synthesizing method is how to precisely control morphology and size of nanoparticles. The uniformity of morphology and size of the synthesized product is expected for being effective utilization in various specific applications, such as optical sensitizers, photocatalysts, light converting electrodes and inorganic light emitting diodes (ILEDs). Xu and Li reported that they could synthesize ZnS nanoparticles and nanorods in ternary water-in-oil microemulsion by varying some parameters such as the molar ratio of water to surfactant (wo) and temperature. Uniform nanorods could be obtained at wo of 11 and reactant concentration of 0.1 mol/dm3 after aging for 2 days [1]. Similarly, Xu et al. could obtain AgI nanowires of uniform diameter from a system of Triton X-100 microemulsion with n-pentanol as a cosurfactant at w_0 of 11 [5]. Lv et al. studied ZnS nanowires synthesis by sodium bis(2-ethylhexyl)sulfosuccinate (AOT) micelletemplate inducing reaction and found that the morphology and size of ZnS nanoparticles would also be affected by reactant concentration and wo [6]. Moreover, Lv et al. also reported that ZnS nanotubes could be obtained from O/W microemulsion by using CS2 as an oil phase and Triton X-100 as a surfactant [7]. In this paper, we have mainly focused on investigating the dependence of morphology of ZnS nanoparticles on cosurfactant types. Meanwhile, other variables, which are wo and reactant concentration, have also been investigated.

2. Experiment

All of the solvents, which are cyclohaxane and Triton X-100, and reactants (Zn²⁺ and S²⁻) used in this experiment are analytical grade and used without any further purification. First, the solution of Triton X-100, cyclohexane and cosurfactant were prepared and mixed in two accurate beakers. Then aqueous solutions of ZnSO₄ or Na₂S are added into each micoemulsion solution in separate beaker and vigorously agitated by a magnetic stirrer. After mechanical agitation for about 15 min, two separate microemulsion solutions were mixed together. The resulting mixture was then incubated for 2 days at room temperature. Samples were taken to analyze by SEM (JEOL JSM 5410LV), Energy Dispersive X-ray Spectroscopy (EDS) and TEM (JEOL JEM-1230).

3. Results and discussion

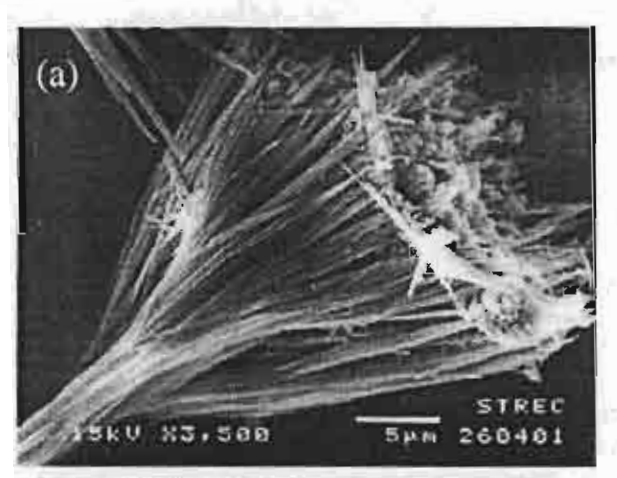
3.1. Effect of cosurfactant

In order to investigate the effects of cosurfactants, n-hexanol, n-pentanol, and n-butanol were selected and individually added into the microemulsion system with

concentration ratio of $C_{\rm Triton~X-100}/C_{\rm cosurfactant} = 1$ while w_0 were varied within the range of 5.5-20.0. The reactant concentration was tentatively kept constant at 0.1 mol/dm³. All syntheses were conducted at room temperature.

Without cosurfactant, the microemulsion with w_0 of 5.5 and reactant concentration of 0.1 mol/dm3 could provide ZnS nanoparticles with the morphology of long and short rods as well as ellipsoid as shown in Fig. 1. These ZnS nanorods have an aspect ratio of approximately 80 (200-750 nm in diameter and up to 30 µm in length). Meanwhile ellipsoidal ZnS nanoparticles have breadth in the range of about 90-200 nm. With an increase in wo up to 11, more agglomeration of ZnS particles and only few nanorods were observed. In order to identify the constituent of these synthesized products, typical EDS analysis was conducted to demonstrate that these products are ZnS nanocrystals (Fig. 2). The X-ray fluorescence peaks at 1.0 and 2.3 keV exhibit the combination of Zn and S. Meanwhile, the smaller peaks at 8.6 and 9.6 keV correspond to the transition of Zn Ka and KB, respectively.

By employing n-hexanol as cosurfactant at relatively low w_0 , Fig. 3(a) and (b) show that the synthesized



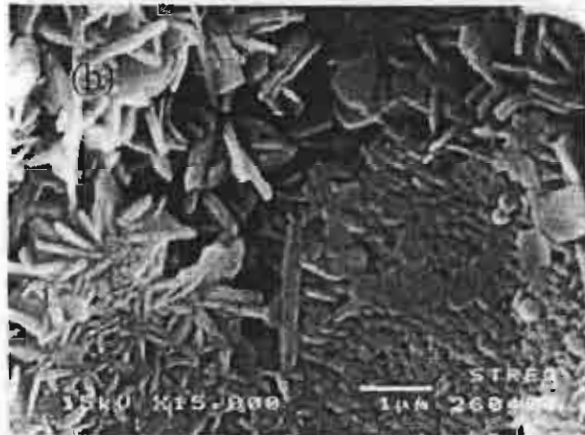


Fig. 1. SEM images of ZnS nanoparticles synthesized in ternary W/O microemulsion with w_o=5.5 and reactant concentration of 0.1 mol/dm³. No cosurfactant is added.

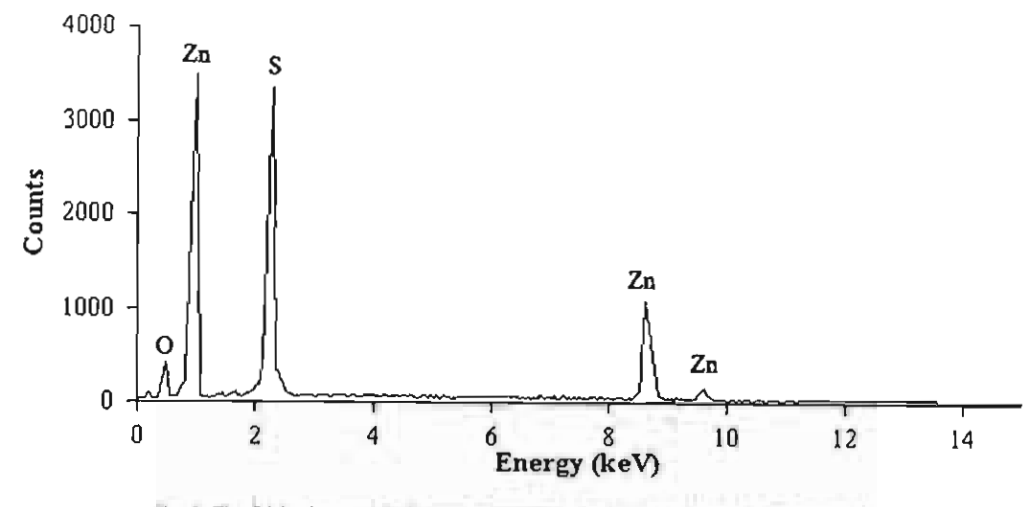


Fig. 2. The EDS of typical ZnS nanoparticle samples obtained from w/o microemulsion.

products were quantum dots with diameters less than 5 nm. These quantum dot particles could agglomerate to form secondary particles with larger diameters of between 40–100 nm, which however are much smaller than those obtained from heat treatment method [8]. Typically ZnS can be used as light emitting phosphor once it is doped with elements such as terbium (Tb) or samarium (Sm). The smaller the size of quantum dots the higher the light emission efficiency they could provide. Therefore it is reasonable to expect that the synthesized products in this work could potentially be used in electroluminescent applications upon doping.

However, it is noteworthy that at w_0 of 15 ZnS nanotubes with diameters of 20–40 nm and length of up to 2 μ m could be successfully synthesized (Fig. 3(c)). It could be confirmed from repeatability test that such hollow

nanotubes of ZnS exhibit a very narrow distribution with respect to their diameters.

It should be noted that there were some significant changes in the morphology of the synthesized ZnS nanoparticles when n-pentanol or n-butanol was employed as cosurfactant. At $w_0 = 7$, comparison of Figs. 3(a) and 4(a) reveals that predominant morphology of the synthesized ZnS are quantum dots and their agglomeration of which diameters are smaller than 100 nm. However, when increasing w_0 value to 11 and 15 n-pentanol could result in ZnS nanorods with some agglomerations as shown in Fig. 4(b) and (c). Interestingly, Fig. 5(a) and (b) show that with w_0 of 11 and 15 ZnS nanotubes with some quantum dc. depositing on their surface could again be successfully grown when n-butanol was employed as cosurfactant.

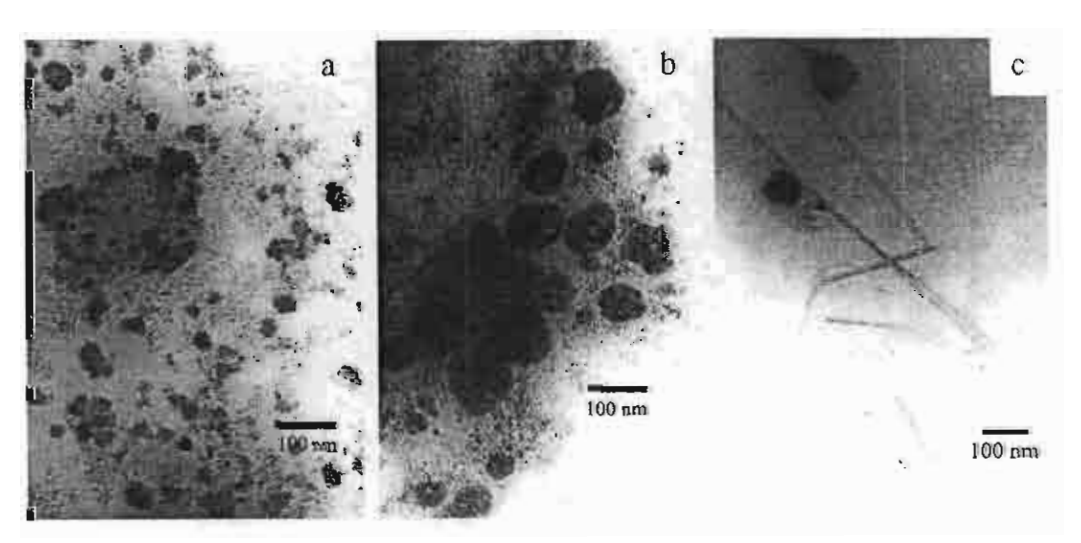


Fig. 3. TEM images of ZnS nanoparticles synthesized in microemulsions with n-hexanol as a cosurfactant at: (a) $w_0 = 1$, (b) $w_0 = 11$, and (c) $w_0 = 15$.

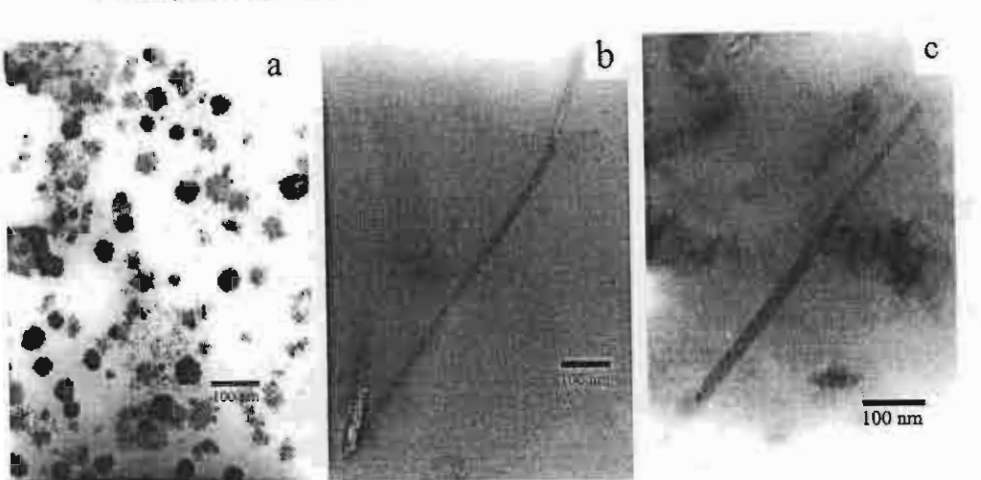


Fig. 4. TEM images of ZnS nanoparticles synthesized in microemulsion with n-pentanol as a cosurfactant at: (a) $w_0 = 7$, (b) $w_0 = 11$, and (c) $w_0 = 15$.

3.2. Effect of reactant concentration

The effect of absolute reactant concentration $[Zn^{2+}]$ and $[S^{2-}]$ on the morphology of ZnS nanoparticles synthesized in microemulsion systems was investigated by varying both $[Zn^{2+}]$ and $[S^{2-}]$ in the range of 0.10–0.05 mol/dm³. With a decrease in the reactant concentration to 0.05 mol/dm³, the synthesized ZnS nanoparticles mainly showed ellipsoidal morphology. With w_0 of either 11 or 20, the morphology of the ZnS nanoparticles synthesized in the microemulsion using n-hexanol as cosurfactant exhibited insignificant difference. As could be observed in Fig. 6(a) and (b), the agglomeration of ZnS nanoparticles, which formed larger aggregates with diameter up to 200 nm, were found all over the TEM grid but no nanorods or nanotubes were observed.

In addition, by employing *n*-pentanol as cosurfactant, the effect of reactant concentration on the morphology of the synthesized ZnS nanoparticles with various w_0 became insignificant. With the reactant concentration of 0.05 mol/dm^3 , at $w_0 = 11$ or 15 few ZnS nanorods with diameter of between 60 and 120 nm were found to coexist with a widely spreading ZnS quantum dots as shown in Fig. 7(a) or (b). From Fig. 7(c) with a further increase in w_0 to 20, long nanorods no longer existed but some ellipsoidal ZnS nanoparticles and ZnS quantum dots were found to disperse throughly within samples. The approximated diameter of these ellipsoidal nanoparticles were about 70–120 nm with the breadth of about 400 nm.

Finally, when *n*-butanol was used as cosurfactant, a similar trend was still observed. With lower concentration

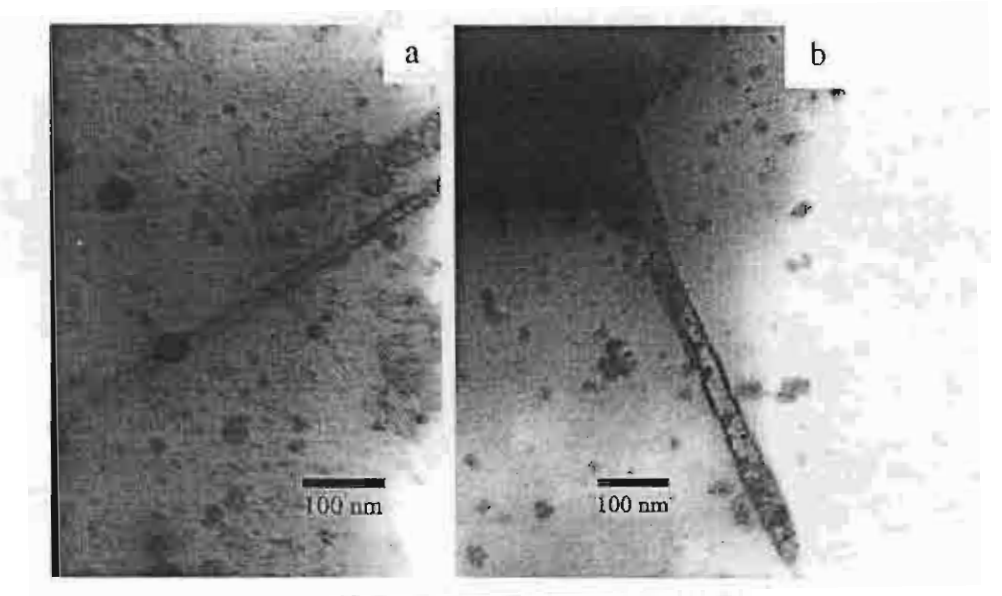


Fig. 5. TEM images of ZnS nanoparticles prepared in microemulsion with n-butanol as a cosofactant: (a) $w_0 = 11$, and (b) $w_0 = 15$.

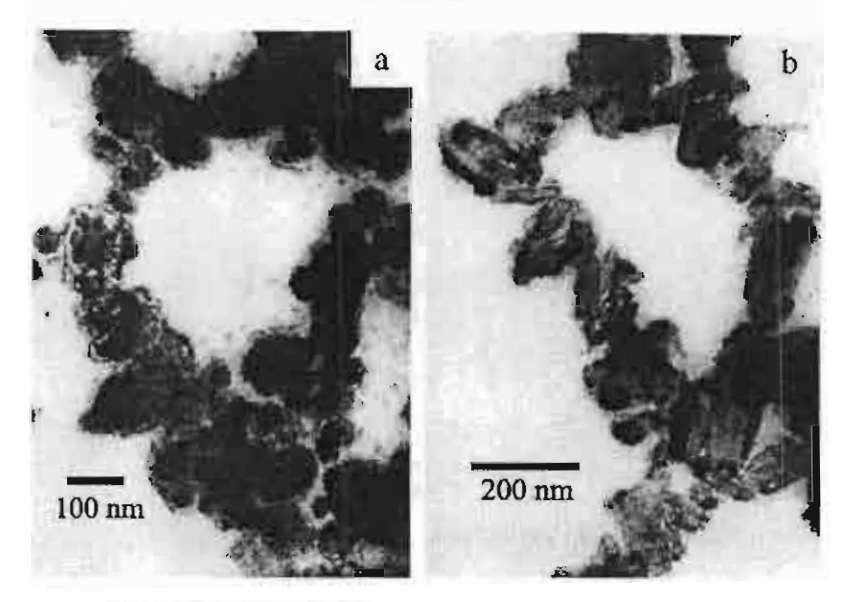


Fig. 6. TEM images of ZnS nanoparticles prepared in microemulsion with n-hexanol as a cosurfactant and reactant concentration = 0.05 mol/dm³: (a) $w_0 = 11$, and (b) $w_0 = 20$.

of the reactant, no ZnS nanotubes could be synthesized regardless of the increasing w_o . However, it is noteworthy that the elongated ellipsoidal morphology of ZnS nanoparticles could be obtained at $w_o = 7$ as shown in Fig. 8(a). With a further increase in w_o to 15 and 20, those ZnS nanoparticles with high aspect ratio disappeared. Fig. 8(b) and (c) show that only ZnS quantum dots and their agglomeration were randomly dispersed in the samples. The agglomerated nanoparticles have the approximated size of 20-100 nm. Also, it should be noted that further increasing w_o led to a decrease in the population density of the ZnS quantum dots and an increase in the number of agglomerated particles. This implies that the higher polarity

of an increased water amount might enhance the agglomerating process of synthesized ZnS nanoparticles.

4. Conclusions

ZnS nanoparticles with distinguishable morphology could be synthesized in quaternary W/O microemulsion systems using various types of cosurfactant. According to the above mentioned experimental results, it could be clearly shown that the size and the morphology of the ZnS nanoparticles are dependent upon the types of cosurfactant and the reactant concentration as well as the molar ratio of

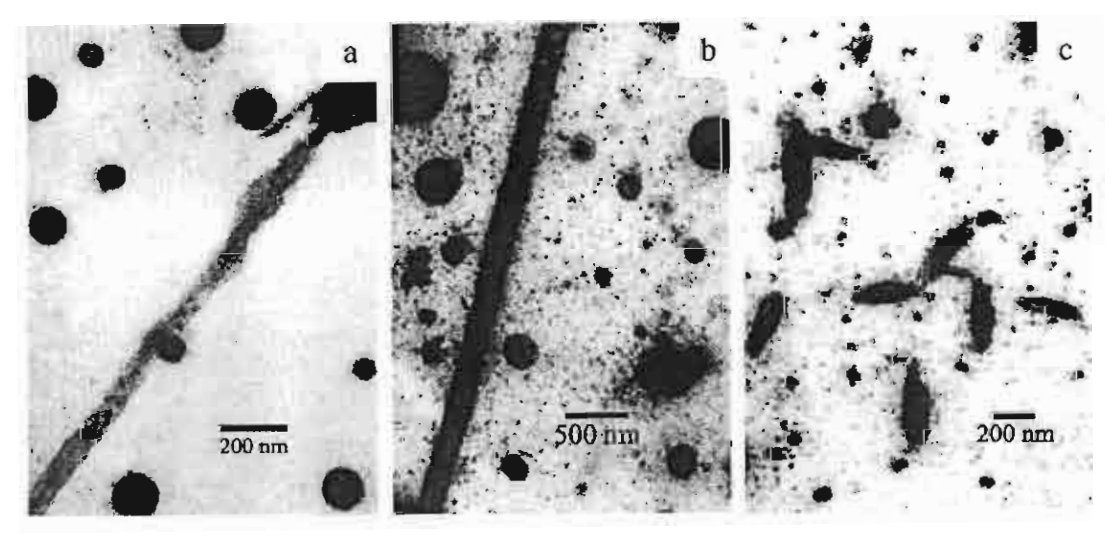


Fig. 7. TEM images of ZnS nanoparticles synthesized in microemulsion with *n*-pentanol as a cosurfactant and reactant concentration = 0.05 mol/dm³: (a) $w_0 = 11$, (b) $w_0 = 15$, and (c, d) $w_0 = 20$.

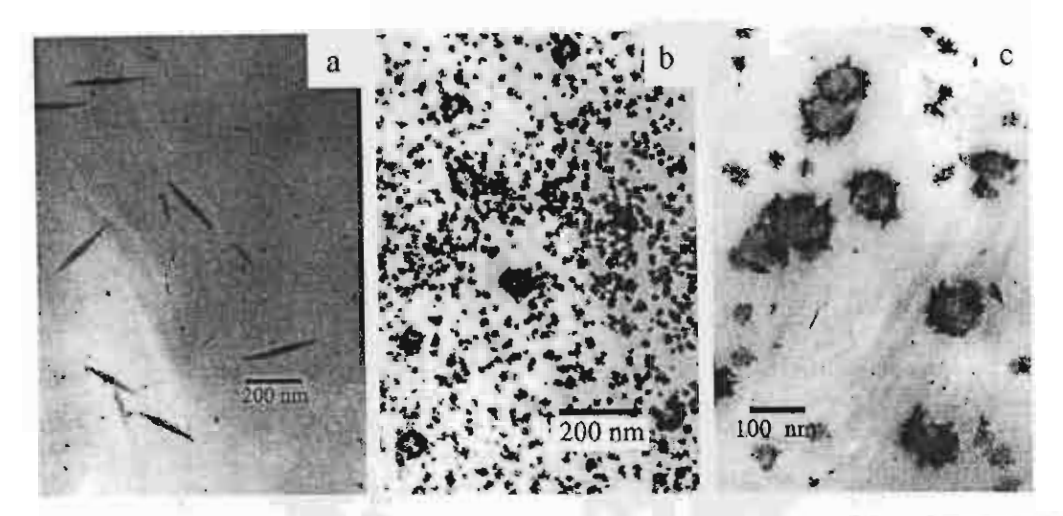


Fig. 8. TEM images of ZnS nanoparticles synthesized in microemulsion with *n*-butanol as a cosurfactant and reactant concentration = 0.05 mol/dm³: (a) w_n = 7. (b) w_0 = 15, and (c) w_0 = 20.

water to surfactant (w_0) . Cosurfactants with larger molecular size such as n-hexanol could provide higher possibility to synthesize ZnS nanoparticles with higher aspect ratio, like nanorod or nanotube. With relatively high reactant concentration, some certain amount of ZnS nanorod and nanotubes could be successfully synthesized. With n-hexanol at $w_0 = 15$, and reactant concentration of 0.1 mol/dm³, ZnS nanoparticles with the morphology of hollow tubes could be repeatedly synthesized. However, with lower reactant concentration, spherical ZnS quantum dots or ellipsoidal nanoparticles were predominantly obtained regardless of cosurfactant types or w_0 .

Acknowledgements

This research project is partially supported by TRF-RTA (Prof. W. Tanthapanichakoon), TJTTP-JBIC and University-Industrial Collaborative Research Project of CU.

Reference

- J. Xu, Y.D. Li, Formation of zinc sulfide nanorods and nanoparticles in ternary W/O microemulsion, J. Colloid Interface Sci. 259 (2003) 275-281.
- [2] Q.T. Zhao, L.S. Hou, R. Huang, Synthesis of ZnS nanorods by a surfactant-assisted soft chemistry method, Inorg. Commun. 6 (2003) 971-973.
- [3] K.J. Klabunde (Ed.), Nanoscale Materials in Chemistry, Wiley-Interscience, New York, 2001.
- [4] R.G. Alany, T. Rades, S. Agatonovic-Kustrin, N.M. Davies, I.G. Tucker, Effects of alcohols and diols on the phase behaviour of quaternary systems, Int. J. Pharm. 196 (2000) 141-145.
- [5] S. Xu, H.C. Zhou, J. Xu, Y.D. Li, Synthesis of size-tunable silver iodide nanowires in reverse micelles, Langmuir 18 (2002) 10503–10504.
- [6] R.T. Lv. C.B. Cao, H.S. Zhu. Synthesis and characterization of ZnS nanowires by AOT micelle-template inducing reaction, Mater. Res. Bull. 39 (2004) 1517-1524.
- [7] R.T. Lv, C.B. Cao, Y.J. Guo, H.S. Zhu, Preparation of ZnS nanotubes via surfactant micelle-template inducing reaction, J. Mater. Sci. 39 (2004) 1575-1578.
- [8] H.S. Kim, W. Sigmund, Zinc sulfide nanocrystals on carbon nanotubes. J. Cryst. Growth 255 (2003) 114–118.

Index Ordering

You can now add your name to our electronic mailing list

Advanced Powder Technology

Volume 16, No. 3, pp. 199--300, 2005

Original papers

Radicalar probes to measure the action of energy on granular materials M. Baron, A. Chamayou, L. Marchioro and J. Raffi 199

Fragile structured layers on surfaces detected by dynamic atomic force microscopy in aqueous electrolyte solutions

Y. Li, Y. Kanda, H. Shinto and K. Higashitani 213

Determination of applicable local porosity distributions in a powder bed by the maximum entropy method

T.-L. Lin and L.-W. Hourng 231

Transition velocities in the riser of a circulating fluidized bed N. Balasubramanian, C. Srinivasakannan and C. A. Basha 247

Investigation of gas--solid flow structure after a 90° vertical-to-horizontal elbow for low conveying gas velocities

H. Akilli, E. K. Levy and B. Sahin 261

Prediction of gas--particle dynamics and heat transfer in a two-dimensional spouted bed T. Swasdisevi, Wiwut Tanthapanichakoon, T. Charinpanitkul, T. Kawaguchi, T. Tanaka and Y. Tsuji 275

Titles of the original research papers published in the Japanese journals 295

APPIE report

297

Calendar of events

298



Books Journals Search

Index

VSP Postal address: P.O. Box 9000, 2300 PA Leiden, The Netherlands Office address: Plantijnstraat 2, 2321 JC Leiden, The Netherlands

Advanced Powder Technol., Vol. 00, No. 0, pp. 1-19 (2005) © VSP and Society of Powder Technology, Japan 2005. Also available online - www.vsppub.com

Original paper

Prediction of gas-particle dynamics and heat transfer in a two-dimensional spouted bed

THANIT SWASDISEVI, WIWUT TANTHAPANICHAKOON 1.*, TAWATCHAI CHARINPANITKUL 1, TOSHIHIRO KAWAGUCHI 2, TOSHITSUGU TANAKA 2 and YUTAKA TSUJI 2

Received 5 February 2004; accepted 10 September 2004

Abstract—The aerodynamics of particles and heat transfer of gas-to-particles in a two-dimensional spouted bed (2DSB) with draft plates are investigated by the discrete element method (DEM). The physical properties of the particles are similar to those of shelled corn. The calculated minimum spouting velocity and pressure drop agree well with the empirical correlations proposed by Kudra et al. The particle circulation rate increases when the friction coefficient decreases or the separation height increases. The draft plates can reduce the minimum spouting velocity and pressure drop. They also increase the maximum spoutable bed height. The effect of taking out the draft plates on the spouting phenomenon is investigated. The mixing of a 2DSB without draft plates of 10,000 particles is better than that of 26,000 particles. In our simulation, the gas-to-particle heat transfer is investigated. The Ranz-Marshall correlation and the correlation of Sartori et al. are applicable in the spout region and the downcomer region, respectively. The gas-to-particle heat transfer occurs mainly in the central or spout region, as reported by Freitas and Freire.

Keywords: Two-dimensional spouted bed; minimum spouting velocity; particle velocity profiles: discrete element method simulation; gas-to-particle heat transfer.

NOMENCLATURE

A_d	cross-sectional area of downcomer (m2)
$A_{p,k}$	external area of a particle (m2)
$c_{p,g}$	heat capacity of gas (J/kg K)
$C_{p,k}$	specific heat of particle (J/kg K)
d_{p}	particle diameter (m)

^{*}To whom correspondence should be addressed. E-mail: Wiwut,T.@Chula.ac.th

Department of Chemical Engineering, Faculty of Engineering, Chulalongkorn University, Patumwan, Bangkok 10330, Thailand

² Department of Mechanophysics Engineering, Faculty of Engineering, Osaka University, 2-1 Yamada-oka, Suita, Osaka 565-0871, Japan

```
2
                                      T. Swasdisevi et al.
                     gravity (m/s2)
g
                     heat transfer coefficient between the particle and gas (J/K m<sup>2</sup> s)
h_{p}
H_{\rm b}
                     bed height (m)
H_{\rm d}
                     spout height (m)
H_{c}
                     entrance height or separation height (m)
Ι
                     moment of inertia (kg m2)
k
                     spring constant (N/m)
                     thermal conductivity of gas (W/mK)
k_c
                     bed length (m)
L_{\rm b}
Μ
                     degree of mixing (—)
                     mass of particle (kg)
m
Nu
                     Nusselt number (—)
                     gas pressure (Pa)
р
\Delta P_{\mathsf{ms}}
                     minimum spouting pressure drop (Pa)
Pr
                     Prandtl number (---)
                     heat transfer rate (J/s m3)
Q_{\rm s}
Re
                     Reynolds number (—)
R_{\rm d}
                     distance from the spout central axis to the draft plate (m)
                     normal distance (m)
T_{\rm g}
                     gas temperature (K)
                     temperature of particle (K)
T_{p,k}
                     time step (s)
\Delta t
                     gas velocity of the ith direction in the coordinate (m/s)
и
                     superficial gas velocity at inlet gas (m/s)
u_i
                     minimum spouting velocity (m/s)
u_{ms}
                     particle velocity (m/s)
v_{p}
                     particle velocity above slanting base (m/s)
v_{\rm ps}
                     average particle velocity (m/s)
\bar{v}_{vi}
                     volume of a particle (m3)
V_{\rm p}
                     vessel width (m)
\boldsymbol{w}
                     bed width (m)
w_{\mathsf{b}}
                     spout width (m)
w_d
                     width of gas inlet (m)
w_{i}
W_{\mathsf{s}}
                     mass flow rate of particle (kg/s)
                     distance from the central spout axis in the y direction (m)
ν
                     distance from the bottom of the vessel in the z direction (m)
Z
```

3

Greek	
ε	void fraction (—)
$ ho_{b}$	bulk density $\rho_b = \rho_p (1 - \varepsilon) (kg/m^3)$
$ ho_{ extsf{g}}$	gas density (kg/m3)
$ ho_{ m p}$	particle density (kg/m³)
ϕ	sphericity (—)
θ	slant angle (deg)
μ	friction coefficient (—)
μ_{g}	gas viscosity (Pas)
ω	angular velocity (1/s)

1. INTRODUCTION

Corn is an important economic agricultural produce for Thailand, the USA and many other countries. The demand for corn is high, especially in the feed milling and food industries. Modern agricultural technology has been developed to solve the problem of the shortage of corn. Consequently, a huge quantity of corn is often produced within a short period of harvest time, thereby resulting in poor corn quality and infection with aflatoxin B-1 in corn with a high moisture content. In this situation, solar drying is generally unsuitable because it depends on weather conditions. Therefore, fluidized bed and spouted bed dryers are often employed because of the high capacity and small area required for installation. The spouted bed technique has become established as an alternative to the fluidized bed for the handling of particulates which are relatively coarse and monodisperse in size. Spouted beds are widely used in industry, e.g. for the drying of granular materials, granulation of powders, coating of tablets and blending of solids. The main feature of spouted beds is the continuous movement or circulation of particles between the spout and the downcomer of the bed.

In the drying operation, the intensive particle circulation results in nearly uniform final moisture content and bed temperature, while the high velocity of the injected gas allows high gas temperature without thermal degradation of the product. Although the spouted bed requires a relatively higher pressure drop prior to the onset of spouting and a higher inlet gas velocity (but much lower volumetric flow rate) than the fluidized bed, the resulting high thermal efficiency makes this technique economically feasible under numerous conditions [1]. The literature on conical—cylindrical spouted beds (CSBs) has shown that the continuous movement of particles has a significant effect on the performance of the spouted beds in industrial applications such as drying, coal gasification, granulation and particle coating. However, CSBs are rarely used in the post-harvest industry because of scale-up and operating problem [2]. Passos et al. [1] proposed the idea of a two-dimensional spouted bed (2DSB) in order to overcome some of the limitations of

4

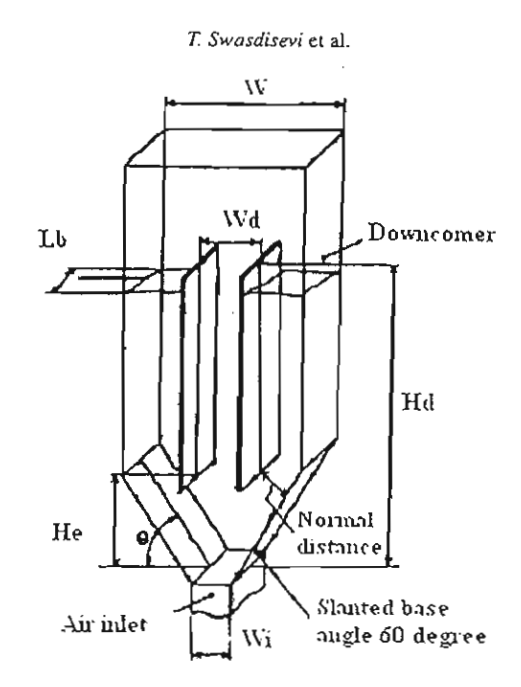


Figure 1. Schematics of the 2DSB with draft plates.

CSBs. As shown in Fig. 1, a typical 2DSB consists of planar walls with a slanting base and has an air entry slot along the center of the bed width. The rectangular geometry presents an easy solution to the increase in production. Production can readily be doubled or tripled by adding identical units in the orthogonal direction. In other words, the laboratory-scale apparatus can be considered to be a single unit in a complex of similar units. In addition, to stabilize solids circulation and reduce the bed pressure drop, draft plates are frequently inserted in the core of the spouted bed to separate the spout region from the downcomer region [3].

Computational techniques are now available to simulate multi-phase flows, including dilute- and dense-phase gas-solid flows. The discrete element method (DEM) is a handy tool for obtaining detailed information on these complex phenomena without physically disturbing the flows. A distinct advantage of carrying out DEM simulation of the spouted bed over the traditional use of the two-fluid models is that the former is capable of elucidating the bed dynamics at the individual particle level [4]. Tsuji et al. [5, 6], Kawaguchi et al. [7, 8], Kaneko et al. [9], Kawagi et al. [10, 11] and Rong et al. [12] successfully applied the DEM to investigate particle flow, particle mixing, formation of bubbles and hot-spot formation in the fluidized bed. They found that the calculated results are in good agreement with experimental observations. Van Nierop et al. [13] and Rhodes et al. [4] applied DEM to investigate the charge motion of a mill and mixing in a gas-fluidized bed. They found that the calculated results agreed well with the experimental results.

Recently, a 2DSB with draft plates has been developed for post-harvest grain drying [14, 15]. Because of the difficulty in measuring the particle dynamics, spatial distribution of particle temperature, etc., without causing disturbances to the system, it is useful to gain some basic understanding of these system characteristics with the aid of DEM. As mentioned above, the 2DSB is selected for this work because it is suitable for coarse heat-sensitive particles. In this work, the physical properties of the particles are similar to those of shelled corn. The minimum spouting velocity, pressure drop, spatial distribution of particle velocity, particle circulation rate and temperature distribution are analyzed and presented. Such detailed, though qualitative, information will be useful for the understanding and improved design of a 2DSB dryer.

2. GOVERNING EQUATIONS

2.1. Fluid motion and temperature

The locally averaged equation of continuity and equation of motion (Navier-Stokes equation) are used to calculate the fluid motion. All the local quantities of the fluid in a calculation cell such as pressure and velocity are represented by their local averages. The void fraction of each cell is calculated from the total volume of the particles contained in it. In this way, the position and velocity of individual particles are not of concern in the equation of fluid motion. Only the local total volume of the particles and their local average velocities are considered. The equations for the fluid motion are as follows:

Equation of continuity:

$$\frac{\partial}{\partial t}\varepsilon + \frac{\partial}{\partial x_i}(\varepsilon u_j) = 0. \tag{1}$$

Equation of motion:

$$\frac{\partial}{\partial t}(\varepsilon u_i) + \frac{\partial}{\partial x_j}(\varepsilon u_i u_j) = -\frac{\varepsilon}{\rho_g} \frac{\partial \rho}{\partial x_i} + f_{pi}. \tag{2}$$

Tsuji et al. [8] have shown that the fluid may be treated as inviscid except for the interaction term (f_{pi}) between the fluid and the particles.

$$f_{pi} = \frac{\beta}{\rho_g} (\bar{v}_{pi} - u_i), \tag{3}$$

where ε , u, p, ρ_g and \bar{v}_{pi} are the local void fraction, fluid velocity, pressure, fluid density and average particle velocity, respectively. The coefficient β is derived from Ergun's equation [16] for the dense phase and Wen and Yu's equation [17] for the dilute phase.

Similarly, a model of the convective gas-to particle heat transfer can be derived by using the following assumptions. (i) Physical properties such as heat capacity,